AFRL-AFOSR-VA-TR-2022-0476

Dynamics of Interactions Between Turbulent Boundary Layers And Compliant Surfaces

McNamara, Jack
OHIO STATE UNIVERSITY
1960 KENNY RD
COUMBUS, OH,
US

08/08/2022
Final Technical Report

Air Force Research Laboratory
Air Force Office of Scientific Research
Arlington, Virginia 22203
Air Force Materiel Command

REPORT DOCUMENTATION PAGE

PLEASE DO NOT RETURN YOUR FORM TO THE ABOVE ORGANIZATION.

1. REPORT DATE	2. REPORT TYPE	3. DATES COVERED	
20220808	Final	START DATE 20170315	END DATE 20210514

4. TITLE AND SUBTITLE
Dynamics of Interactions Between Turbulent Boundary Layers And Compliant Surfaces

5a. CONTRACT NUMBER	5b. GRANT NUMBER	5c. PROGRAM ELEMENT NUMBER
	FA9550-17-1-0106	61102F
5d. PROJECT NUMBER	**5e. TASK NUMBER**	**5f. WORK UNIT NUMBER**

6. AUTHOR(S)
Jack McNamara

7. PERFORMING ORGANIZATION NAME(S) AND ADDRESS(ES)
OHIO STATE UNIVERSITY
1960 KENNY RD
COUMBUS, OH
US

8. PERFORMING ORGANIZATION REPORT NUMBER

9. SPONSORING/MONITORING AGENCY NAME(S) AND ADDRESS(ES)	10. SPONSOR/MONITOR'S ACRONYM(S)	11. SPONSOR/MONITOR'S REPORT NUMBER(S)
Air Force Office of Scientific Research 875 N. Randolph St. Room 3112 Arlington, VA 22203	AFRL/AFOSR RTA1	AFRL-AFOSR-VA-TR-2022-0476

12. DISTRIBUTION/AVAILABILITY STATEMENT
A Distribution Unlimited: PB Public Release

13. SUPPLEMENTARY NOTES

14. ABSTRACT
A synergistic experimental and computational campaign was carried out to improve our understanding of interactions that arise from Turbulent Boundary Layers (TBL) and Shock Boundary Layer Interactions (SBLI) over compliant surfaces. Such phenomena represent design-driving conditions for structural skin panels on high-speed air vehicles, yet we lack basic understanding for high-confidence predictions. Thus, careful and systematic breakdown of the problem was carried out so as to improve our fundamental understanding of this challenging problem. Using high-fidelity simulation, we considered both prescribed and coupled surface conditions. Companion experimental measurements of the same conditions were taken over both statically deformed and compliant surfaces. Uncoupled application of computed pressure distributions onto structural models were also considered in order to better elucidate the impact of coupling on the system responses. Collectively, these results provide key physical insights into the degree of dynamic interaction and feedback associated with TBL and SBLI on compliant surfaces; provide the necessary foundation to enable development of improved structural response prediction tools in these conditions, and also direct future
computational and experimental studi

15. SUBJECT TERMS

16. SECURITY CLASSIFICATION OF:			17. LIMITATION OF ABSTRACT	18. NUMBER OF PAGES
a. REPORT	b. ABSTRACT	c. THIS PAGE		
U	U	U	UU	78

19a. NAME OF RESPONSIBLE PERSON	19b. PHONE NUMBER *(Include area code)*
SARAH POPKIN	000-0000

Final Report

Dynamics of Interactions Between Turbulent Boundary Layers and Compliant Surfaces

Fundamental Research in response to BAA-AFOSR-2015:

Energy, Power and Propulsion - Aerothermodynamics

Principal Investigators:
Jack J. McNamara
Mechanical & Aerospace Engineering
The Ohio State University
(614) 292-6778, mcnamara.190@osu.edu

Datta V. Gaitonde
Mechanical & Aerospace Engineering
The Ohio State University
(614) 688-1122, gaitonde.3@osu.edu

Joanna M. Austin
GALCIT
California Institute of Technology
(626) 395-4479, jmaustin@caltech.edu

Submitted to: Dr. Sarah Popkin
Air Force Office of Scientific Research
875 N. Randolph St.
Arlington, VA 22203-1768
sarah.popkin@us.af.mil

Sponsored Program Officer: Ms. Geetha Sampathkumar
Sampathkumar.11@osu.edu

Period of Performance: March 15, 2017 - May 14, 2021

Abstract

A synergistic experimental and computational campaign was carried out to improve our understanding of interactions that arise from Turbulent Boundary Layers (TBL) and Shock-Boundary Layer Interactions (SBLI) over compliant surfaces. Such phenomena represent design-driving conditions for structural skin panels on high-speed air vehicles, yet we lack basic understanding for high-confidence predictions. Thus, careful and systematic breakdown of the problem was carried out so as to improve our fundamental understanding of this challenging problem. Using high-fidelity simulation, we considered both prescribed and coupled surface conditions. Companion experimental measurements of the same conditions were taken over both statically deformed and compliant surfaces. Uncoupled application of computed pressure distributions onto structural models were also considered in order to better elucidate the impact of coupling on the system responses. Collectively, these results provide key physical insights into the degree of dynamic interaction and feedback associated with TBL and SBLI on compliant surfaces; provide the necessary foundation to enable development of improved structural response prediction tools in these conditions, and also direct future computational and experimental studies on the problem.

Table of Contents

1 Statement of Objectives

A synergistic experimental and computational campaign was carried out from 2017-2021 to significantly improve our understanding of nonlinear interactions and energy transfer that arise from Turbulent Boundary Layers (TBL) and Shock-Boundary Layer Interactions (SBLI) over compliant surfaces. Such phenomena represent design-driving conditions for structural skin panels on high-speed air vehicles, yet we currently do not have sufficient basic understanding for high-confidence predictions. Since experiments and computations are expensive and difficult for this class of problem, we carried out a systematically progressive decomposition so as to target key knowledge gaps and lay the basic research foundation needed to direct future studies and ultimately revolutionize predictive models. Specifically, we studied and statistically characterized TBL/SBLI for the following surface conditions:

1. rigid baseline (experiments and simulations)
2. static, varying surface topology (experiments and simulations)
3. coupled fluid-structural response (experiments and simulations)
4. uncoupled application of fluctuating fluid pressures on compliant structures (simulations only)

Successively increasing the interaction between the fluid and structure was done to mitigate the constraint of short time records (from a structural response perspective) needed to carry out the experiments/high-fidelity flow simulation ($<$100 ms). Cases $1-3$ enabled characterization of sensitivities of the fluid dynamics to (structurally relevant) varying surface topology. Case 4 yielded insight into the degree of coupling between the fine scale fluid dynamics and structural response. Together, this enables fundamental characterization of dominant features that govern interactions between fine scale boundary layer dynamics and structural compliance.

2 Key Novel Contributions

Several novel accomplishments in the state-of-the-art in high-speed fluid-structure interaction research were achieved throughout the course of this research. In summary, these are:

- The onset of boundary layer separation elevates the importance and complexity of coupling between fine scale dynamics in the boundary layer and structural compliance.
- Streamwise surface curvature is identified as a dominant driver for structurally induced onset of boundary layer separation.
- Large eddy simulations of shock-boundary layer interactions with a responding surface reveal complex, and insufficiently understood, fluid-structural energy transfer mechanisms when compared to baseline uncoupled responses of the fluid and structure.
- Deployment of suite of measurement techniques for both structural and flow field response has been demonstrated in lab-scale FSI experiments in a Mach 4 windtunnel.
- Measurements conducted over i) baseline flat plate including freestream and incoming boundary layer characterization, ii) rigidly-deformed panels representative of long-time scale deflection, iii) compliant panels.
- Motor-driven oscillating shock generator designed, built, and demonstrated for impinging shock experiments on complaint surfaces. The experiment is designed to force fluid time scales comparable to selected structural timescales.

3 Introduction and Motivation

A long-standing challenge in the development of high-speed flight systems is adequate understanding of Turbulent Boundary Layers (TBL) and Shock-Boundary Layer Interactions (SBLI). In particular, predicting the associated loading conditions is crucial for the development of lightweight structural systems, and by extension, maneuverable and reusable high-speed air vehicles. However, the current state-of-the-art is not adequate to meet this need [1–6]. This stems from the inherent complexity and multi-scale nature of the fluid physics, the potential for fluid-structure interactions on lightweight systems, and difficulty in carrying out experimental and numerical study of the problem due to disparities in scales for the evolving fluid and structural/material responses. This research program addressed these issues through systematic study of TBL and SBLI at structurally relevant scales; targeting key specific knowledge gaps that currently impede the design and life prediction of lightweight structural systems needed for reusable high-speed flight vehicles.

4 Background

The importance of structural loads imposed by TBL and impinging shock waves, as well as the current gap in prediction of structural response to these conditions, is well recognized. Recently, the Aerospace Systems Directorate of AFRL (AFRL/RQ) has sponsored a 6.2 research program by Boeing and Lockheed Martin to examine the predictive capabilities for hypersonic structural response and life prediction [2–5]. The effort identified the intense fluctuating pressures associated with TBL and oblique shockwave generated SBLI as design-driving loading environments; and assessed the current state-of-the-art as inadequate for reliably predicting the response and life of reusable, compliant structural components in such conditions.

There is a large body of literature on TBL and SBLI over rigid surfaces (see overviews by Bies [7], Smits and Dussauge [8], Dolling [9] and Gaitonde [10]). Studies that include compliant boundaries are more limited due to challenges already discussed. Early foundational experimental / theoretical efforts focused on characterizing the relevant statistical properties of TBL and SBLI for structural response prediction at supersonic speeds [1, 11–17]. Shown in Figs. 1 and 2 are measurements of power spectra and spatial correlations by Coe and Chyu [16] for Mach 1.5 to 3.5. Note that the maximum power spectra and spatial correlation occur over frequency bands that overlap with primary structural response modes – i.e., Strouhal numbers of $O(0.001 - 0.1)$. This observation is consistent with measurements that indicated that the structural response was dominated by the first few modes [14–16]. A number of studies that examined panel response in subsonic turbulent flow (see the overview by Bies [7]) suggested the existence of a 'coincidence' frequency that provided an approximate upper bound of the structural response for panels subjected to TBL. However, similar trends were not explicitly evident for supersonic flow.

Some benchmarking of predictive capabilities was also carried out using subsequently developed semi-empirical fluid loads models [15, 16] or assuming a homogeneous random excitation[18]. The results were mixed, with reasonable agreement in some qualitative trends, but significant under-prediction of magnitude of panel response [15, 16]. Note that a number of semi-empirical models [19] have been reasonably successful in capturing the characteristic trends and magnitude of the TBL loads in subsonic flows [11, 20, 21]. However, the accuracy of these models was found to degrade below acceptable levels for values of Strouhal number less than 1 - corresponding to lower, more compliant, structural modes - and for high-speed flows.

More recently are computational efforts in supersonic flows using phenomenological models [22], RANS level analysis with add-on fluctuating pressure models [23–25], Detached Eddy Simulation [26, 27], laminar SBLI [28], and DNS [29]. There is also a growing body of experimental work, such as that at the

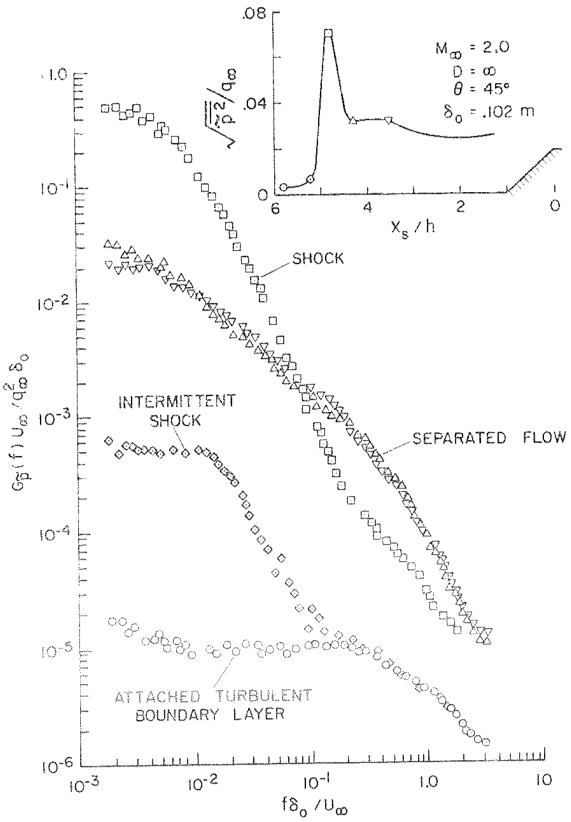

Figure 1: Power spectra of cross spectra density for fluctuating pressures in supersonic turbulent boundary layers. [16]

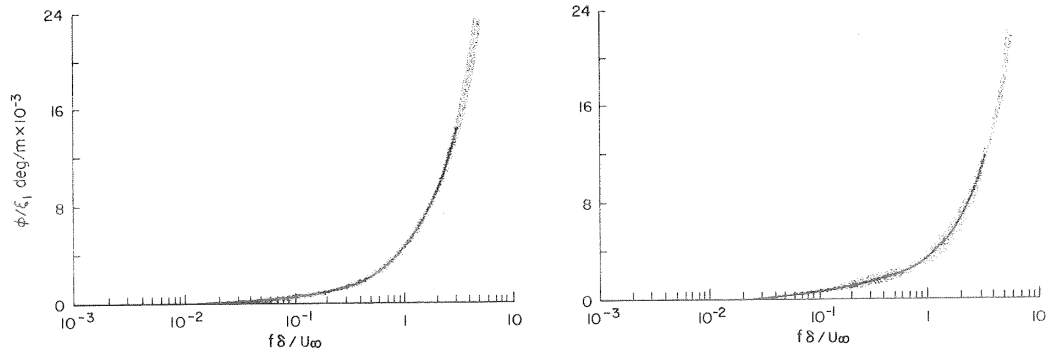

Figure 2: Phase angles of cross spectra density for fluctuating pressures in supersonic turbulent boundary layers. [16]

AFRL/RQ [6, 30], the DLR [31, 32], Imperial College [33], UNSW Canberra [34], NC State [35], and University of Maryland [36]. This recent body of work has yielded new insights into the interactions. However, the complexity and scale of the problem has continued to impede progress through a combination of: limited scope of study (in terms of operating conditions, structural length scales, response times, etc.), modeling fidelity, test conditions and measurement capabilities. Thus, there remains a litany of unanswered questions.

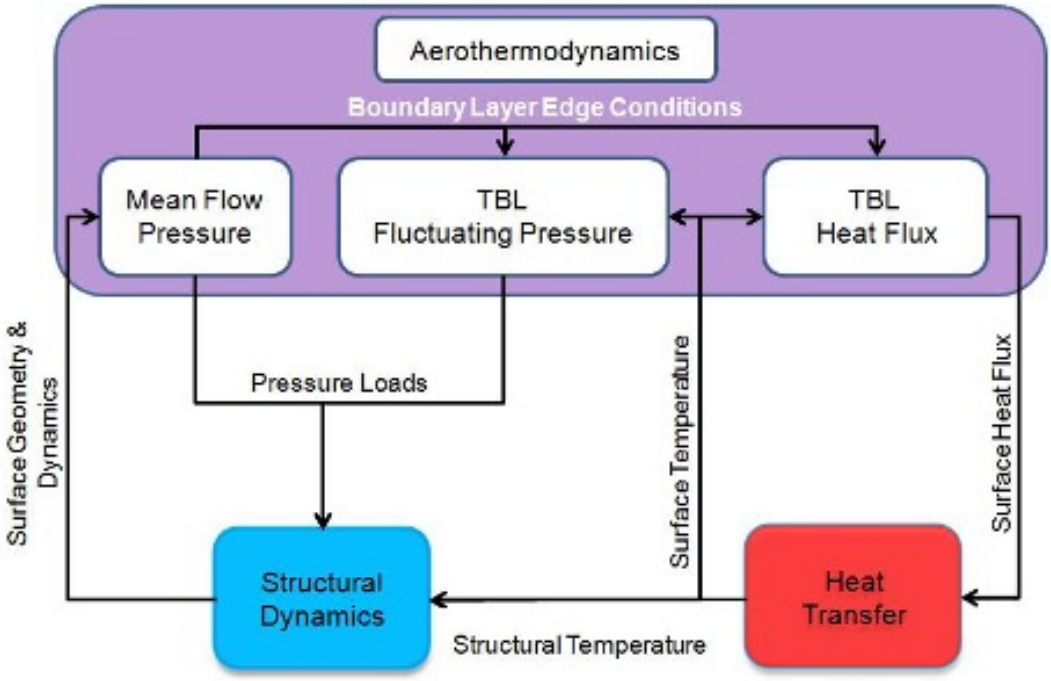

Figure 3: Schematic of different coupling mechanisms during aerothermoelastic response of skin panels operating in high-speed, turbulent flows. [22]

In order to highlight deficiencies in engineering class modeling efforts, consider work by Deshmukh, McNamara, and Culler [22], who coupled a basic TBL load model used by original equipment manufacturers [2] into a 2-D aerothermoelastic response prediction code for structural panels. The TBL load model consisted of two parts: 1) a model for the RMS of the fluctuating pressure, which was based on the semi-empirical model developed by Laganelli et al. [1, 17, 37]; and 2) the phase angle of the fluctuating pressure; where the spatial component was predicted using the semi-empirical model developed by Coe and Chyu [16], and the temporal component was assumed random in time. As shown in Fig. 3, the TBL load model is implicitly coupled to the structural response through dependency on boundary layer edge conditions, and explicitly coupled to the thermal response through surface temperature. Using this model, several different cases were considered to investigate the sensitivity of the structural response to uncertainties in both RMS and phase angle of the TBL fluctuating pressure model. A key finding was the importance of coupling between the TBL model and the structural response – i.e., the panel response was significantly varied between the cases that included and neglected feedback from the surface conditions to the TBL load model. However, as highlighted by Fig. 4, the panel response was also found to be sensitive to variations in the TBL model itself within expected bounds of uncertainty. Furthermore, while coupling between the TBL load model and the aerothermoelastic response was found to be significant, the TBL load models were never intended for such use. Thus, there is a continued need for improved fundamental understanding of these complex interactions so as to enable the development of improved predictive models.

In related work, Gogulapati, Deshmukh, Crowell, McNamara et al. [24, 25] combined a RANS CFD model with the TBL model developed by Deshmukh, McNamara, and Culler [22] to carry out a comparison with SBLI experiments conducted by the AFRL/RQ Structural Sciences Center [6, 30]. Unsurprisingly, com-

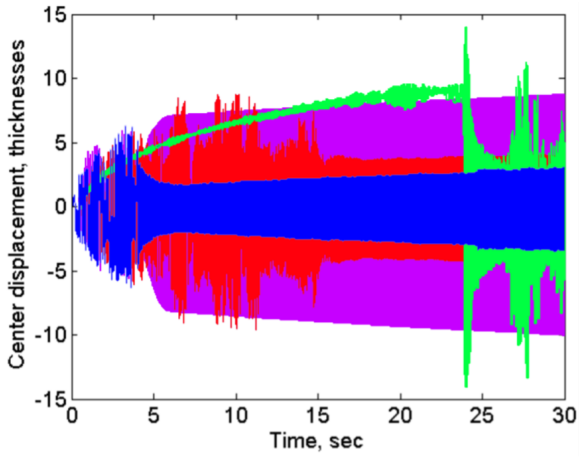

Figure 4: Center point displacement of a panel subject to different representations of a semi-empirical turbulent boundary layer fluctuating pressure model. [22]

parison of time-averaged responses showed good to excellent agreement between model and experiments. However, a comparison of the dynamic response was much less favorable. Power spectra of the panel response to SBLI are shown in Fig. 5 for several successive modeling cases: 1) a basic SBLI model that assumes a stationary shock position and spatially uncorrelated phase (blue line); 2) a stationary shock using a spatial TBL phase angle measured from the experiments (red line); and 3) prescribed (tuned) broadband shock unsteadiness (200 to 400 Hz, ± 4mm shock foot movement; green line). The large difference that results from using the measured phase angle instead of a spatially uncorrelated phase angle demonstrates the significance of this parameter in structural response prediction. Similarly, the panel is observed to be responsive to the broadband unsteady shock motion. These results highlight the importance of TBL / SBLI parameters such as spatial correlation and shock unsteadiness, and also the inability engineering level models for reliably forecasting the dynamic response of panels in such environments.

Clearly, a weak link in the process is the inadequate understanding and modeling of the unsteady boundary layer. However, as noted previously, improving this requires finely resolved computational domains and small time steps (relative to structural length and time scales), which hinders the broad use of high fidelity flow simulation in predicting the structural response in TBL/SBLI environments. This was recently highlighted by Ostoich et al. [29], who carried out a transient aeroelastic response prediction of a flexible panel interacting with a high-speed turbulent flow field using DNS. Notable differences in the statistics of the TBL were observed for the compliant vs. rigid surfaces. However, in order to maintain a tractable solution, the length and time scales of the panel responses were restricted to orders of magnitude smaller than that of a realistic structure. Thus, while few assumptions were made in modeling the fluid, the generality of the observed coupled responses remains unknown. Similarly, Visbal [28, 38] restricted the analysis of a panel subject to shock impingement to 2-D inviscid [38] and 2-D laminar [28] flow fields. This work demonstrated the potential for the introduction of structural instabilities due to shock impingement, as well as flow control with aeroelastic tailoring. However, the needs of the structural design community require extension of such analyses to 3-D structural configurations in turbulent flow conditions.

Experimentally, a few different groups have recently carried out study of TBL and SBLI on flexible surfaces. Jinks et al. [33, 39] found that the shock position and strength were sensitive to the shape and movement of

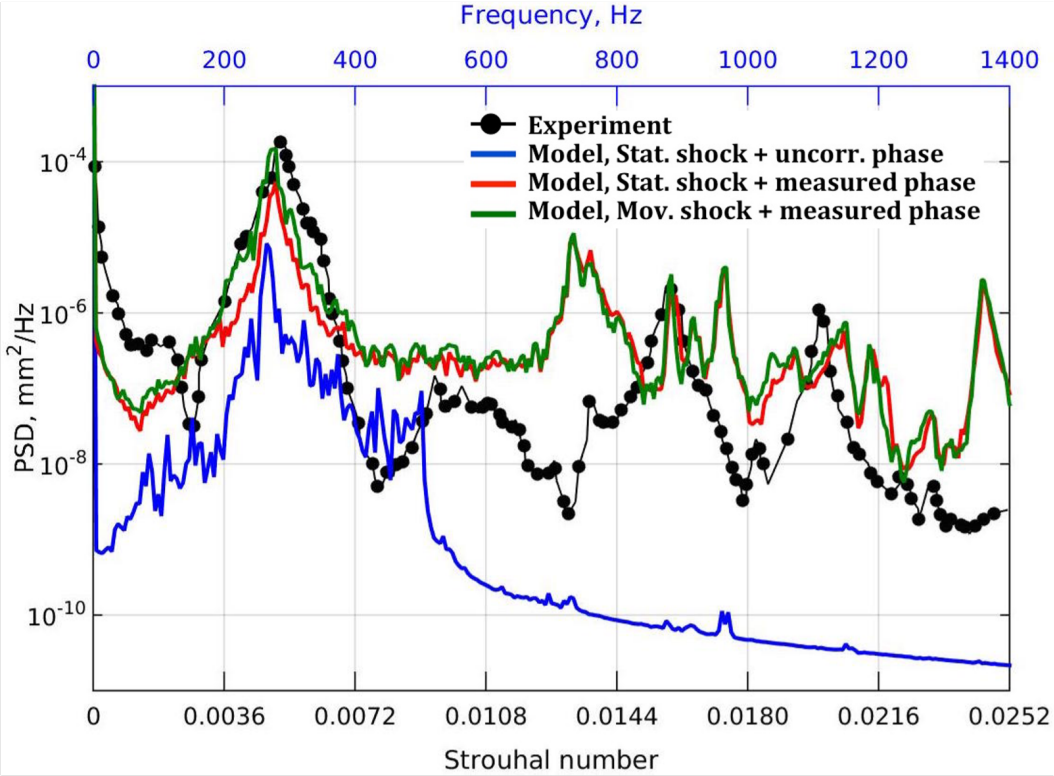

Figure 5: Power spectra of a panel response to SBLI. Strouhal number is based on boundary layer thickness. [25]

the panel surface downstream of the shock foot. This suggests a possible modification of the flow upstream of the shock due to downstream effects, which might contribute in a significant manner to the interaction between a flexible panel, the TBL, and a shock. Furthermore, the noted experiments carried out at AFRL/RQ by Spottswood et al. [6, 30] served as the benchmark for the computational study by Prof. McNamara's research group [24, 25]. For these studies, a 3-D panel response was considered by restricting displacements on all edges. Full field pressure and displacement measurements were made using pressure sensitive paint and digital image correlation, respectively. Panel temperature was monitored at one location near the frame, as a measure for ensuring thermal equilibrium between the panel holder frame and the panel. Results indicated mutual fluid-structural coupling. However, limitations in the measurement and analysis capabilities have hindered deep understanding of the mutual effect between the SBLI and the surface compliance [24, 25]. Similar issues were also faced by Willems et al. [31] at the DLR. In their work, they sought a 2-D study by only restraining the leading and trailing edges of the panel. Despite this, the fluid and structural response data indicated the presence of some 3-D effects– complicating the measurements, analysis and simulations. Furthermore, they did not attempt full field displacement data and restricted the CFD analysis to RANS. Thus, while dynamic fluid-structure interactions were detected in experiments, a full understanding of these interactions was not possible, again due to both measurement and modeling limitations.

The above survey of work highlights several inadequacies that severely limit understanding of TBL/SBLI on compliant surfaces. Computational studies using high fidelity analysis only considered 2-D laminar flows or unrepresentative structural configurations, while 3-D analysis of representative structures was carried out us-

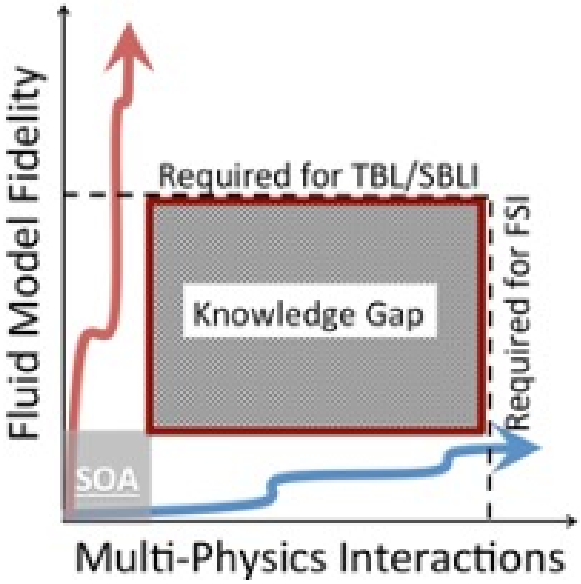

Figure 6: Knowledge gap due to orthogonal constraints that exceed the state-of-the-art for high-speed fluid-structural interaction research.

ing RANS CFD with semi-empirical corrections for TBL pressure fluctuations. Furthermore, experimental study was limited by both measurement and flow condition restrictions [6, 24, 25, 30, 31, 33].

The significant knowledge gap that arises is qualitatively depicted in Fig. 6. Direct coupling of high-fidelity flow solvers to nonlinear structural solvers for broad analysis and response prediction of structures operating in high-speed (Mach 2+) 3-D turbulent flow conditions is not feasible due to an inability to simultaneously achieve all structurally relevant length scales (O(100s to 1000s of mm)) and response records (O(mins)). Furthermore, lack of understanding of the fundamental physics and interactions obfuscates study using more tractable, but lower fidelity flow models. Thus, the current state-of-the-art is inadequate for meeting the orthogonal constraints necessary for a complete understanding of TBL/SBLI over compliant surfaces.

5 Technical Approach

The experimental setup (Section 5.1) and numerical simulations (Section 5.2) are detailed in this section. Experiments are performed in the Caltech Mach 4 Ludwieg Tube. Numerical simulations are performed using a sophisticated fluid-structure interaction solver framework. An extensively validated finite difference flow solver (Sec. 5.2.1) is coupled to the commercial finite element structural solver - Abaqus/Standard® (Sec. 5.2.2). The coupled solver is referred to as FDFEM (for the coupling between the Finite Difference and Finite Element Methods) and is detailed in Sec. 5.2.3.

5.1 Experimental Setup

5.1.1 Facility

The Caltech Ludwieg Tube, shown in Figure 7, consists of a driver tube that can be filled to a maximum pressure of 650 kPa, a Mach 4 axisymmetric nozzle, a test section with a 390 mm diameter, and a dump tank. During operation, the driver tube is separated from the test section and dump tank by a pneumatic piston valve which is suspended in the driver tube. The test section and dump tank are evacuated to a pressure of

200 Pa while the driver tube is filled to the desired pressure between 100 kPa and 650 kPa using bottled air as the test gas. The valve is then opened resulting in 60-80 ms of steady Mach 4 flow with a freestream velocity of 670 m/s and a unit Reynolds number of $5 - 25 \times 10^6$ per meter. For details on the facility and pneumatic valve operation see [40].

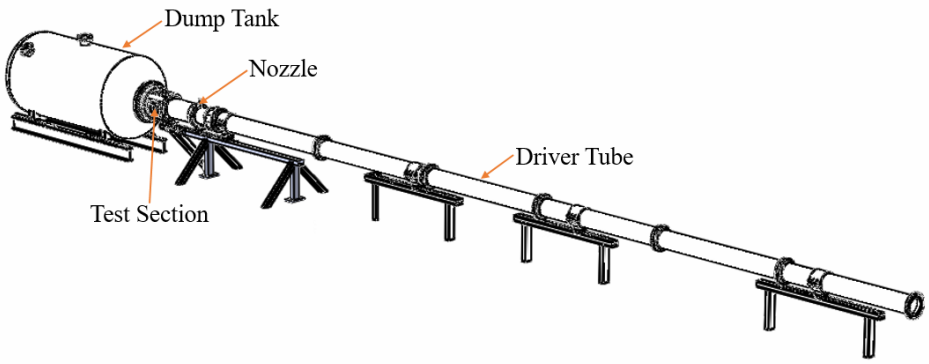

Figure 7: Caltech Ludwieg Tube with Mach 4 nozzle and test section. The overall facility length is 23.5m and the driver tube has a diameter of 300 mm.

5.1.2 Model Description

A CAD depiction of the full experimental setup, with the oscillating shock generator in place is shown in Figure 8. The setup consists of three main components: the oscillating wedge, the static flat plate model, and the panel inserts. The location of the oscillating wedge relative to the panel insert is designed using a series of Euler simulations described in Section 5.1.5. The mounting structure for the oscillating wedge allows the wedge to translate in the streamwise direction and also allows the wedge to move normal to the flat plate model. This allows the distance the shock travels and the interaction location to be changed between tests. Detailed looks at the two sub-assemblies are given in Figure 9.

The oscillating wedge sub-assembly is shown in Figure 9 (left). The sub-assembly is designed to fit into the existing circular window opening, 203 mm diameter, on the upper surface of the test section. This is done such that the assembly can be easily added or removed to the test section in one piece. The shock generator itself is an aluminum wedge with a 35 degree angle. Two rigid supports are connected to the wedge on a steel pivot rod. Nylon bushings are used to ensure that the wedge is able to oscillate smoothly and to prevent damage to the rigid supports. The shock generator is driven by a crank shaft connected to a Parker BE342KR brushless servo motor with a Bayside PX3-005 inline planetary gearhead with a 5:1 gear ratio. The motor with the gearhead has a maximum speed of 1000 rpm and a maximum torque of 15.6 N·m. The frequency of the oscillation is controlled by changing the speed of the motor. A more detailed description of the motor control is given in [41]. The wedge is connected to the crank shaft by a steel rod labeled as the crank rod in Figure 9 (left). The crank shaft is shown in detail in the zoomed in view of Figure 9 (left). As can be seen the crank rod is attached to the crank shaft by a pin. The crank shaft has a slot machined 1.5 mm off the crank centerline such that as the crank rotates the wedge oscillates 10 degrees. The slot has an oversized groove machined into it and a steel internal retaining ring is pushed into this groove. The crank pin is chamfered on the leading edge such that as it is pushed into place it expands the retaining ring into the

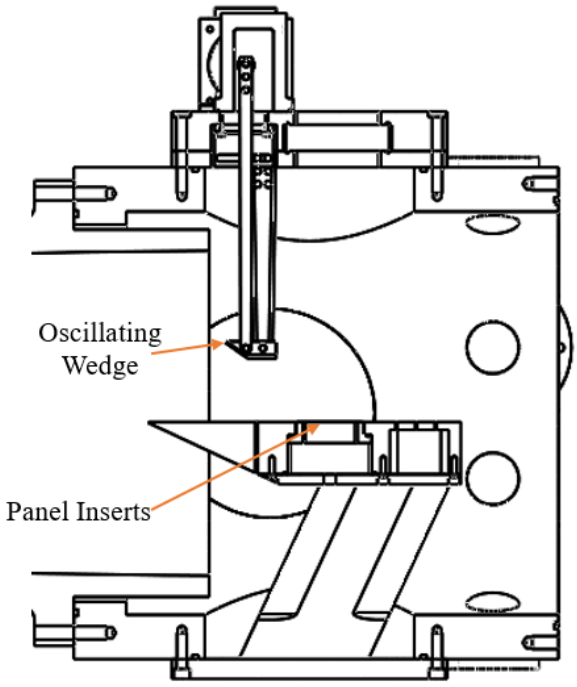

Figure 8: Experimental setup showing interchangeable panel inserts in sting-mounted model and the oscillating shock generator (top). Nozzle exit diameter is 315 mm. Flow direction is left to right.

oversized groove. Once the pin is in the correct position the retaining ring snaps into the groove on the pin locking it in place. The crank rod is held in place on the pin using a steel circlip. As can be seen in Figure 9 (left) the rigid supports and the crank rod have three different mounting holes. This allows for the shock generator to be moved normal to the flat plate model between tests, 32 mm in increments of 13 mm, giving additional control over how far the shock travels during an oscillation. In addition the shock generator is able to translate 15 mm in the streamwise direction. A rectangular window, 84 mm x 140 mm, is located behind the crank shaft assembly and provides visual access to the panel surface on the flat plate model.

The flat plate model, detailed in Figure 9 (right), is made of aluminum and is 292 mm long streamwise and 203 mm long spanwise. The model is supported from below by two steel stings to ensure that the model does not move under the loading imposed by the shock generator. The flat plate model has a maximum thickness of 51 mm and has a front wedge angle of 25 degrees. The flat plate model has two cavities labeled in Figure 9 (right). The first cavity is where the panel inserts are installed and has the ability to be pressure controlled. During experiments with the compliant panel inserts, a solenoid valve is utilized during the tunnel vacuuming process. The solenoid valve is open until the test section reaches the predicted freestream static pressure for the given run conditions at which point it is closed. This helps to ensure that the panel is deformed due to the TBL or SBLI phenomena only. The second cavity is not pressure controlled and provides access to five pressure taps behind the panel insert. The pressure taps behind the panel insert are organized in an ”L” shape with three taps 32 mm downstream of the panel, one on the panel centerline, one 19 mm off center, and the third 38 mm off center. The final two taps in the ”L” are on the panel centerline 51 mm and 70 mm downstream of the panel respectively. There is an additional pressure tap on the model

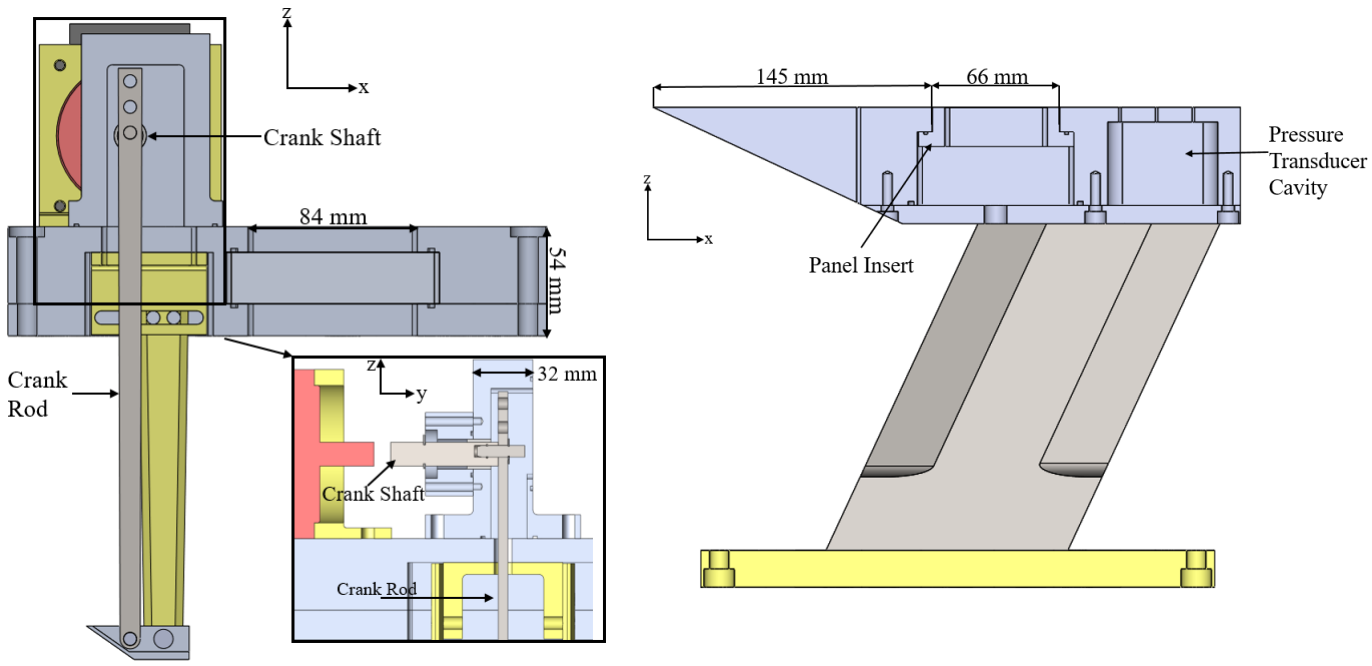

Figure 9: Experimental setup sub-assemblies: Oscillating wedge assembly (left). Flat plate model with compliant panel insert (right).

centerline, 38 mm upstream of the panel insert. The diagnostics will be described in detail in Section 5.1.4.

5.1.3 Panel Inserts

As stated earlier, all of the experiments are carried out with three different types of panel inserts. In each case the panel is 90 mm long spanwise and 66 mm long streamwise and is flush mounted in the flat plate model. The first class of model is the rigid flat plate. The rigid panel is machined from a single piece of aluminum and is 20 mm thick to ensure zero deflection during tests.

The second class of model is statically deformed geometries in the predicted panel modal shapes. Statically deformed panels are made in the three panel modes with the lowest natural frequencies. The shape and natural frequencies of the compliant panel are found from Equation 1 for a clamped rectangular panel given in [42].

$$f_{mn} = \frac{\lambda_{mn}^2}{2\pi a^2} \left(\frac{Eh^3}{12\gamma \left(1 - \nu^2\right)} \right)^{\frac{1}{2}} \tag{1}$$

where subscripts m and n refer to the number of half-waves in the spanwise and streamwise directions, a is the spanwise length, E is the elastic modulus, ν is Poissons ratio, γ is the mass per unit area, and λ is an experimentally determined constant that is a function of the modal indices, aspect ratio, and boundary conditions. The panels are 3D printed using a Polyjet process with a layer resolution of 0.03 mm. The panel geometries are specified by Equation 2. Each panel shape has an amplitude, A, of 0.7 mm which is 20% of the predicted turbulent boundary layer thickness at a driver pressure of 350 kPa. After the print, stair stepping was visible on the deformed surface of the printed parts. To eliminate this effect, the exposed

surface is painted with a thin layer of epoxy. The height of the deformed surface is then remeasured using a dial gauge with a 0.025 mm resolution. The three modal shapes with their corresponding predicted natural frequencies are shown in Figure 10. The first mode shape, 11, is a half wave with a positive amplitude, above the model surface, in both the streamwise and spanwise directions. The second mode shape, 12, is a full wave in the streamwise direction and a positive amplitude half wave in the spanwise direction. And the final mode shape, 21, is a positive amplitude half wave in the streamwise direction and a full wave in the spanwise direction.

$$z\left(x,y\right) = A\sin\left(\frac{m\pi x}{a}\right)\sin\left(\frac{n\pi y}{b}\right) \tag{2}$$

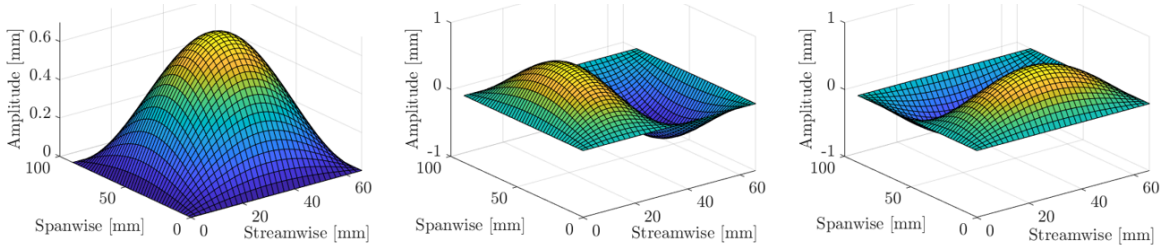

Panel 11
293.0 Hz

Panel 12
452.6 Hz

Panel 21
717.5 Hz

Figure 10: Statically deformed panel geometries, all dimensions in mm.

The third class of model is the thin, compliant panel insert. The compliant panels are made from 0.2 mm thick 316 stainless steel shim stock. The shim stock is sandwiched between to thicker pieces of material, to ensure the material does not deform during machining, and cut using a water jet. These panels are then measured at six location using calipers to ensure that the material is a uniform thickness. The water cut pieces are then adhered to a rigid base resulting in a compliant dimension of 80 mm spanwise and 55 mm streamwise with approximately clamped boundary conditions.

A series of roving hammer tests were performed to measure the natural panel frequencies using a PCB 086E90 modal hammer and two two-axis accelerometers, 11. The data are averaged over 10 impacts at each point. A comparison of measured and predicted frequencies is shown in Table 1.

Mode (Hz)	11	12	21	13
Predicted	293.0	452.6	717.5	722.0
Measured	293.0	500.5	775.2	875.9

Table 1: Predicted and measured panel frequencies.

5.1.4 Diagnostics

During the experiments, the flow is characterized using surface pressure measurements and high speed schlieren images. The pressure tap 38 mm upstream of the panel insert is instrumented with a Kulite XCS-093-5A pressure transducer. This transducer has a diameter of 2.4 mm and is equipped with a B screen. The pressure tap 32 mm downstream of the panel insert is instrumented with a Kulite XCS-062-5A pressure transducer. This transducer has a diameter of 1.7 mm and is also mounted with a B screen. The XCS series of pressure transducers uses a diaphragm design resulting in higher full scale outputs giving higher mV/Pa

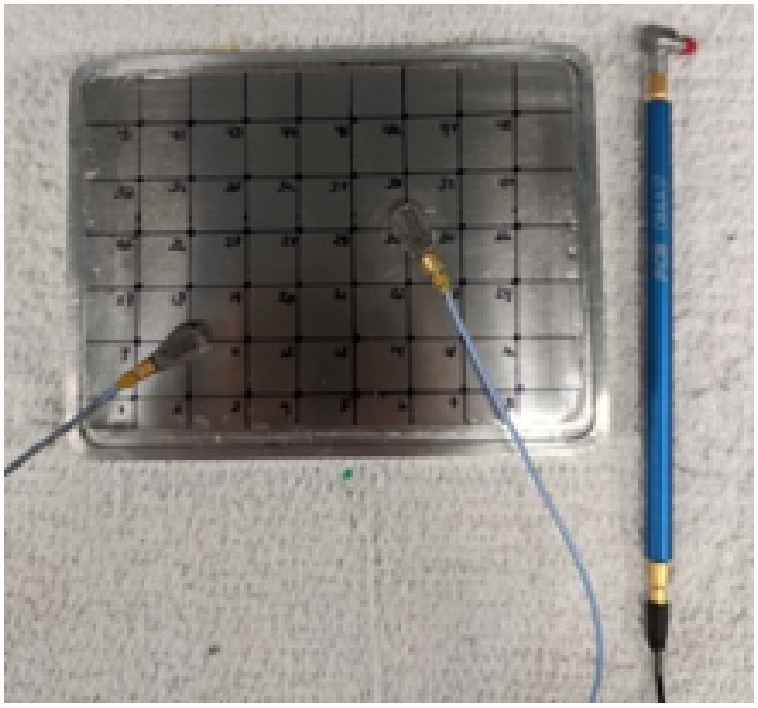

Figure 11: Compliant panel insert removed from plate model indicating node locations for roving hammer tests.

sensitivities and better signal to noise ratios when compared with similar transducers. Both transducers also have a natural frequency response of 150 kHz or greater which is well above the structural and forced flow frequencies of interest.

The pressure on the surface of the panel inserts is also measured using porous, fast-response pressure sensitive paint (PSP) from Innovative Scientific Solutions Inc. (ISSI). The paint consists of a polymer/ceramic base layer and a luminescent molecule, benzotrifluoride, coating. The PSP works by utilizing a molecule that interacts with oxygen in the flow. The luminescent molecule is excited by a light source causing it to absorb a photon and then release a photon of longer wavelength to transition back to the ground state. The molecule interacts with the oxygen in the test gas in such a way that the greater the partial pressure of oxygen the lower the intensity of the emitted photon. Thus, the output intensity of the paint gives an intensity map corresponding to the static pressure of the test gas on the surface [43]. The PSP used in these experiments is excited from above by a 532 nm wavelength, 200 mW laser light source (Spectra-Physics EXLSR-532-200-CDRH). The laser is first expanded through a -6 mm focal length biconcave lens and then dispersed by a 220 grit ground glass plate to illuminate the entire panel insert. The excited paint emits photons between 600 nm to 720 nm. The paint is imaged using a PCO 2000 CCD camera with a 600 nm cut-on longpass filter mounted above the test section looking through the rectangular window on the oscillating wedge assembly. Radiometric imaging with a long exposure time, 5 ms, is used to get high signal to noise ratio images with a relatively weak excitation source. In radiometric imaging, the camera averages over the entire duration of the camera exposure time. This image is compared to a ”wind-off” image taken at a known pressure before the test. The ratio of the ”wind-on” to ”wind-off” image eliminates effects of non-uniform excitation, paint thickness, and luminescent molecule concentration.

The flow is visualized using a high-speed Z-type schlieren system with 150 cm focal length concave mirrors. Two different light sources are utilized to visualize the flow. For mean flow measurements, a Cree X-Lamp MC-E cool white continuous LED light source is used. This light source provides high contrast images of the mean flow and works well for larger fields of view. However, with a continuous light source, the minimum exposure time is set by the camera and is typically on the order of 1 μs. This results in significant blurring of the instabilities in the flow. To lower the exposure time, a 905 nm wavelength laser diode (Laser Components 905D3S3J08) is used. The diode is controlled by a PicoLas LDP-V 03-100 UF3 laser diode driver. The diode is pulsed at widths between 20-100 ns resulting in lower camera exposure times and a more detailed image of the instabilities in the boundary layer. When the pulsed diode light source is used, a grated filter with 13 mm spaced gratings is substituted for the traditional sharp schlieren cutoff to reduce fringing around the knife edge. For more details of the Ludwieg Tube schlieren system see [40] and [44].

Photogrammetry is a non-contact, image based technique for determining the location of a point in space that appears in at least two images. By tracking a large enough number of points on a surface of interest this technique can be used to determine full-field surface deformations and motions. In this work, photogrammetry is used to obtain high-speed measurements of the compliant panel displacement. Whalen et al. demonstrated the use of this technique for FSI in high-speed flows in the NASA Langley 20-Inch Mach 6 Hypersonic Wind Tunnel [36]. At Caltech, a single-camera system has been designed and built, as detailed below.

The photogrammetric model used in this work is based on the work of Walker et al. to study the motion of insect wings [45]. For a point in space, shown in Figure 12 as X_A, there is a corresponding image point, x_a, on the projection plane (i.e. the camera sensor). A straight line drawn between the object point, X_A, and image point, x_a, passes through the perspective center, denoted as X_O in Figure 12. The line drawn perpendicular to the projection plane and intersecting the perspective center is known as the principal axis and the point at which the principal axis intersects the projection plane is the principal point. Two coordinate systems are utilized to define the location of the point. In 3D space the object coordinate system is utilized, and on the projection plane, the image coordinate system is used. The object coordinate system is located arbitrarily in 3D space while the image coordinate system is fixed with its origin at the perspective center. The z-axis of the image coordinate system runs along the principal axis while the x- and y-axes correspond to the horizontal and vertical axes of the projection plane respectively. Thus point X_A in Figure 12 has object coordinates: (X_A, Y_A, Z_A) and its corresponding projected image has image coordinates: $(x_a, y_a, -c)$, where c is the distance between the principal point and perspective center.

As described in [45] and in greater detail in [46, 47], the central perspective projection model described above is represented mathematically by the collinearity equations. The equations describe the linear relationship between any point in space X_A, the perspective center X_O, and the corresponding point on the projection plane x_a. The collinearity equations are given in equations 3 and 4 for the x and y image coordinates respectively.

$$x_{i,k} = \frac{-c_k[r_{k,11}(X_{O,k} - X_i) + r_{k,12}(Y_{O,k} - Y_i) + r_{k,13}(Z_{O,k} - Z_i)]}{[r_{k,31}(X_{O,k} - X_i) + r_{k,32}(Y_{O,k} - Y_i) + r_{k,33}(Z_{O,k} - Z_i)]} \tag{3}$$

$$y_{i,k} = \frac{-c_k[r_{k,21}(X_{O,k} - X_i) + r_{k,22}(Y_{O,k} - Y_i) + r_{k,23}(Z_{O,k} - Z_i)]}{[r_{k,31}(X_{O,k} - X_i) + r_{k,32}(Y_{O,k} - Y_i) + r_{k,33}(Z_{O,k} - Z_i)]} \tag{4}$$

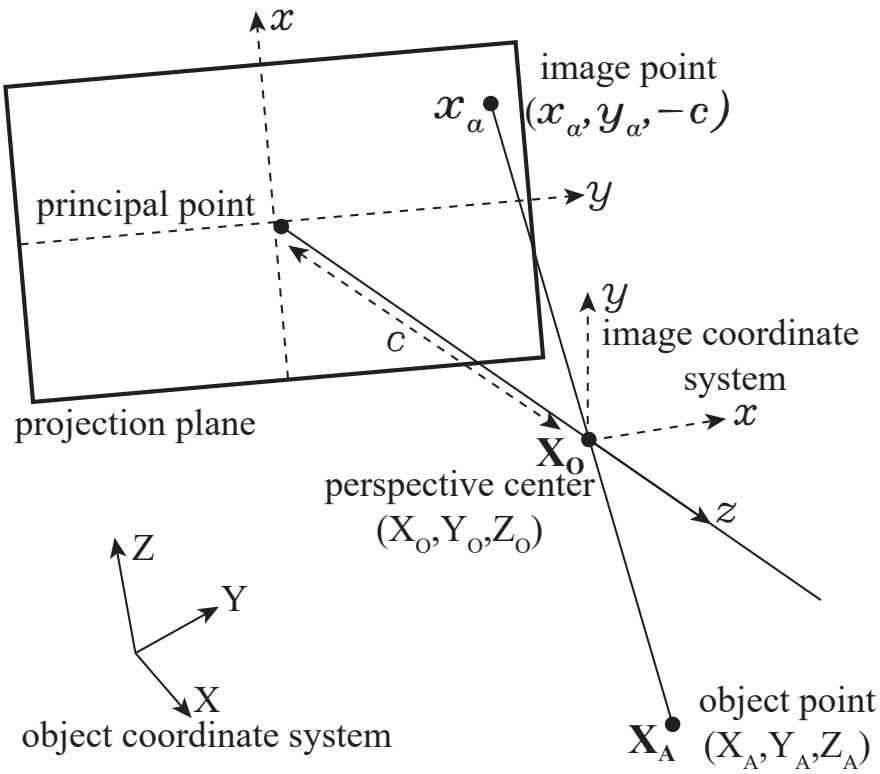

Figure 12: Central perspective projection redrawn from [45]. X_A is the object point in 3D space which is projected through the perspective c enter, X_O, creating the image point, x_a, on the projection plane.

In equations 3 and 4, the elements r_{11}, r_{12} ... are elements of a 3×3 rotation matrix which maps the object coordinate system to the image coordinate system, $k = 1, ..., m$ are the cameras, and $i = 1, ..., n$ are the points appearing in the images. Two images are required to solve the collinearity equations. In addition, to obtain a complete solution to the collinearity equations a camera calibration procedure is required. This procedure is described in the Calibration subsection.

As mentioned above, a minimum of two views of each point is required to determine the points located in the object coordinate system. Thus, photogrammetry is typically performed utilizing two or more cameras to obtain the multiple views of each point. However, in this work, a single Phantom v1612 high-speed camera was utilized. In order to obtain the two images of the surface points, a four-mirror adaptor system was implemented to image two different views of the surface on a single camera sensor. This system was utilized by Yu and Pan to perform single camera 3D digital image correlation (DIC) measurements [48]. A schematic of the optical system is shown in Figure 13.

In Figure 13 the panel surface is illuminated by and LED light source. The outside flat mirrors, M1 and M3, are mounted on rotating stages to allow them to rotate around the vertical axis. In this setup, M1 and M3 are 2 inch diameter flat mirrors. The central mirror pair is formed by a knife-edge right angle prism with two mirror coated legs. The mirror coated legs are each 1 inch long. Utilising a right angle prism mirror pair ensures that the central mirrors form a 90 degree angle to each other. A fixed focal length lens,

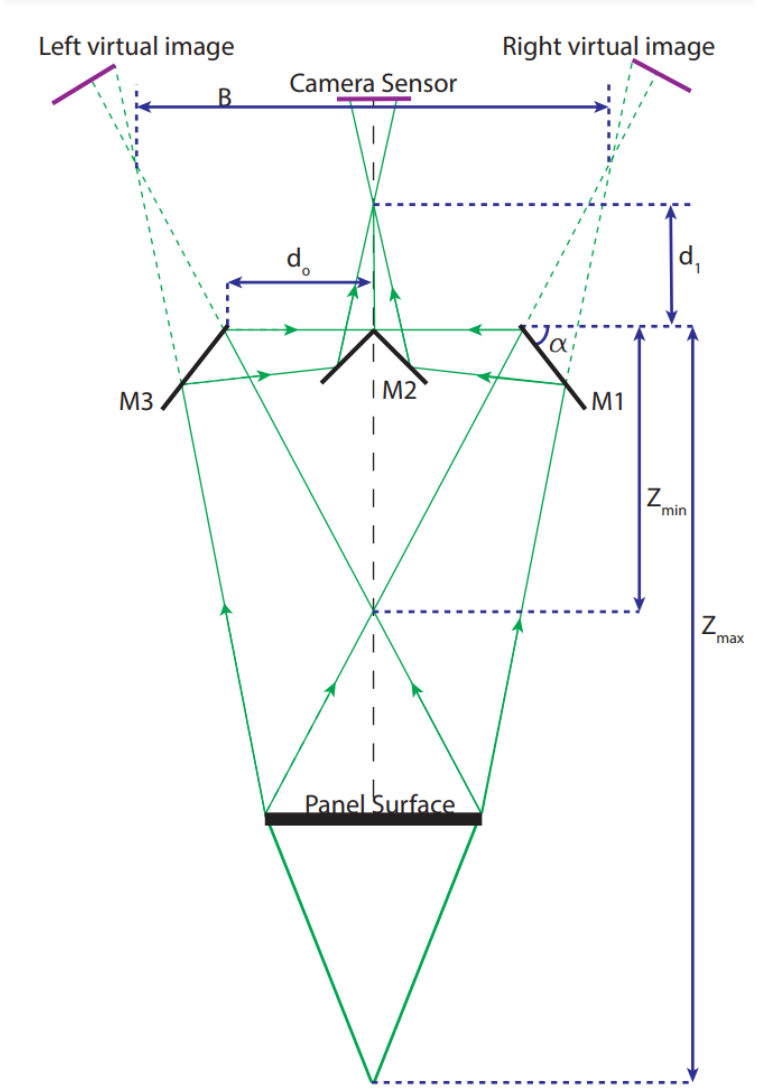

Figure 13: Single camera photogrammetry optical setup. M1 and M3 are 2” diameter flat mirrors and M2 is a right angle prism with two, 1” long, mirror coated legs.

determined by the desired field-of-view and distance to the panel surface, is used to focus the two images onto the camera sensor. The position of the outer two mirrors, M1 and M3, as well as the location of the lens are adjusted to form the two images on the camera sensor. The virtual image planes shown in Figure 13 correspond to the theoretical location of the cameras in a standard two-camera stereo imaging system to obtain the same two images as are seen on the camera sensor.

The size of each mirror, the angle of the outer mirrors, and the focal length of the lens were determined using the equations derived in detail by Yu and Pan in [48], and a brief overview is given here. The distances and angles utilised in the following equations are shown in Figure 13.

The first step is to determine the baseline distance of the system. In a traditional two-camera setup, the baseline distance is the distance between the two cameras. Here, the baseline distance corresponds to the

distance between the two virtual cameras. This distance is calculated using Equation 5.

$$B = 4d_0 \sin^2(\alpha) - 2d_1 \cos(2\alpha) \tag{5}$$

Where, d_0 is the distance from the outer mirror to the intersection of the mirror legs on the right angle prism, d_1 is the distance from the right angle prism to the focusing lens, and α is the outer mirror rotation angle. The next step is to determine the depth of the field of view using Equations 6 and 7.

$$Z_{min} = -\frac{B}{2}\tan(2\alpha) - (d_0 + d_1)\sin(2\alpha) \tag{6}$$

$$Z_{max} = -\frac{B}{2}\tan(2\alpha - \theta) - (d_0 + d_1)\sin(2\alpha);\ \theta = \tan^{-1}\left(\frac{ls}{2f}\right) \tag{7}$$

In Equation 7, ls is the size of the camera sensor and f is the focal length of the lens. The last parameters needed to design the four-mirror adaptor system are the size of the right angle prism mirror, L_i, the size of the outer mirrors, L_O, and the pose angle, α, of the outer mirror. These values can be calculated using Equations 8, 9, and 10 respectively.

$$\frac{d_1 \sin\theta}{\sin 45^\circ - \theta} \leq L_i \leq -\frac{\sqrt{2} d_0 \tan(2\alpha)}{1 - \tan(2\alpha)} \tag{8}$$

$$L_O \geq \frac{(d_0 + d_1)\sin\theta}{\sin(\alpha - \theta)} \tag{9}$$

$$45^\circ \leq \alpha \leq 90^\circ - \tan^{-1}\left(\frac{\frac{\sqrt{2}}{2}L_i}{d_0 - \frac{\sqrt{2}}{2}L_i}\right) \tag{10}$$

As can be seen, there is no upper limit on the size of the outer mirrors, L_O. However, if the outer mirrors are too small, the valid FOV is decreased and the illumination across the image can become uneven. If the outer mirrors are chosen to be very large, the system volume will also become very large. The size of the inner mirror pair, L_i, also can affect the valid FOV of the system if it is too small. However, in addition, if the inner mirror is too long the reflected light from the panel surface will be blocked by the inner mirror pair. The pose angle of the outer mirrors, α, is directly related to both the baseline distance, B, and the FOV. For an angle less than 45° there will be no common FOV between the two virtual cameras. For too large of a pose angle, however, the reflected light from the panel will be obstructed by the outer mirror. By utilising Equations 5-10 and varying d_0, d_1, α, and f the size of each mirror, the FOV of the system, and the baseline distance of the system can be determined for a wide variety of valid configurations.

Once the system is aligned as discussed in the previous section, the system must be calibrated using a known target. The calibration for this setup is done utilizing a bundle adjustment calibration routine provided by Walker et al. [45]. A bundle adjustment routine provides the optimal estimates of the camera parameters (principal distance, position vector, and rotation matrix for each camera) and the object coordinates given known image coordinates and knowledge about the relationship between the image points (distance between

each point). The calibration grid for this work is a printed card consisting of 2 mm circular points separated by 5 mm. The grid consists of 7 points in the x-direction and 8 points in the y-direction. The grid must have an unequal number of points in each direction for the calibration code to determine the target orientation. For each calibration a series of 20-30 images is taken of the calibration grid in a number of different orientations. The calibration must be done after each realignment of the photogrammetry system.

The photogrammetry images are split into the left and right images using a Matlab code. A single background image is taken and used on the entire data set to help remove noise. For each image we utilize top-hat filtering to obtain a background image. First, a morphological disk structuring element is created to be slightly larger than each of the imaged points. The top-hat filter takes this element and erodes it from the image, known as opening the image. This open image is then subtracted from the original image to obtain the background noise. This background noise is then Gaussian filtered to remove the noise added by utilizing the structured elements. Finally this background image is subtracted from the original image to obtain what we refer to as the normalized image. The normalized image is converted to a binary image, changing the foreground polarity to dark. The built in Matlab centroid finding function is used to calculate the centroids of each marker on the binary image. These centroids are used to locate the points but are not accurate enough to use in the 3D reconstruction. Limits may be set on where to look for centroids. A image processing code was written to sort the centroids, then select a region around each centroid to create a mask and uniform background intensity. A least squares Gaussian curve fit is applied to each imaged point to find the centroid location. The output of this is the centroid location in the small region which are then adjusted to locate the centroid on the full image.The final step is to use these centroids to calculate the 3D point locations.

Figure 14: Example images, Left: Normalized, Center: Background, Right: Binary

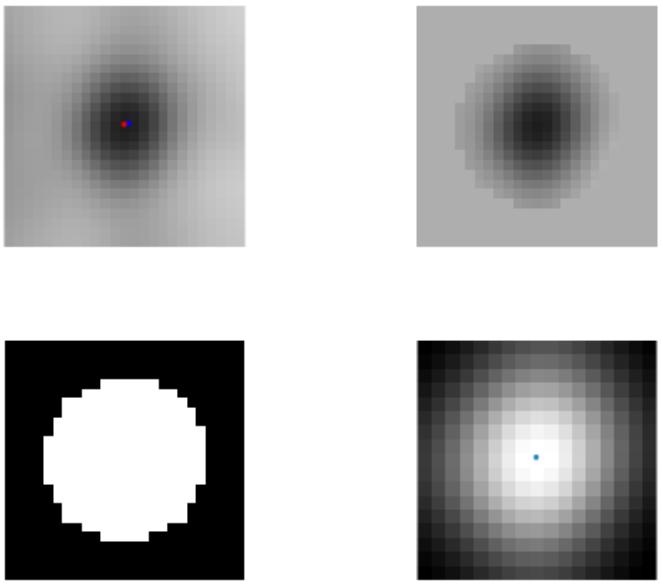

Figure 15: Masking of data points

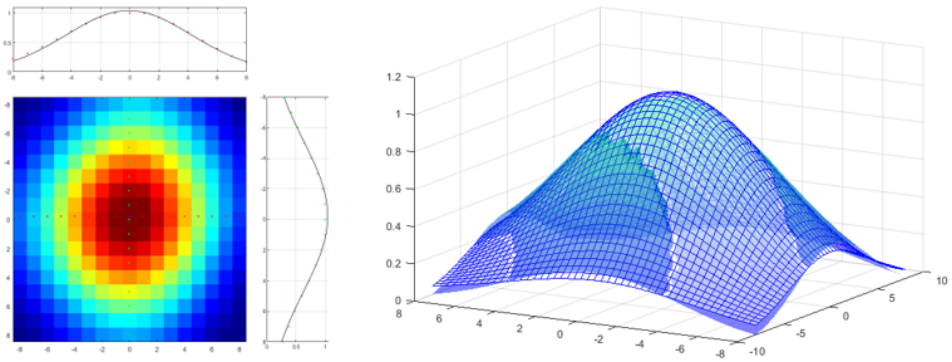

Figure 16: Gauss Optimization for a single point

The displacement of the compliant panel can also be measured at a point using a Keyence LK-G407 laser displacement sensor. The laser displacement sensor is a non-contact method of measuring point-wise displacements of a surface. The laser displacement sensor consists of a 650 nm solid-state laser light source and a CCD detector. The laser beam is projected onto the surface of the panel and the reflection is focused on the detector. As the surface moves the laser beam moves on the detector and through triangulation the surface displacement is found. The keyence LK-G407 has a measurement range of $\pm$ 100 mm, repeatability of 2 μm, and a maximum sample rate of 50 kHz.

5.1.5 Oscillating Wedge Simulations

Unsteady, two-dimensional simulations of the wedge oscillating above a plate are performed utilizing the AMRITA software system constructed by Quirk [49]. These simulations are used to estimate the location of the wedge, the angle of the wedge, and the amplitude of the motion needed to periodically load the panel insert. The AMRITA Euler solver for this application is an operator-split scheme with Harten-Lax-van Leer (HLLE) flux and kappa-monotone upstream-centered schemes for conservation laws (MUSCL) reconstruction. The AMRITA computations are carried out on a 200 x h coarse grid with each coarse cell corresponding to 1.6 mm. The height of the computational domain (h) is varied between 40 and 60 to set the distance between the wedge and the flat plate. One level of mesh refinement is applied to the coarse grid with a refinement ratio of 3.

The wedge and the plate are specified using a system of level set equations. In the computational domain, the panel is not specified, however, based on the scaling the panel is located from mesh points 90-130. The upper surface of the domain is extrapolated to allow the flow to expand behind the wedge; representing the fact that the wedge is not mounted on the upper wall of the test section. Because the simulation is inviscid, bluntness is added to the leading edge of the plate to create a pseudo boundary layer over the plate.

Pseudo-schlieren images from the AMRITA simulations are shown in Figure 17. The shock structure and the associated pressure rise at the plate surface is shown in the left images of Figures 17 and 18 respectively for the wedge in the initial position with the leading edge in line with the flow. At the beginning of the wedge motion, a double-Mach reflection is created as the shock from the leading edge of the wedge interacts with the plate. As can be seen in the initial configuration the pressure rises by a factor of 8.5 at the leading edge of the panel, and remains fairly constant over the front half of the panel before decreasing back to the freestream value. The shock structure and the associated pressure rise at the plate surface are shown on the right of Figures 17 and 18 for the wedge at the end of its oscillation. Through the AMRITA simulations it is found that the wedge needs to oscillate by 10 degrees in order to drive the pressure wave over the entire panel insert and maintain visual access to the panel surface. As can be seen by the time the wedge has finished the oscillation the shock structure has transitioned into a regular reflection. In this configuration, the pressure rise reaches a maximum value of just over 6 and does not remain at the peak value for as long as the Mach reflection pressure rise.

Figure 17: Numerical pseudo-schlieren snapshots for shock generator rotation angles of 0 (left) and 10 (right) degrees.

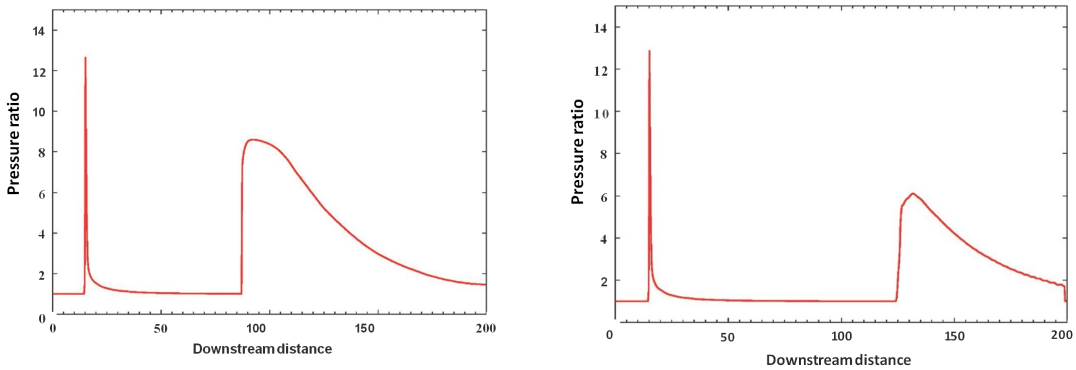

Figure 18: Pressure profiles over plate surface at times corresponding to schlieren images above with shock generator rotation angles of 0 (left) and 10 (right) degrees.

5.2 Numerical Simulations

5.2.1 Fluid Modeling

The flow field is governed by the full 3-D compressible Navier-Stokes equations, which are solved in curvilinear coordinates, $(x, y, z, t) \rightarrow (\xi, \eta, \zeta, \tau)$ with $t = \tau$ using the strong conservation form:

$$\frac{\partial}{\partial \tau}\left(\frac{\vec{U}}{J}\right) + \frac{\partial \hat{F}}{\partial \xi} + \frac{\partial \hat{G}}{\partial \eta} + \frac{\partial \hat{H}}{\partial \zeta} = \frac{1}{Re}\left[\frac{\partial \hat{F}_v}{\partial \xi} + \frac{\partial \hat{G}_v}{\partial \eta} + \frac{\partial \hat{H}_v}{\partial \zeta}\right] \tag{11}$$

where $\vec{U} = [\rho, \rho u, \rho v, \rho w, \rho E]^T$ is the conserved solution vector. Here u, v and w are the Cartesian components of the velocity, ρ is the density and E is the internal energy. $J = \partial(\xi, \eta, \zeta, \tau)/\partial(x, y, z, t)$ is the transformation Jacobian. Flow variables are non-dimensionalized by reference (∞) values, except for pressure, which is normalized by $\rho_\infty u_\infty^2$. The length scale is chosen to be the length of compliant surface in the streamwise direction (a). Thus, $Re = \rho_\infty u_\infty a/\mu_\infty$. More details on the inviscid and viscous fluxes are provided in, for example, [50]. The fluid is assumed to be a perfect gas, $p = \rho T/\gamma M_\infty^2$, where p, T, γ, and M_∞ are the pressure, the temperature, the ratio of specific heat (here $\gamma = 1.4$ is assumed), and the reference Mach number, respectively.

The second-order implicit time marching scheme of [51] is adopted, with two Newton-like subiterations to reduce factorization and explicit boundary condition application errors. Further details on the time scheme are provided in [52]. The spatial derivatives are discretized using a 6^{th} order compact finite difference scheme with the central difference, ensuring no dissipation error. However, to provide dissipation at high spatial wavenumbers in the implicit large eddy simulation context, a small amount of numerical dissipation is

added. Detailed validation studies may be found in [53], [54] and [55]. In shock regions, which are detected by a simple switch for specified threshold parameters [56], the high-order compact scheme is replaced by the classical Roe scheme with a 2^{nd} order central-difference formulation.

5.2.2 Structural Modeling

The equation of motion for the structural solver (Abaqus/Standard®) is,

$$M_s\ddot{\chi}(t) + C_s\dot{\chi}(t) + K_s\chi(t) = F_s(t), \tag{12}$$

where M_s, C_s and K_s are the structural mass, damping and stiffness matrices; while $F_s(t)$ and $\chi(t)$ are the fluid force and structural deflection at time t. The overdots indicate derivatives with respect to time. The structural equation (Eq. 12) is normalized by the flow reference quantities (*i.e.* ρ_∞ and u_∞) and the stream-wise length of compliant panel (a), similar to the flow solver (see Sec. 5.2.1). At present, the force term $F_s(t)$ comprises only induced by pressure (i.e., flow induced shear loads are neglected). Abaqus/Standard® uses the Hilber-Hughes-Taylor (HHT) time integration to solve Eq. 12, where the HHT operator is an extension of the Newmark β-method [57], viz.,

$$\dot{\chi}(t+\Delta t) = \dot{\chi}(t) + [(1-\gamma_s)\ddot{\chi}(t) + \gamma_s\ddot{\chi}(t)]\,\Delta t \tag{13}$$

$$\chi(t+\Delta t) = \chi(t) + \dot{\chi}(t)\Delta t + [(0.5-\beta_s)\ddot{\chi}(t) + \beta_s\ddot{\chi}(t+\Delta t)]\,\Delta t^2 \tag{14}$$

The numerical parameters γ_s and β_s are defined as,

$$\gamma_s = 1/2 - \alpha_s \;\text{ and }\; \beta_s = 1/4\cdot(1-\alpha_s)^2. \tag{15}$$

For $\alpha_s = 0$, the scheme is essentially the second order non-dissipative (energy preserving) trapezoidal rule, also known as the Newmark β-method with $\beta_s = 1/4$ and $\gamma_s = 1/2$. A default value of $\alpha_s = -0.05$ is used in the present simulations, which adds a small amount of damping for numerical stability. The implicit time stepping is solved using Newton's method; it is unconditionally stable for linear systems, and exhibits quadratic convergence for well-conditioned nonlinear problems.

5.2.3 Fluid-Structural Coupling

A detailed verification of FDFEM, in terms of a canonical test case of the inviscid panel flutter at Mach 2, is presented in [58]. Here we discuss both the one-way and two-way FDFEM solvers.

The finite difference and finite element solvers, described in Sec. 5.2.1 and Sec. 5.2.2 respectively, are coupled in a partitioned manner. A schematic of the fluid-structure interaction simulation strategy is shown in Fig. 19, depicting both the two-way (Fig. 19a) and one-way (Fig. 19b) FSI computations.

The FSI kernel of the two-way simulation (Fig. 19a) operates as follows:

a-1. Starting from initial and boundary conditions, the flow solver computes the wall pressure on the compliant surface at time $t = t_0$.

a-2. The wall pressure (p_{t_0}) is then transferred to the structural solver, which computes the deflection (χ_{t_1}), velocity ($\dot{\chi}_{t_1}$) and acceleration ($\ddot{\chi}_{t_1}$) response of the compliant surface.

a-3. The flow solver receives the new deflection, velocity and acceleration, which are used to deform the compliant surface boundary and the entire computational mesh. The procedure accounts for the Lagrangian-Eulerian effect by enforcing the geometric conservation law [59].

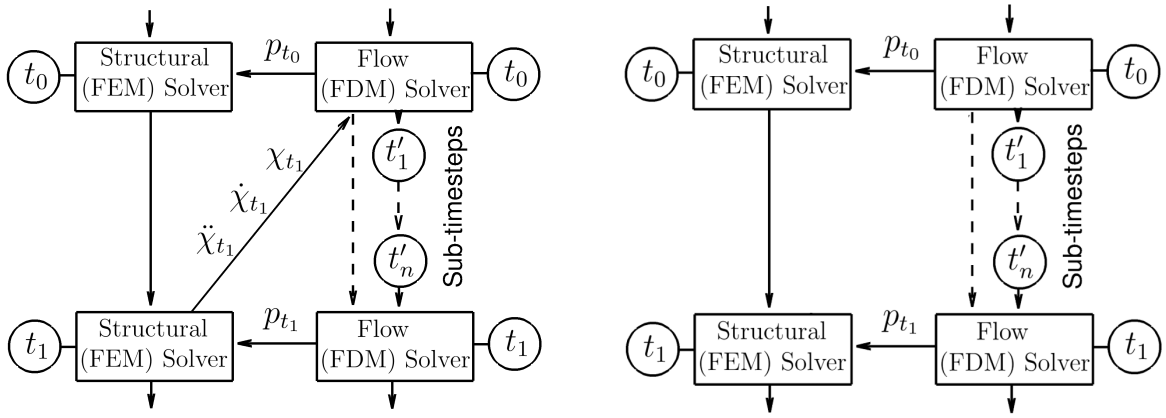

(a) Two-way coupling

(b) One-way coupling

Figure 19: Schematic of the fluid-structure interaction couplings between the finite difference and finite element solvers (FDFEM).

a-4. The flow time-step from $t = t_0$ to $t = t_1$ can be performed in multiple sub-timesteps, where the compliant surface deflection, velocity and acceleration are ramped over the sub-timesteps to provide the structure response at $t = t_1$. Sub-timesteps are useful in speeding-up the FSI computations (refer to [58]), particularly for fluid-structure systems with large scale disparity.

a-5. The wall pressure p_{t_1} at $t = t_1$ comprises the effect of deforming surface. The pressure p_{t_1} is then transmitted to the structural solver for the next time step, as shown in Fig. 19(a).

On the other hand, the one-way simulation, of Fig. 19(b), follows the steps a-1, a-2, and a-5, eliminating the steps a-3 and a-4 of the two-way simulation. The one-way FSI simulation can be also performed with a pre-computed flow solutions; this feature of FDFEM allows the use of existing CFD databases to examine the structural response.

In the message passing interface (MPI) framework, the head processors of the flow and structural solvers first complete their communications with the respective subordinate processors, and then exchange information across the solvers. A bi-linear interpolation facilitates the exchange of data between the two topologically different computational grids. The grid deformation in the flow domain is governed by Laplace's equation for the incremental changes in the structural deflection and velocity, respectively, as:

$$\nabla^2 \chi' = 0 \quad \text{and} \quad \nabla^2 \dot{\chi}' = 0, \tag{16}$$

where $\chi' = \chi(t + \delta t) - \chi(t)$ and $\dot{\chi}' = \dot{\chi}(t + \delta t) - \dot{\chi}(t)$, with the flow solver timestep of δt. At present however, Eq. 16 is solved in the wall normal direction only, neglecting the deflection and velocity of the flexible surface in the streamwise and spanwise directions. As noted before, the flow solver achieves second-order time accuracy by means of sub-iterations [59]. To this end, the sub-timesteps (of the flow solver in Fig. 19) exploit the disparity between the structural and flow physical scales to improve the time effeciency. However, since the solvers do not communicate during the sub-timesteps and flow sub-iterations, and no control of the time stepping in Abaqus/Standard® is possible, only a formally first order accurate time

advancement is achieved for the FSI responses. However, despite requiring smaller time steps to maintain time accuracy, computational time-to-solution is significantly improved by avoiding time intensive repeated interactions between the flow and structural solvers.

6 Results

6.1 Simulations of Static Deformation

The effects of static surface deformations on a spatially developing supersonic boundary layer flow at Mach number $M = 4$ and Reynolds number $Re_{\delta_{in}} \approx 49300$, based on inflow boundary layer thickness (δ_{in}), are analyzed by performing large eddy simulations. Two low-order structural modes of a rectangular clamped surface panel of dimensions $\approx 33\delta_{in} \times 48\delta_{in}$ are statically prescribed with modal amplitudes of δ_{in}. The effects of these surface deformations are examined on the boundary layer, including changes in the mean properties, thermal and compressibility effects and turbulence structure. The results are analyzed in the context of deviations from concepts typically derived and employed for equilibrium turbulence. Both Morkovin's hypothesis and strong Reynolds analogy break down in the near-wall region of the turbulent boundary layer. Modifications to the turbulence structure due to the surface deformations are elucidated by means of the wall pressure two-point correlations and anisotropy invariant maps. In addition to the amplification of turbulence, such surface deformations lead to local flow separation. One consequence of significance to practical design is the presence of low frequency unsteadiness similar to that encountered in impinging or ramp shock boundary layer interactions. The results and conclusions from this study are detailed here. Full details on the work are available in Ref. [60].

As stated, we consider the effect on turbulence of statically deformed rectangular panels that comply with basic modes arising commonly in fluid-structure interactions (FSI). This effectively breaks down the fully coupled problem into a geometrically simpler variant that isolates some of the crucial effects of surface deformations on the evolution of turbulent boundary layers and enables a better understanding of fully coupled interactions. To this end, a rectangular panel is statically deformed in its fundamental modes of vibration, namely, Mode(1,1) and Mode(2,1). The notation Mode(a,b) follows the convention that the first entry ('a') corresponds to the wave number in the streamwise direction (two times the number of cycles per unit panel length) and the second term ('b') corresponds to the wave number in the spanwise direction (two times the number of cycles per unit panel width). For concreteness, the geometric and flow parameters are chosen to be similar to those detailed in Section 6.5. Thus, the aspect ratio of the panel is fixed at 1.377 (the ratio of the spanwise to streamwise lengths), with modal deformation amplitude of 2.5% of the panel streamwise length, which equals the inflow boundary layer thickness (δ_{in}). These parameters generate a suitable response in the boundary layer, and simplify the task of identifying the impact of pressure gradients imposed by static surface deformations on the supersonic turbulent boundary layer. The specific areas of focus are turbulence structure, thermal and compressibility effects and flow unsteadiness.

The flow parameters are shown in Table 4. The Mach number (4) and other choices reflect those achieved in the Caltech Ludwieg Tube [61], where the corresponding experiments are being conducted (Sec. 6.5). Other attributes, including panel dimensions are presented in Table 4. Length scales are normalized by the streamwise length of the panel insert, a. Thus, the non-dimensional spanwise length of the panel insert (b/a) and inflow boundary layer thickness (δ_{in}/a) are 1.377 and 0.025, respectively, while the Reynolds number based on a is 1.57×10^6. The inflow boundary layer thickness is conveniently chosen to ensure a sufficient departure from the equilibrium state when subjected to surface deformations. The characterization of the inflow turbulent boundary layer, in terms of the boundary layer thickness and growth rate, is

Flow										
	M_∞	Re $(/m)$	P_0 (N/m^2)	T_0 (K)	p_∞ (N/m^2)	u_∞ (m/s)	ρ_∞ (kg/m^3)	δ_{in} (mm)	δ_{LE} (mm)	δ_{TE} (mm)
	4	2.375×10^7	5×10^5	290	3.3×10^3	674	0.17	1.65	2.60	3.70
Panel										
	a	b/a	δ_{in}/a	Re_a	A_m/a					
	1	1.377	0.025	1.57×10^6	0.025					

Table 2: Flow and panel parameters

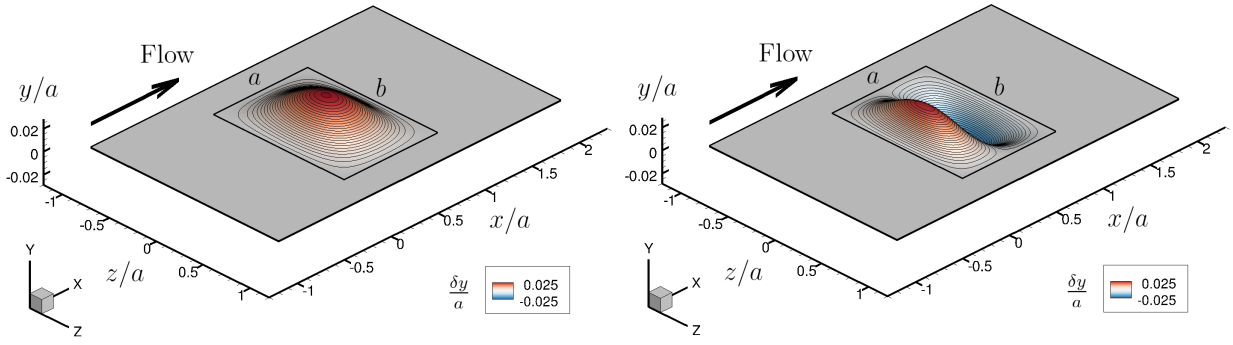

(a) Mode(1,1) (a) Mode(2,1)

Figure 20: Flow geometries with surface modal deformations: (a) Mode(1,1); (b) Mode(2,1).

performed by means of the same boundary layer edge detection procedure on the time-averaged schlieren images (in experiments) and density gradient magnitude (in simulations) [61]. A verification study on the inflow boundary layer characterization indicate that the simulated values of the boundary layer thickness at the leading and trailing edges of the panel and the growth rate are within 2.7%, 5.2%, and 11% of the experimental values, respectively.

In addition to the flat plate base case, the deflected surfaces with Mode(1,1) and Mode(2,1) surface deformations are considered to investigate the effect of surface static deformation. The geometries of the modal surface deformations of Mode(1,1) and Mode(2,1) are displayed in Fig. 20(a) and Fig. 20(b), respectively, with the peak modal amplitude A_m/a for the both cases is 0.025. This value is sufficient to distort the boundary layer to an extent that facilitates extraction of trends relative to the flat plate, with Mode(2,1) imposing the distortion twice as rapidly as Mode(1,1).

For perspective, an instance of the turbulent boundary layer obtained through LES is shown in Fig. 21 with normalized density. The leading and trailing edges of the panel insert are indicated by the vertical dashed lines. The boundary layer thicknesses at these locations are $\delta_{LE}/a = 0.029$ and $\delta_{TE}/a = 0.045$, respectively. A three-dimensional (3-D) view of the spatially developing TBL for all cases is shown in Fig. 22 using Q-criterion isosurface colored by velocity magnitude. The figure clearly shows the influence of surface deformation on flow turbulence, including especially rapid changes in the form and density of hairpin like flow structures due to the panel deflection, as they grow along the positive streamwise direction. These effects depend on the specifics of the deflection, and are discussed further below.

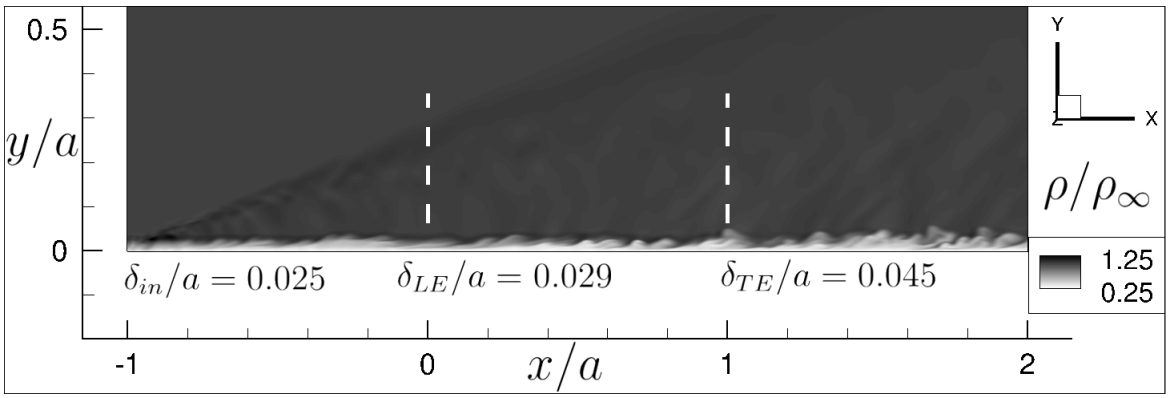

Figure 21: Instantaneous turbulent boundary layer over the flat plate model in terms of the normalized density (ρ/ρ_∞)

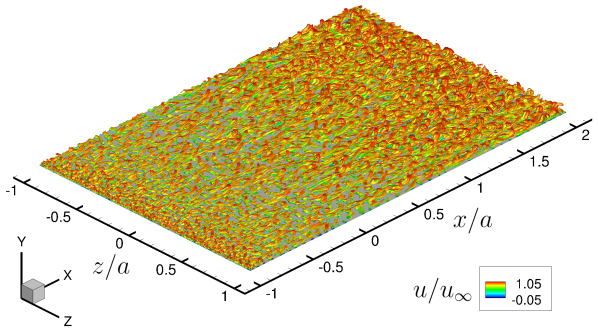

(a) Base case

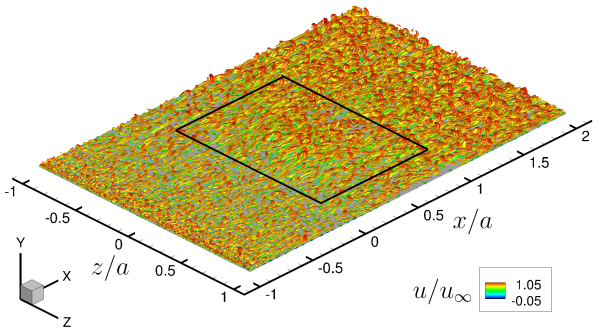

(b) Mode(1,1)

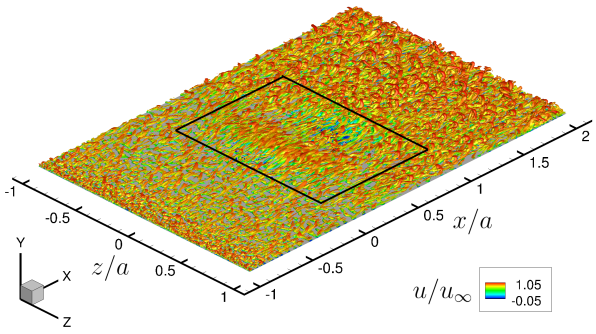

(c) Mode(2,1)

Figure 22: Three dimensional flow structures, displaying a Q criterion isosurface colored with streamwise velocity, developing over the Mode(2,1) configuration. The compliant panel is delineated by the black rectangle.

6.1.1 Modification of the boundary layer

In this section, we discuss the modification of the wall quantities of practical significance due to surface deformation in terms of the difference with respect to the baseline case. The time-mean wall pressure profiles $\Delta\langle p_w\rangle$ along the panel center-line ($z = 0$), normalized by the free-stream pressure $p_\infty = \rho_\infty u_\infty^2$, are displayed in Fig. 23(a) for the two cases: Mode(1,1) and Mode(2,1). As expected, the pressure profiles

for the two cases are identical in the inlet region of the computational domain ($x/a \lessapprox -0.25$), whereas the pressure profiles are considerably modified over the surface deformations for both cases, before returning to zero difference with the baseline in the downstream region ($x/a \gtrapprox 1.25$). The effect of surface deflection is reflected on the wall pressure slightly upstream of the leading edge of the panel (Fig. 23a), indicating the flow deceleration in the upstream near-wall region of the deflection. The deviation in the wall pressure profile occurs at an upstream distance of $\approx 5\delta_{in}$ ($\approx 0.125a$) for Mode(1,1) and $\approx 10\delta_{in}$ ($\approx 0.25a$) for Mode(2,1) from the panel leading edge. Comparing the two cases, the upstream influence length appears to scale linearly with the surface curvature at the panel leading edge, which for Mode(2,1) is approximately twice that for Mode(1,1), where a higher surface curvature corresponds to a smaller radius of curvature. However, in general, effects of the streamline curvature, compression and pressure gradient are closely related to each other and separating the influence of each is difficult [62]. The wall pressure profiles for Mode(1,1) and Mode(2,1), in Fig. 23(a), are modified with respect to the Base case over the streamwise extent of $-0.25 \lessapprox x/a \lessapprox 1.5$ due to the respective surface deflections of panel over $0 \leq x/a \leq 1$.

The modified wall pressure due to surface deflection is often estimated by means of simplified flow theories. For instance, for a surface deflection of δy, the time averaged wall pressure can be derived based on the second-order potential (quasi-steady supersonic) flow theory by Van Dyke [63] as:

$$\frac{\langle p_w(x) \rangle}{p_\infty} = \frac{1}{\sqrt{M_\infty^2 - 1}} \frac{d(\delta y)}{dx}, \tag{17}$$

The pressure profile for Mode(1,1) in Fig. 23(a) closely follows the profile of the gradient of surface deflection $d(\delta y)/dx$ as per Eq. 17, and it is also consistent with the correlation of streamwise gradients of the time-mean wall pressures, as shown in Fig. 23(b), to $d^2(\delta y)/dx^2$. However, significant deviations are evident from this correlation for Mode(2,1), most notably in areas corresponding to flow separation; this is consistent with the anticipated breakdown of simplified inviscid models for wall pressure in such regions. The modified time-averaged wall pressure profiles for the two cases along the spanwise direction at a streamwise location of $x/a = 0.75$ are displayed in Fig. 23(e).The wall pressures exhibit Gaussian-like profiles for both Mode(1,1) and Mode(2,1) in response to the corresponding surface deflections. The spanwise three-dimensionality introduced by Mode(1,1) and Mode(2,1) surface deflections is evident (Fig. 23e), where in general Mode (1,1) results in higher difference with the baseline, particularly at the centerline location ($z = 0$).

A measure of flow separation can be obtained by means of the skin-friction coefficient along the symmetry plane:

$$C_f = \frac{\langle \tau_w \rangle}{\frac{1}{2}\rho_\infty u_\infty^2} \quad \text{with} \quad \tau_w = \mu \frac{du}{dy}\bigg|_w, \tag{18}$$

where τ_w is the local wall shear stress on the wall. The effect of surface deflection on the skin-friction coefficient is shown in Fig. 23(c), where the ΔC_f is the difference between the respective deflected case and the baseline. Similar to the wall pressure profiles, the difference of the skin-friction profiles for Mode(1,1) and Mode(2,1) deviate from the Base case at about $x/a \approx -0.25$ and reunite downstream approximately at $x/a \approx 1.5$. For Mode(2,1), the difference in the skin-friction coefficient (Fig. 23c) becomes negative at $x/a \approx 0.069$ and also near $x/a \approx 0.478$, indicating two distinct regions of flow separation. The flow separation and reattachment locations are denoted by S and R, respectively, on the figure (Fig. 23c). The locations of flow separation are consistent with the stronger pressure gradients induced by Mode(2,1) surface

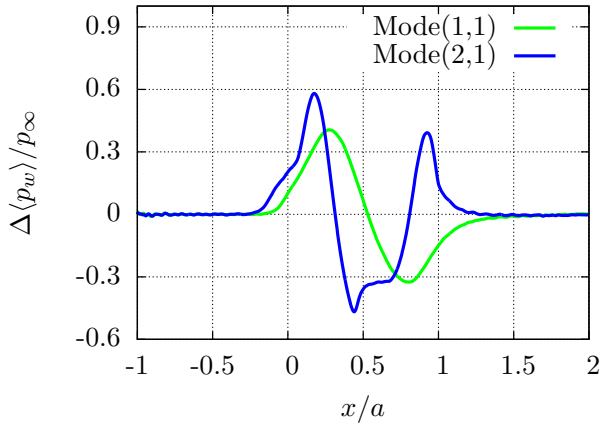

(a) wall pressure

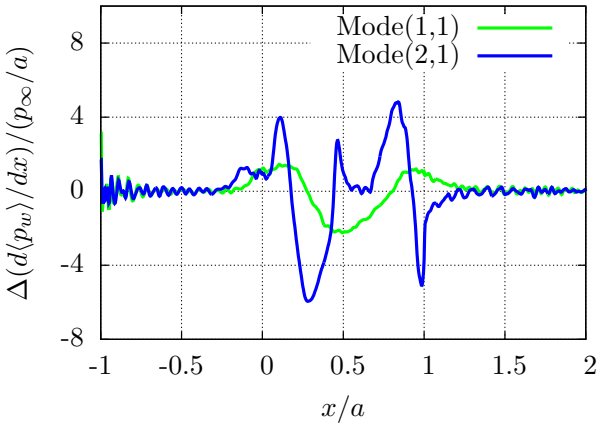

(b) wall pressure gradient

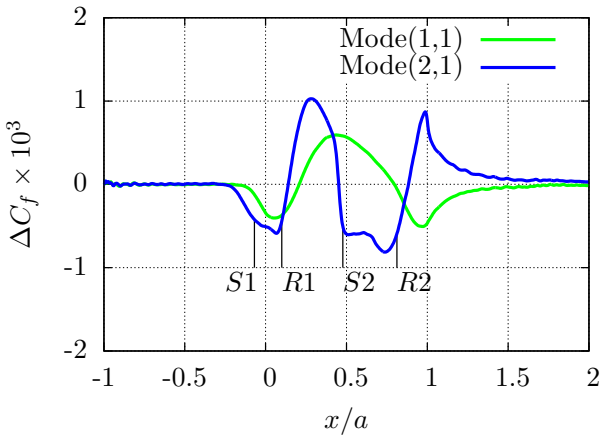

(c) skin friction coefficient

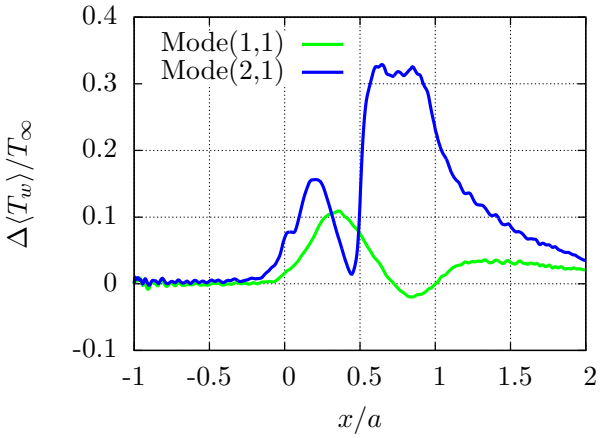

(d) wall temperature

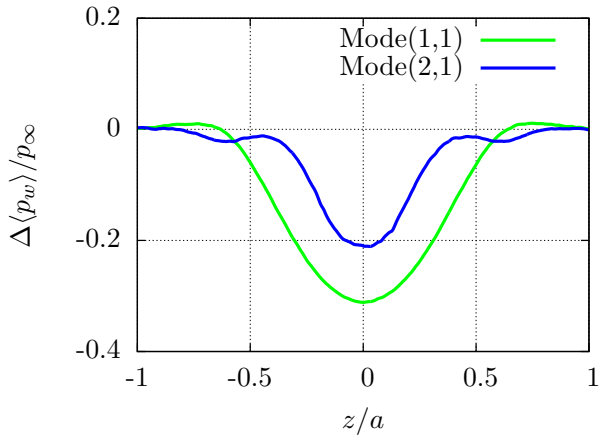

(e) spanwise wall pressure at $x/a = 0.75$

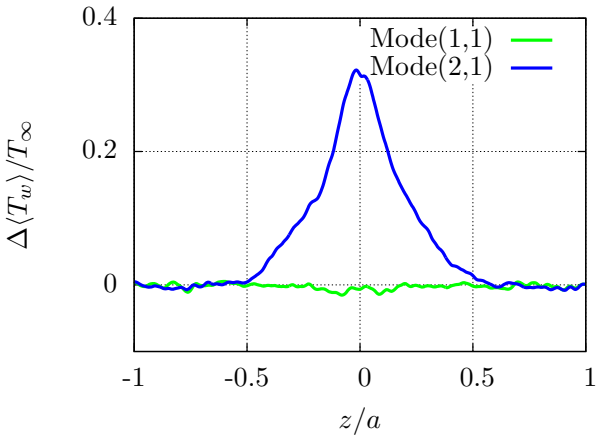

(f) spanwise wall temperature at $x/a = 0.75$

Figure 23: Comparison of the wall properties for the two cases (Mode(1,1) and Mode(2,1)) relative to the baseline. (a) Wall pressure, (b) wall pressure gradient, (c) skin friction coefficient, (d) wall temperature as function of streamwise location, (e) wall pressure along the span at $x/a = 0.75$ and (f) wall temperature along the span at $x/a = 0.75$.

deflections. The first region of separation forms near the leading edge of the panel in $-0.069 \lessapprox x/a \lessapprox 0.1$ with a separation length of $L_{s1}/a \approx 0.169$; whereas the second region of separation arises in $0.478 \lessapprox x/a \lessapprox 0.812$ with a separation length of $L_{s2}/a \approx 0.334$. For Mode(1,1), on the other hand, the skin-friction coefficient remains positive, in the time mean sense; however, the value near the leading edge of panel is nearly zero, suggesting the time-localized presence of separation in the unsteady flow. The streamwise variations in the skin-friction coefficient for Mode(1,1) and Mode(2,1) follow the pattern that high values occur at streamwise locations where the wall pressure gradient is favorable, such as in the vicinity of the apexes of the surface deflections.

At constant Reynolds number and adiabatic conditions, generally, an increase in the Mach number leads to the increase of the near-wall temperature and decrease of the near-wall density, resulting in a decrease of the skin-friction coefficient [62]. The time-mean wall temperature for Mode(1,1) and Mode(2,1) relative to the Base case ($\Delta\langle T_w\rangle/T_\infty$) are displayed in Fig. 23(d). The wall temperatures exhibit local variations due surface deformations, which gradually relax to the Base case wall temperature in the downstream region ($x/a \gtrapprox 1.5$). These variations are, to some extent, associated with the rise and fall of the wall pressures in Fig. 23(a), as well as with the flow separation regions for Mode(2,1). In addition to the wall pressure gradient, the wall temperature and flow separation appear to affect the skin-friction coefficient, particularly for Mode(2,1), which leads to much higher flow separation and temperature in $0.5 \gtrapprox x/a \gtrapprox 1.0$. The spanwise mean wall temperature variation for the two cases is displayed in Fig. 23(f), clearly indicating the wall temperature rise for Mode(2,1) along $x/a = 0.75$ inside the separated flow with a peak at the centerline ($z/a = 0$).

The shape factor, H, of a boundary layer provides useful information about the state of the boundary layer [64], particularly when its susceptibility to separation under adverse pressure gradients [65].

$$H = \frac{\delta^*}{\theta} \qquad \delta^* = \int_0^{\delta_x} \left(1 - \frac{\rho u}{\rho_\infty u_\infty}\right) dy \qquad \theta = \int_0^{\delta_x} \frac{\rho u}{\rho_\infty u_\infty}\left(1 - \frac{u}{u_\infty}\right) dy, \tag{19}$$

where δ^* and θ are the displacement and momentum thicknesses of the boundary layer. A theoretical estimate of the shape factor of an equilibrium supersonic TBL may be obtained by using a power-law relation for the mean velocity of an incompressible TBL [66, 67]. For instance, $u/u_\infty = (y/\delta_x)^{1/n}$ gives the velocity profile of a zero pressure gradient incompressible TBL, where n weakly depends on the Reynolds number (Re_x). This leads to $H_i = (2+n)/n$, where i stands for incompressible. Thus, for $n = 7$, the shape factor is $H_i \approx 1.26$. For a supersonic TBL over a flat surface with adiabatic wall condition, the shape factor can be expressed as, $H/H_i = 1 + r(\gamma - 1)M_\infty^2$, where r is the recovery factor [66]. For Mach number $M_\infty = 4$, the ratio of specific heats $\gamma = 1.4$ and the recovery factors of $r = 1$ and $r = 0.8$, the shape factor values are $H = 9.32$ and $H = 7.7$, respectively.

Figure 24 displays the variation of δ^*, θ and H with distance along the centerline ($z = 0$). Although the flow is not in equilibrium, particularly in locally separated regions, the integrations in Eq. 19 are nonetheless carried, estimating the local boundary layer thickness δ_x corresponding to $0.99u_\infty$. The profiles are significantly modified due to the presence of surface deformations in the Mode(1,1) and Mode(2,1). In general, a constant value of shape factor indicates a well-behaved zero pressure gradient turbulent boundary layer [64, 65]. The departure of profiles from equilibrium, due to surface deformation and/or pressure gradient, is marked by dashed lines in Fig. 24. The displacement thickness, in general, decreases for the positive slopes of surface deformation (concave curvature or compression effects) and vice versa; whereas the momentum

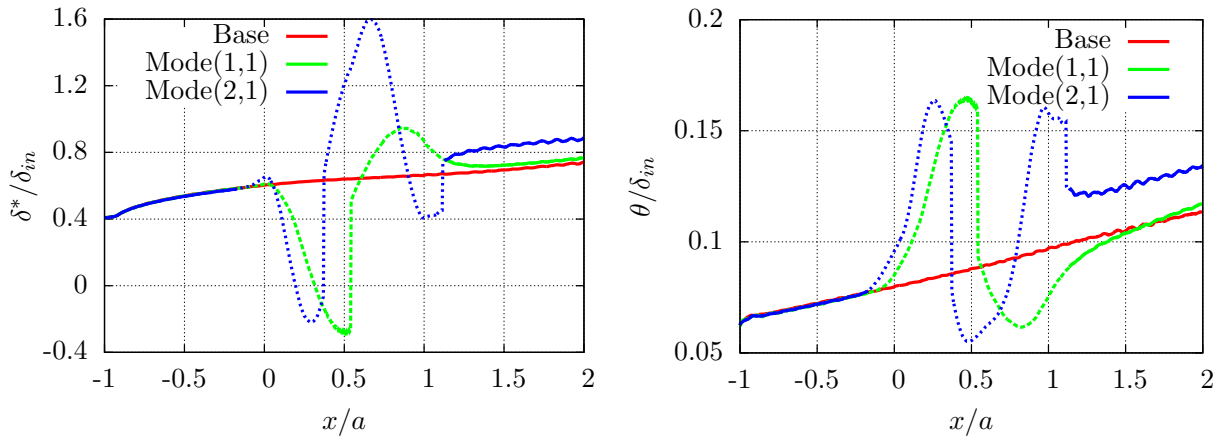

(a) displacement thickness

(b) momentum thickness

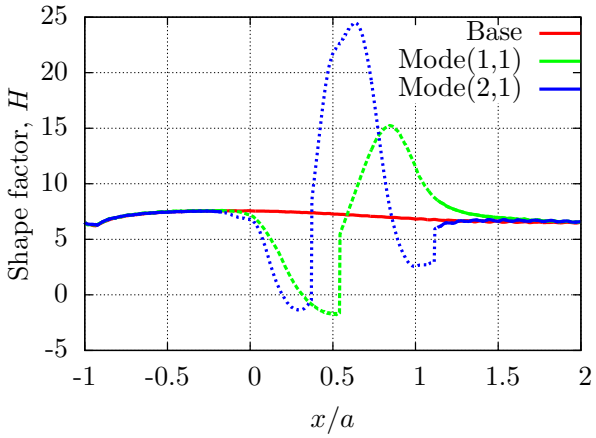

(c) shape factor

Figure 24: Streamwise evolution of the (a) displacement thickness, (b) momentum thickness, and (c) shape factor along the centerline $z = 0$ for the Base case, Mode(1,1) and Mode(2,1).

thickness exhibits opposite trends, where it increases for the positive slopes of surface deformation and vice versa. Furthermore, the shape factor mainly follows the variations in the displacement thickness (Fig. 24 c).

Similar to the displacement thickness, the shape factor decreases over the compression surfaces and increases over the expansion surfaces, as shown in Fig. 24(c). The higher values of shape factor indicate the regions of higher adverse pressure gradient where the flow is prone to separation, but only over the expansion surfaces: $0.5 \leq x/a \leq 1$ for Mode(1,1) and $0.25 \leq x/a \leq 0.75$ for Mode(2,1). For instance, we can infer about the possibility of separation at $x/a \approx 0.8$ for Mode(1,1) and the occurrence of separation at $x/a \approx 0.6$ for Mode(2,1). The shape factor for the three cases converge to a constant value of $H \approx 6.6$ for $x/a \gtrapprox 1.5$, returning to equilibrium; however, the downstream evolution of the turbulent boundary layer influenced by the effects of surface deflection [68]. In addition, the shape factor informs the effects of surface deformations from the boundary layer stability point of view. The rise or fall of the shape factor, in Fig. 24(c), corresponds to de-stabilization or stabilization of the boundary layer, respectively. This is consistent with the fact that convex curvature stabilizes the boundary layer, whereas concave curvature

destabilizes the boundary layer [67, 69]. Furthermore, after an initial adjustment, concave curvature leads to increase in the wall friction, heat transfer, and Reynolds stresses as well as it may give rise to Taylor-Görtler like vortices; on the other hand, the convex surface deformation typically results in opposite effects. The skin-friction and wall temperature of Fig. 23 are in agreement with these observations; however, the Taylor-Görtler like vortices, which contribute to enhancement of the flow turbulence, are not observed.

In addition to these opposite effects of the concave and convex curvatures, the supersonic TBL responds differently in the near-wall region as opposed to the outer region of boundary layer, in terms of the turbulence kinetic energy and mean streamwise velocity. However, for the present parameters, the effect of combinations of curvatures, such as in Mode(2,1), do not produce a linear superposition of the two; this contrasts with the linear superposition observed for a single surface curvature and a pressure gradient by [70]. The boundary layers in Mode(1,1) and Mode(2,1), which are distorted due to the surface deformations, relax to an equilibrium state (zero pressure gradient state) at a distance of $\approx 0.5a$ ($\approx 20\delta_{in}$) downstream from the trailing edge of panel. The time-averaged streamwise velocity and Reynolds stresses at this location ($x/a = 1.5$) for the three cases are displayed in Fig. 25. The streamwise velocity for Mode(1,1) and Mode(2,1) exhibits a decrease and an increase respectively when compared to the Base case in $0 < y/\delta_{x/a=1.5} \lessapprox 0.2$, the near-wall region of the boundary layer; whereas in the outer region, the distorted profiles are nearly recovered (Fig. 25 a). The streamwise component of Reynolds stress tensor, $\langle u'u' \rangle / u_\infty^2$, exhibits a slight decrease in its peak values for both Mode(1,1) and Mode(2,1) compared to the Base case. On the other hand, the wall-normal ($\langle v'u' \rangle / u_\infty^2$), spanwise ($\langle w'w' \rangle / u_\infty^2$) and the off-diagonal $\langle u'v' \rangle / u_\infty^2$ components of the Reynolds stress tensor are significantly increased in the near-wall region, indicating an overall increase of the turbulent kinetic energy.

The strength of the boundary layer distortion can be quantified in terms of an additional strain rate, e, and the primary strain rate, $\partial\langle u \rangle / \partial y$ [71]. $e/(\partial\langle u \rangle / \partial y) \lessapprox 0.01$ and $e/(\partial\langle u \rangle / \partial y) \gtrapprox 0.01$ represent weak and strong distortion values, respectively. The primary strain rate provides the measure of eddy strain rate, estimated by $(-\langle u'v' \rangle)^{1/2}/L_\epsilon$, where u' and v' are the fluctuating streamwise and wall-normal components of velocity and L_ϵ is a dissipation length scale. The flow or eddy response time scale can be approximated by the turbulent kinetic energy (TKE) per unit rate of TKE production [72], and it is inversely proportional to the primary strain rate. Furthermore, the characteristic time scale of turbulence, T_t, can be also defined based on the integral length scale of turbulence (L_t) and the root mean squared (*rms*) velocity fluctuations u'_{rms} as, $T_t = L_t/u'_{rms}$ [73]. The distortion is termed as rapid when a characteristic time scale of the turbulence (T_t) is much larger compared to the distortion time T_d, that is $T_d/T_t \ll 1$.

Rapid distortion theory (RDT) considerations [74, 75] can provide insights into the interpretation of the observations. The distortion time for the Mode(1,1) and Mode(2,1) can be estimated based on the streamwise lengths of $a/2$ and $a/4$ respectively and the sound velocity c; where the distortion length corresponds to the distance of the first peak of surface deflection from the panel leading edge. This results in the time scales of $T_d \approx 2$ and $T_d \approx 1$ for Mode(1,1) and Mode(2,1) respectively, where the values are also equal to the respective gradient Mach number. The integral length scale (L_t) of turbulence is typically associated with most energy producing turbulent eddies; for turbulent boundary layers, this length scale can be assumed to be δ, a local value of the boundary layer thickness. Thus the turbulence time scale is approximately $T_t \approx 0.2$, leading to $T_d/T_t \approx 10$ for Mode(1,1) and $T_d/T_t \approx 5$ for Mode(2,1). Evidently, the ratio T_d/T_t is much larger than 1 for both the cases, contrary to the assumption of $T_d/T_t \ll 1$ in the rapid distortion theory, indicating that the boundary layer distortions are not rapid.

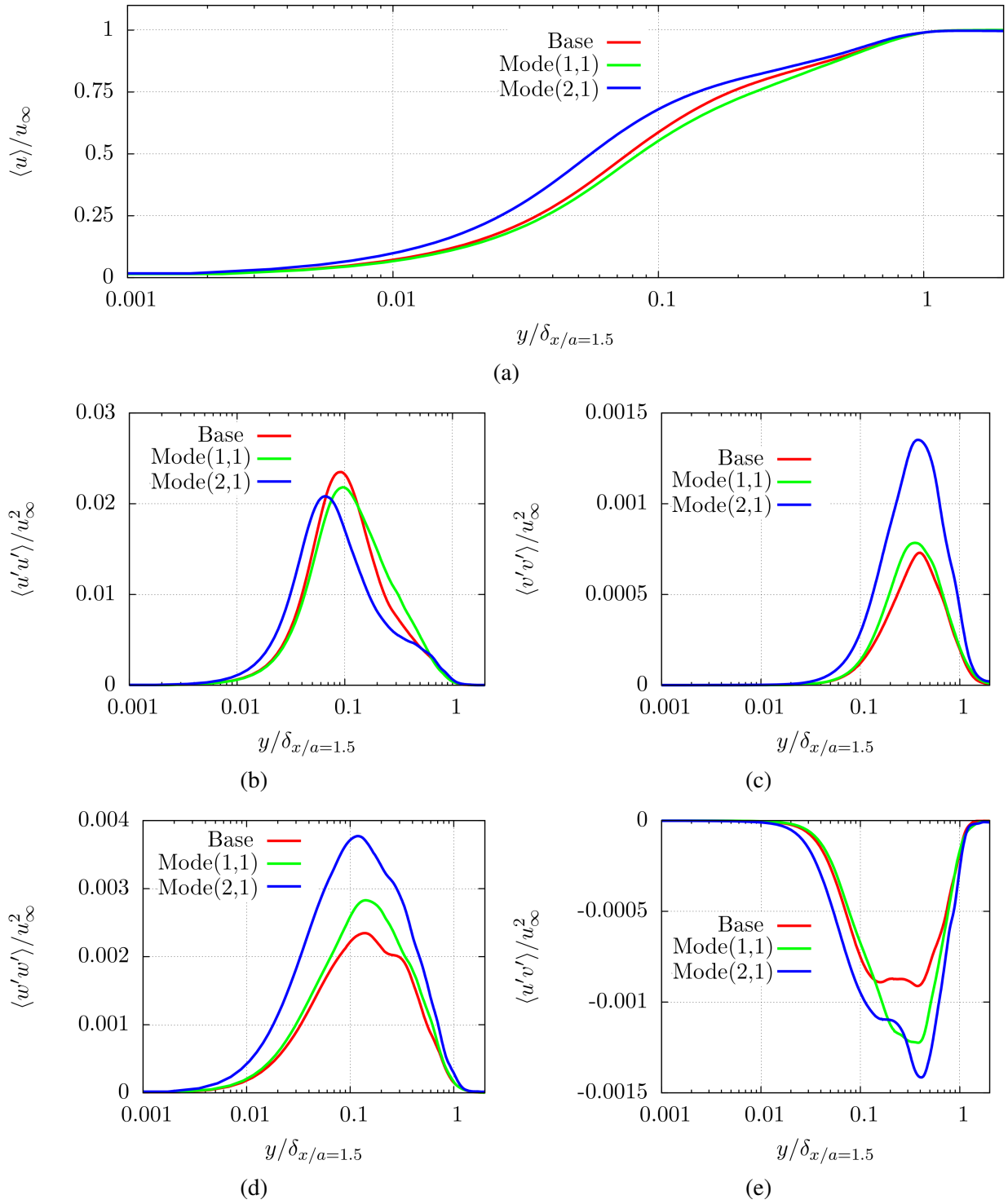

Figure 25: (a) Time-mean streamwise velocity and (b)-(e) Reynolds stresses a downstream location $x/a = 1.5$ for the three cases.

Loc.	$L1$	$L2$	$L3$	$L4$	$L5$
x/a	-0.5	0.0	0.5	1.0	1.5

Table 3: Streamwise reference locations on the wall surface ($y/a = 0$) along the domain centerline ($z/a = 0$).

6.1.2 Compressibility and thermal effects

The implications of panel deflections are now examined in the context of Morkovin's hypothesis [76], specifically that key features of incompressible turbulence persist in the supersonic regime ($1.5 \lessapprox M_\infty \lessapprox 5$) without significant modifications, other than mean density variation. Beyond $M_\infty \gtrapprox 5$, compressibility effects, in addition to the velocity and pressure fluctuations, density and temperature fluctuations may also affect the different mechanisms of energy exchange among the turbulence scales. The relations between the velocity and temperature fluctuations, encapsulated in the strong Reynolds analogy (SRA), can be considerably affected due to the higher levels of the acoustic and thermal fluctuations.

The turbulent Mach number,

$$M_t = \frac{\sqrt{\langle u_i' u_i' \rangle}}{\langle c \rangle}. \tag{20}$$

often employed with a threshold of $M_t \approx 0.3$ for the appearance of compressibility effects on turbulence [67], is plotted Fig. 26 at the different streamwise locations of Table 3. For all cases and locations, the turbulent Mach number is lower than the threshold of 0.3 for compressibility, indicating, in the equilibrium case, the applicability of Morkovin's hypothesis and strong Reynolds analogy by this measure. The analysis was also be conducted in terms of the fluctuating Mach number (M_f), which takes into account the variation in the speed of sound [62]:

$$M_f = \sqrt{\langle M^2 \rangle - \langle M \rangle^2}. \tag{21}$$

The results were again analyzed at locations ($L2$, $L3$, $L4$ and $L5$) (not included for brevity). The maximum values of M_f in all cases remain less than the threshold of 0.3 considered necessary to manifest the special effects of compressibility on turbulence. Although the profiles for Mode(1,1) and Mode(2,1) deviate from the Base case in the region of the panel, particularly at the mid-chord ($L3$) and trailing edge ($L4$) locations (see Fig. 26), they recover relatively rapidly towards the Base case profile within half the panel length downstream, by location $L5$.

We now examine the effect of the panel distortion on interactions between the thermal and velocity fluctuations, which are typically assumed small for equilibrium boundary layers when $1.5 \lessapprox M_\infty \lessapprox 5$. The relevant parameter is the turbulent Prandtl number Pr_t, which is the ratio of turbulent momentum to turbulent heat diffusivities. Typical considerations assume a Pr_t of unity for Reynolds analogy considerations to derive the correspondence between velocity and temperature profiles. The assumption of negligible total temperature fluctuations for adiabatic walls leads to the strong Reynolds analogy (SRA).

$$\frac{T'_{rms}}{\langle T \rangle} = (\gamma - 1)\langle M \rangle^2 \frac{u'_{rms}}{\langle u \rangle} \tag{22}$$

$$\frac{\langle u'T' \rangle}{u'_{rms} T'_{rms}} = -1, \tag{23}$$

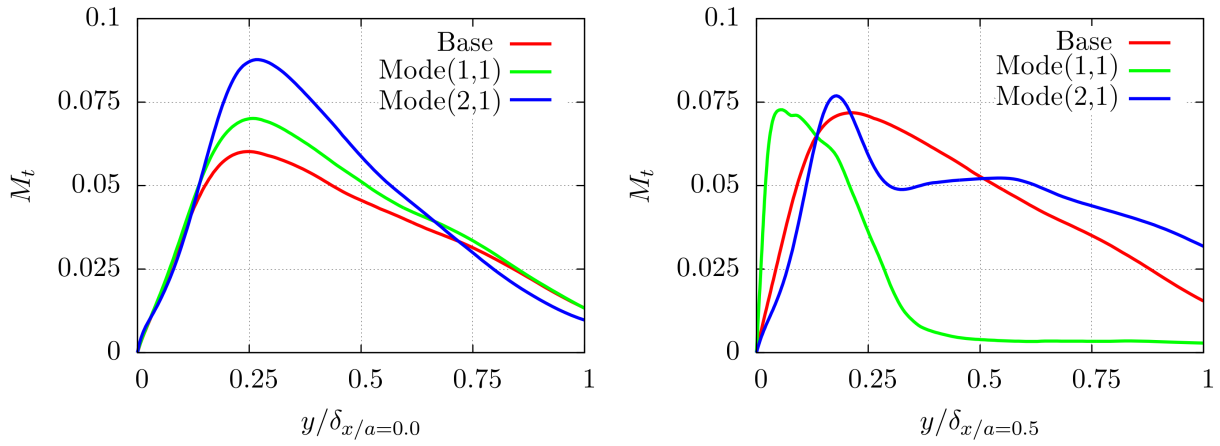

(a) $L2$ (panel leading edge location)

(b) $L3$ (panel mid-chord location)

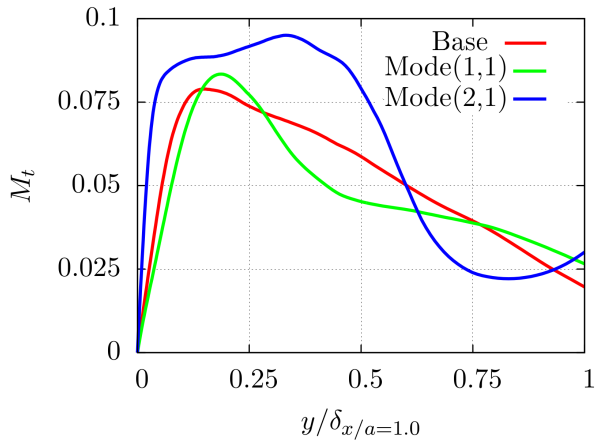

(c) $L4$ (panel trailing edge location)

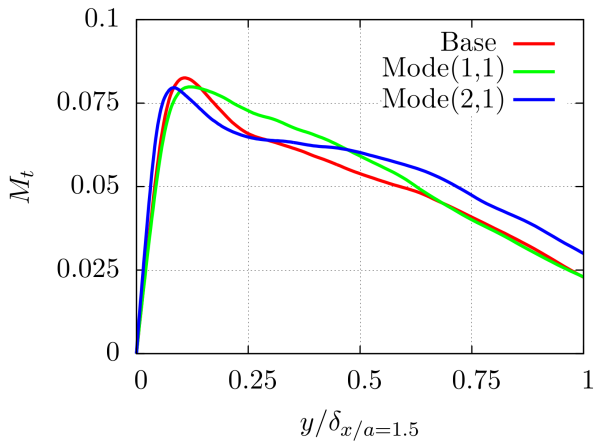

(d) $L5$ (a downstream location)

Figure 26: Turbulent Mach number (M_t) wall normal profiles for the three cases at (a) the leading edge of panel (b) at the center of panel (c) at the trailing edge of panel and (d) at $x/a = 1.5$ on the surface and at $z/a = 0$. For locations detail refer Table 3.

The simulations specify $Pr = 0.72$ for air, which affects the underlying assumption. Nonetheless, the application of the SRA greatly aids analysis and motivates an examination of its accuracy in the presence of the surface deformation. The SRA relation of Eq. 22 is examined at two streamwise locations: the panel mid-chord location $L3$ and downstream location $L5$ at $x/a = 1.5$ in Fig. 27(a) and Fig. 27(b) respectively. The figures display the ratio $(T'_{rms}/\langle T\rangle)/\big((\gamma-1)\langle M\rangle^2 u'_{rms}/\langle u\rangle\big)$ as a function of the wall distance (y/δ_x) with deviations from unity being the primary consideration. For the Base case, the ratio remains nearly constant at ≈ 0.8 for most of the boundary layer ($0.05 \lessapprox y/\delta_{x/a=0.5} \lessapprox 1$) at both the mid-chord and downstream locations ($L3$ and $L5$), closely following the SRA. However, in the close vicinity of the wall for $y/\delta_x \lessapprox 0.06$, the left hand side (LHS) of Eq. 22 becomes significantly higher compared to the right hand side (RHS), indicating the dominance of thermal effects. In the presence of surface deformations, the ratio of LHS to RHS of Eq. 22 reduces to a minimum of ≈ 0.35 for Mode(1,1) between $0.35 \lessapprox y/\delta_{x/a=0.5} \lessapprox 1$ as shown in Fig. 27(a); whereas for Mode(2,1), it drops significantly in the near-wall region for $y/\delta_{x/a=0.5} \lessapprox 0.06$ due to the negative streamwise velocity inside the flow separation. Nevertheless, at the downstream location $L5$,

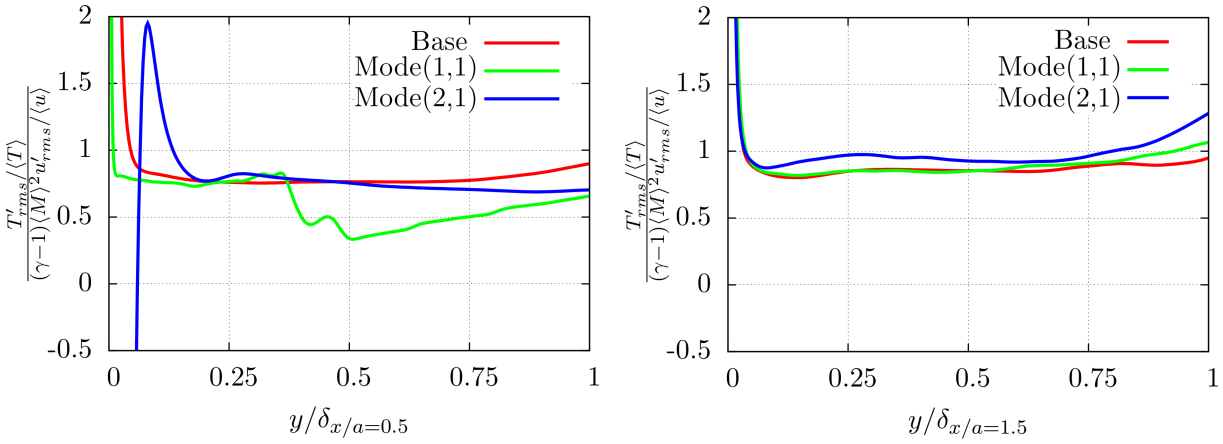

(a) $L3$ (panel mid-chord location)

(b) $L5$ (a downstream location)

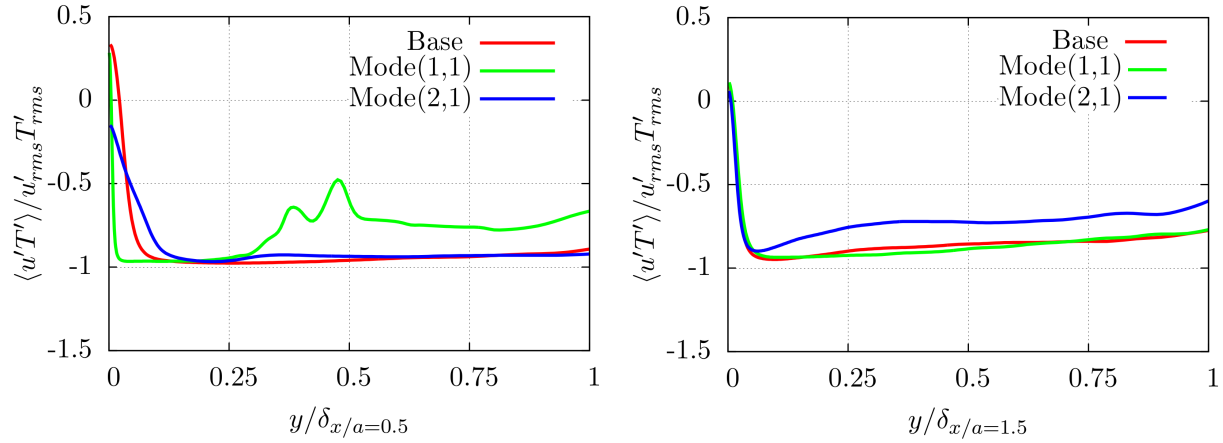

(c) $L3$ (panel mid-chord location)

(d) $L5$ (a downstream location)

Figure 27: Applicability of the strong Reynolds analogy for the three cases. (a) Eq. 22 at $x/a = 0.5$ (b) Eq. 22 at $x/a = 1.5$ (c) Eq. 23 at $x/a = 0.5$ (d) Eq. 23 at $x/a = 1.5$

the boundary layer for both Mode(1,1) and Mode(2,1) returns to the Base case profile, confirming the SRA in most of the boundary layer (Fig. 27 b).

Similarly the second SRA relation, Eq. 23), is evaluated for the three cases. The normalized thermal shear stress, $\langle u'T'\rangle/u'_{rms}T'_{rms}$, for increasing wall normal distance is displayed in Fig. 27(c) and Fig. 27(d) for location $L3$ and $L5$ respectively. As anticipated, the anti-correlation between the velocity and thermal fluctuations is evident for all the three cases at the panel mid-chord and downstream locations. The correlation profile for Mode(1,1) (Fig. 27 c) at the upstream location $L3$ exhibits higher values (or lower negative values) as high as -0.5 for the wall distance in $0.25 \lessapprox y/\delta_{x/a=0.5} \lessapprox 1$ compared to the Base case and Mode(2,1). The anti-correlations between the velocity and temperature, for all cases, drop sharply to near-zero values in the near-wall region ($y/\delta_x \lessapprox 0.1$), as shown in Fig. 27(c) and Fig. 27(d).

6.1.3 Effects on turbulence structure

We now examine the effect of surface deformation on the evolution of coherent structures. Their descriptions, including jet- and wake-like structures [77] or near-wall streamwise streaks [78] may be characterized by different length scales. The turbulent eddies from the outer region of the boundary layer influence the near wall streaks, whose imprints on the wall may be examined in terms of the coherent wall pressure fluctuations. The effect of compressibility on these structures is significant; for example, the streaks are known to be relatively smaller in size compared to their incompressible counterparts [79].

The two-point cross-correlation is typically employed to extract turbulent scales of interest:

$$\langle \phi'_L \psi' \rangle = \frac{\langle \phi'(\vec{x}_L)\psi'(\vec{x}_L + \vec{\Delta x})\rangle}{\phi_\infty \psi_\infty}, \tag{24}$$

where ϕ' and ψ', are two representative variables, $\vec{x}_L$ is a specific chosen location in the flow (Table 3), $\vec{\Delta x}$ represents the separation between the two points and the normalization employs global reference values of the two variables. The two-point correlations between the turbulent wall-pressure and flow pressure for locations $L3$ and $L4$ are displayed in Fig. 28 for the three cases. The correlation $\langle p'_{L3} p' \rangle / p^2_\infty$ in xz and xy planes on the flat surface (Base case) is displayed in Fig. 28(a) and Fig. 28(b) respectively, while its evolution at the downstream location $L4$ is displayed in xy plane in Fig. 24(c). The turbulent wall pressure p'_{L3} exhibits positive correlation with the surrounding turbulent wall pressure; in addition, it displays two lobes of negative correlation, one upstream and another downstream of the positive lobe, along the flow direction as shown in Fig. 24(a). The streamwise and spanwise extents of the correlation are $\approx 0.15a$ ($\approx 4.06\delta_{x/a=0.5}$) and $\approx 0.075a$ ($\approx 2.03\delta_{x/a=0.5}$) respectively, whereas in the wall normal direction (Fig. 24b) the correlation extends up to $\approx 0.04a$ ($\approx 1.08\delta_{x/a=0.5}$) from the wall, leading to three-dimensional cones of the positive and negative correlations. The approximate base diameters for the positive and negative cones of the pressure correlations are $0.075a$ ($\approx 2.03\delta_{x/a=0.5}$) and $0.0167a$ ($\approx 0.45\delta_{x/a=0.5}$) respectively. The size of the correlation, $\langle p'_{L4} p' \rangle / p^2_\infty$, in the wall normal direction at the downstream location $L4$ increases to $0.05a$ ($\approx 1.24\delta_{x/a=1.0}$). This increase of about $\approx 25\%$ occurs for the complete 3-D correlation, when compared to $\approx 10\%$ increase of the the boundary layer thickness from location $L3$ to location $L4$. These correlations are integrally connected with various near wall dynamics on length-scales and flow structure orientations as discussed by [80–82] for incompressible turbulent boundary layers.

The boundary layer undergoes modifications due to the presence of surface deformations, as discussed in Sec. 6.1.1; in the same vein, the two-point turbulent pressure correlations are also modified. The effects of surface deflection on the correlations at locations $L3$ and $L4$ for Mode(1,1) and Mode(2,1) are displayed in Figs. 28(d),(e),(f) and Figs. 24(g),(h),(i) respectively. For Mode(1,1), the turbulent pressure correlation $\langle p'_{L3} p' \rangle / p^2_\infty$ at $L3$ (Fig. 28d) is, relatively, weak compared to the Base case (Fig. 28a); whereas its dimensions and shape appear nearly the same, in the absolute sense. However, the boundary layer height at this location $\delta_{x/a=1.0}$ decreases by $\approx 66\%$ compared to the Base case. At the downstream location $L4$, the size of the conical pressure correlation increases by $\approx 10\%$, making an inclination of $\approx 20\,\mathrm{deg}$ to the wall normal, as shown in Fig. 28(f)*; while the boundary layer height at this location becomes $\approx 98.5\%$ of that in the Base case.

For Mode(2,1) surface deflection, the two-point pressure correlations (Eq. 24) at the two locations $L3$ and $L4$

*The axes of Fig. 28 use different scales for better comparison among the three cases.

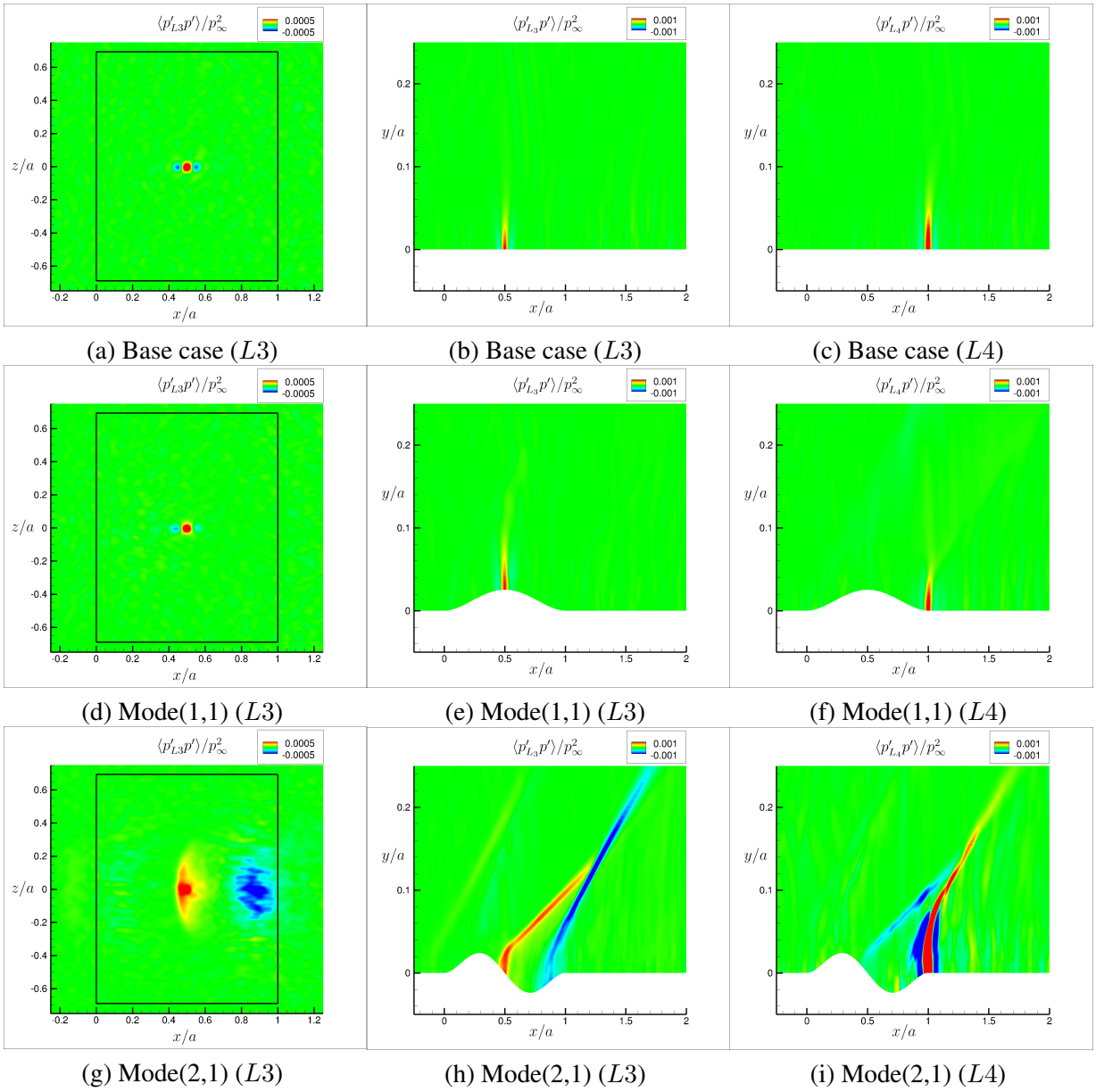

(a) Base case ($L3$) (b) Base case ($L3$) (c) Base case ($L4$)

(d) Mode(1,1) ($L3$) (e) Mode(1,1) ($L3$) (f) Mode(1,1) ($L4$)

(g) Mode(2,1) ($L3$) (h) Mode(2,1) ($L3$) (i) Mode(2,1) ($L4$)

Figure 28: Two-point turbulent pressure correlations at $L3$ (panel mid-chord) and $L4$ (panel trailing edge) locations (Table 3) for the flat and deflected surfaces.

are significantly modified compared to the Base case, as shown in Figs. 28(g),(h) and (i). Unlike Mode(1,1), the location $L3$ for Mode(2,1) lies in the separation region (Fig. 23 c, $x/a = 0.5$), in the mean sense; thus the wall pressure fluctuations exhibit a much larger extent of the correlation compared to the Base case and Mode(1,1), which is in agreement with the observations of [82]. Furthermore, the separation region of Mode(2,1) is accompanied by the presence of a set of expansion and compression waves that emanate near the locations $L3$ and $L4$ respectively, which results in bridging the turbulent flow structures at the two locations. Consequently, the turbulent wall pressure at location $L3$ manifests a strong correlation with the pressure fluctuations near location $L4$, albeit an anti-correlation. The positive correlation near

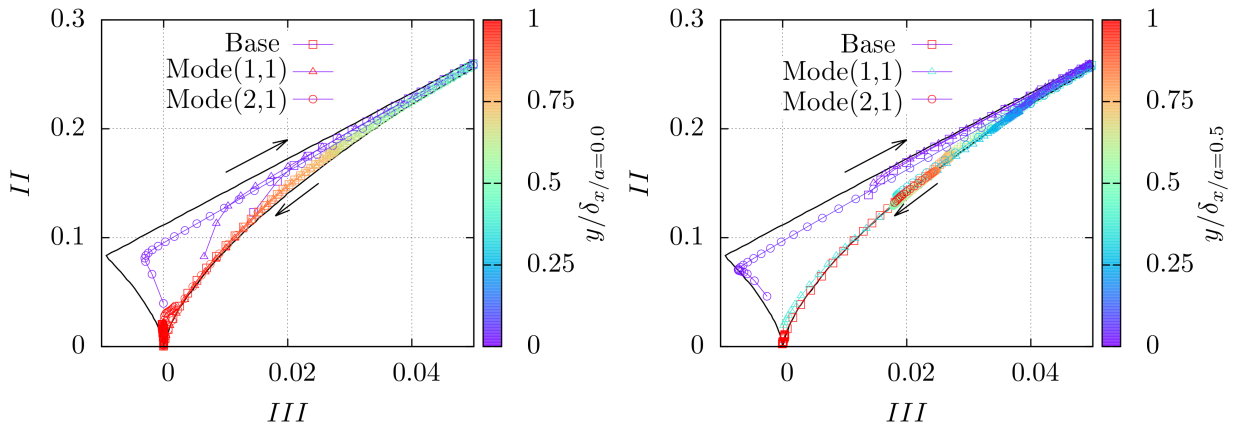

(a) $L2$ (panel leading edge location) (b) $L3$ (panel mid-chord location)

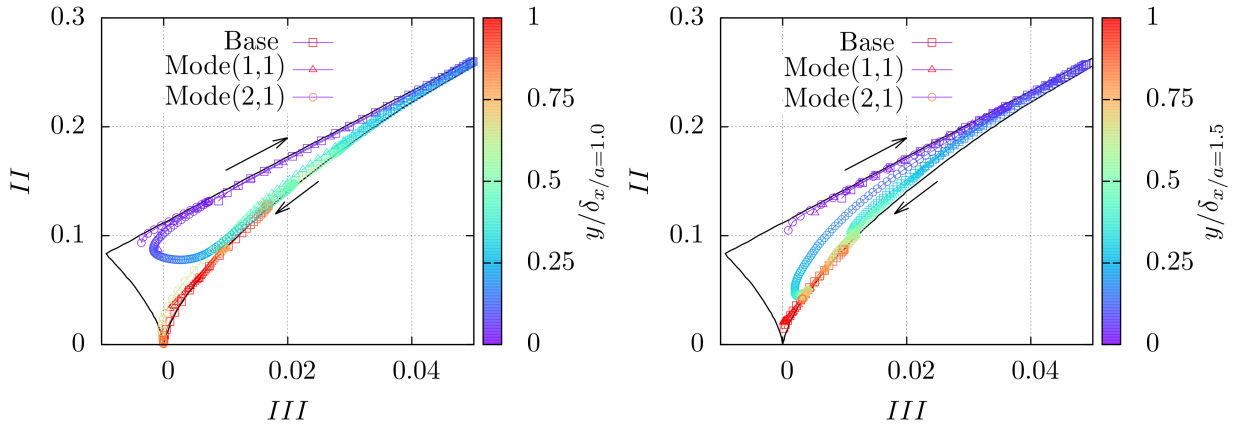

(c) $L4$ (panel trailing-edge location) (d) $L5$ (a downstream location)

Figure 29: Turbulence anisotropy map for Base case, Mode(1,1) and Mode(2,1) at different streamwise locations. The black curves delineate Lumley's triangle.

location $L3$ spans over $\approx 0.15a$ ($\approx 3.34\delta_{x/a=0.5}$) and $\approx 0.4a$ ($\approx 8.9\delta_{x/a=0.5}$) in the streamwise and spanwise directions respectively (Fig. 28g). In addition, an equally strong negative correlation manifests at a downstream location of $x/a = 0.85$, spanning over $\approx 0.2a$ ($\approx 4.46\delta_{x/a=0.5}$) and $\approx 0.4a$ ($\approx 8.9\delta_{x/a=0.5}$) in the streamwise and spanwise directions respectively (Fig. 28g). Interestingly, the pressure correlation at $L3$ escalates due to expansion and compression waves and extends into the far field, engaging the large scales of turbulence (Fig. 28h). Similarly, the turbulent wall pressure at $L4$ exhibits an anti-correlation with location $L3$, stretching the correlation into the far field, as shown in Fig. 24(i).

The effect of surface deformation on the structure of turbulence is estimated with Lumley's traceless and symmetric tensor that identifies deviation from isotropic turbulence[83]:

$$a_{ij} = \frac{\langle u_i' u_j' \rangle}{2\mathcal{K}} - \frac{\delta_{ij}}{3}, \tag{25}$$

where $\mathcal{K} = \langle u_i' u_i' \rangle / 2$ is the turbulent kinetic energy and δ_{ij} is the Kronecker delta. For reference, the second

and third scalar invariants that aid in the deviation assessments are [84]:

$$II = a_{ij}a_{ji} = \frac{1}{2}a_{ii}^2 \quad \text{and} \quad III = a_{ij}a_{jk}a_{ki} = \frac{1}{3}a_{ii}^3 \tag{26}$$

respectively, since variant I is zero. The invariant-map, plotted as III versus II map, manifests a triangular shape (Lumley's triangle), which includes all physically realizable states of turbulence inside the triangle.

The turbulence anisotropy invariant-maps for the three cases (Base case, Mode(1,1) and Mode(2,1)) at four streamwise locations, namely $L2$, $L3$, $L4$, and $L5$ (refer Table 3), are displayed in Figs. 29(a),(b),(c), and (d), respectively, where the black curves delineate Lumley's triangle. In each sub-figure (of Fig. 29), the invariants of the anisotropy tensor are estimated along the wall normal direction for the three cases. The curves for the Base case, Mode(1,1) and Mode(2,1) are shown using square, triangle and circle symbols respectively, colored using the wall normal distance normalized by the local boundary layer thickness. The arrows indicate the direction of increasing wall normal distance. In general, the curves begin (near wall) in the left corner of the triangle. In this region, the streamwise and spanwise components are similar (two-component limit), and are much larger than the wall-normal velocity fluctuation component. As the wall normal distance increases, invariants II and III increase together in somewhat linear fashion and the curve forms the upper corner; this is the one-component limit where one component (here, the streamwise component) is much larger than the other two components. With further distance from the surface, both III and II decrease to finally yield the three-component limit or the isotropic turbulence at the bottom corner of the triangle, where the II and III invariants become zero.

The near-wall turbulence at the panel leading edge (location $L2$) for Mode(1,1) and Mode(2,1) differs from the Base case in terms of the starting (near-wall) values of the invariants, initiating at points far from the two-components limit, as displayed in Fig. 29(a). The onset/presence of flow separation at location $L2$ appears to have influenced the near-wall turbulence structure for Mode(1,1) and Mode(2,1). However, the one-component limit for the three cases is reached at about $y \approx 0.25\delta_{x/a=0.0}$, in addition to the similar behavior for $y/\delta_{x/a=0.0} \gtrapprox 0.25$ (Fig. 29a). At location $L3$, the anisotropy invariant-curves for the Base case and Mode(1,1) follow the two-components limit and one-component limit, eventually reaching the isotropy limit (Fig. 29 b). In contrast, the near-wall turbulence state for Mode(2,1) indicates the influence of the flow separation at this location ($L3$), without reaching the isotropy limit at $y/\delta_{x/a=1.0} = 1$, where the flow field undergoes an expansion. The similarities and differences of the state of turbulence at this location ($L3$) among the three cases are consistent with the two-point turbulent pressure correlations discussed before. The turbulent anisotropy state at the panel trailing edge (location $L4$) manifests similar behavior for the Base case and Mode(1,1), where the curves follow the typical anisotropy limits; however, the invariant-curve for Mode(2,1) exhibits a jump from the two-components limit in the near wall region to the axisymmetric turbulence expansion path to isotropic turbulence, as displayed in Fig. 29(c). The anisotropy invariant-curves at the downstream location $L5$ for the three cases are shown in Fig. 29(d), where the boundary layer turbulence for Mode(1,1), to large extent, returns to the relaxed state close to the Base line, whereas Mode(2,1) turbulence anisotropy profiles exhibit some deviation, particularly in the outer boundary layer region.

6.1.4 Flow unsteadiness and turbulence spectra

The surface deformations in Mode(1,1) and Mode(2,1) locally modify the supersonic TBL in terms of the flow properties and turbulence structure, in the time-mean sense, where, as noted before, the modified boundary layer returns to an equilibrium state at about $0.5a$ ($20\delta_{in}$) downstream of the panel trailing edge.

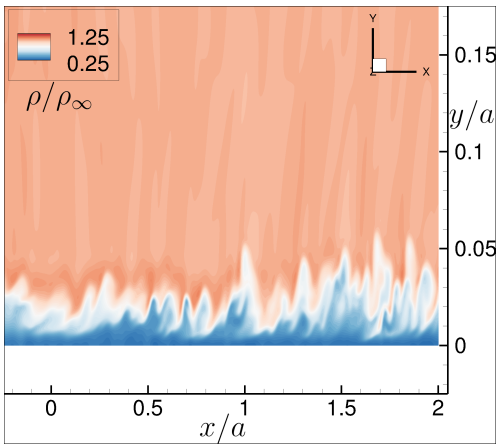

(a) Base case

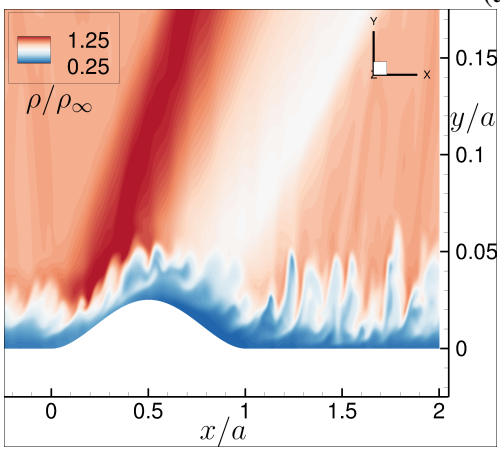

(b) Mode(1,1)

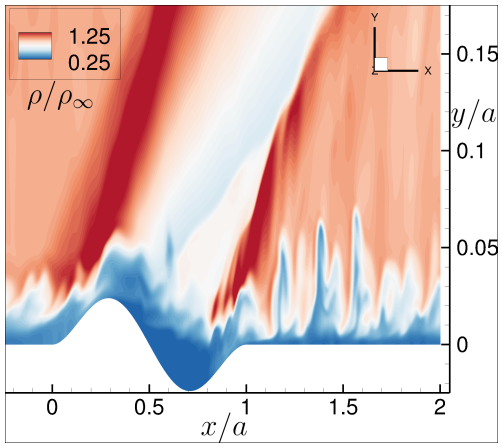

(c) Mode(2,1)

Figure 30: Normalized density at the mid-span ($z = 0$) plane for the three cases. (a) flat surface Base case (b) Mode(1,1) surface deformation (c) Mode(2,1) surface deformation.

However, the surface deformations in some regions introduce a strong adverse pressure gradient, leading to flow separation. For example, the flow near the panel leading edge (location $L2$) for Mode(1,1) and Mode(2,1) as well as near the mid-chord length (location $L3$) separates, transiently but not in the mean sense for the former, due to the adverse pressure gradients, as discussed before in terms of the skin-friction coefficient (Fig. 23c). The regions exhibiting the flow compression and expansion due the surface deformations of Mode(1,1) and Mode(2,1) alongside the Base flow are displayed in Fig. 30, where the density increase due to the compression and decrease due to the expansion are evident. The figure also manifests the increased levels of flow turbulence downstream of the surface deformations for both Mode(1,1) (Fig. 30b) and Mode(2,1) (Fig. 30c) compared to the flat Base case (Fig. 30a), which is consistent with the higher Reynolds stresses in Fig. 25 for the two cases (Mode(1,1), Mode(2,1)).

The turbulence modification in the near wall region due to the surface deformations and flow separation is also analyzed by using the power spectral densities (PSD) of the streamwise velocity and wall pressure. The spectra are computed as a function of the spanwise wavenumber ($\omega_z = 2\pi/\lambda_z$, where λ_z is the wavelength) at the leading ($L2$) and trailing ($L4$) edge locations of the panel, while the streamwise velocity spectra are

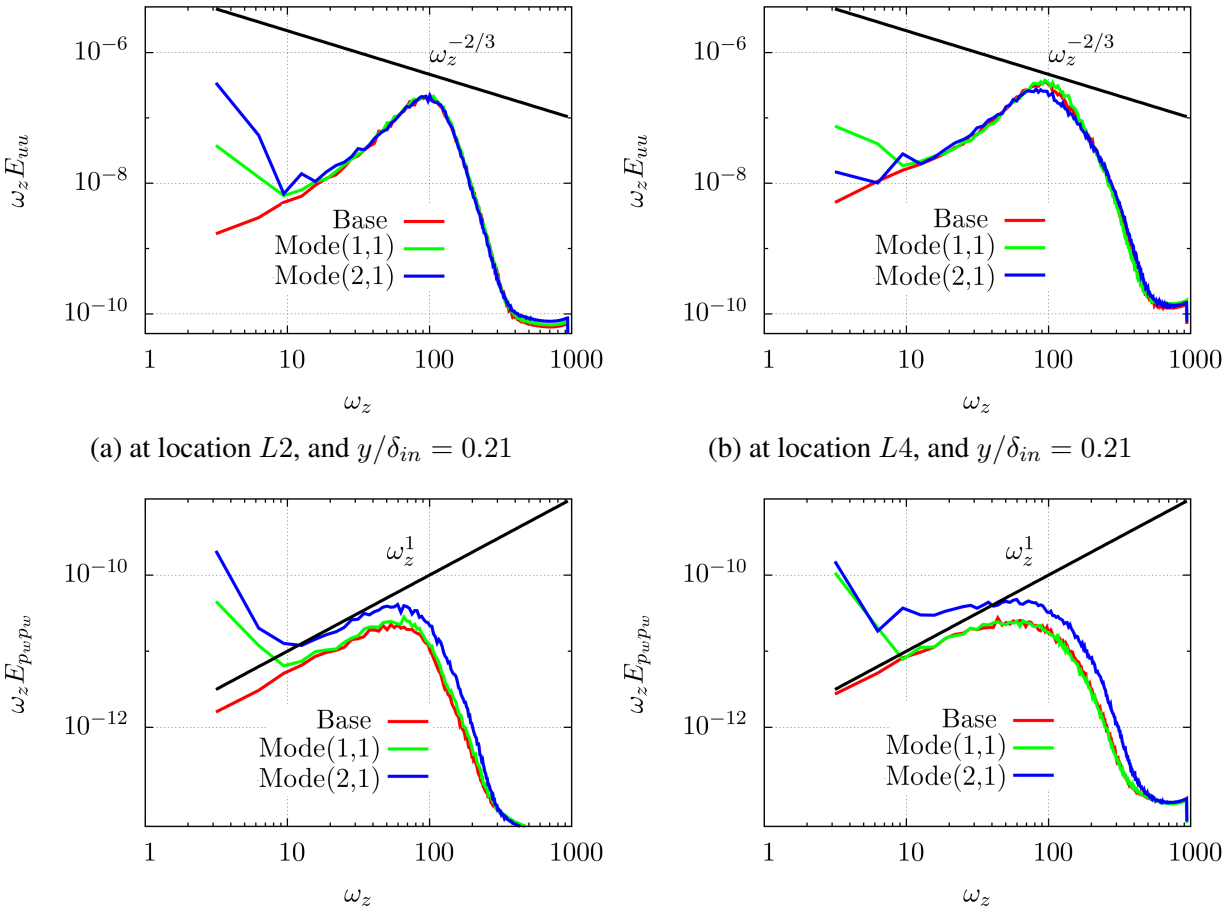

(a) at location $L2$, and $y/\delta_{in} = 0.21$

(b) at location $L4$, and $y/\delta_{in} = 0.21$

(c) at location $L2$, and $y/\delta_{in} = 0.0$

(d) at location $L4$, and $y/\delta_{in} = 0.0$

Figure 31: Turbulence spectra of the streamwise velocity and wall pressure versus the spanwise wavenumber for the three cases. (a) Streamwise velocity spectra at the panel leading edge and $y/\delta_{in} = 0.21$ (b) streamwise velocity spectra at the panel trailing edge and $y/\delta_{in} = 0.21$ (c) wall pressure spectra at the panel leading edge and $y/\delta_{in} = 0.0$ (c) wall pressure spectra at the panel trailing edge and $y/\delta_{in} = 0.0$.

computed at a wall normal distance of $\approx 0.21\delta_{in}$. The pre-multiplied spectra of the streamwise velocity (E_{uu}) as a function of the spanwise wavenumber (ω_z) for the three cases at the panel leading edge location $L2$ are shown in Fig. 31(a); while the evolution of spectra at the downstream location $L4$ is displayed in Fig. 31(b). The wavenumber and PSD are normalized by using the panel length (a) and free-stream pressure p_∞, respectively. Overall, the spectral energy at the downstream location $L4$ is higher for all wavenumbers, where both (the upstream $L2$ and downstream $L4$) spectra exhibit a short production range ($E_{uu} \propto \omega_z^{-1}$) that is centered around $\omega_z \approx 100$. This wavenumber corresponds to a spanwise wavelength scale of $\lambda_z \approx 0.063a$ ($\lambda_z = 2.5\delta_{in}$). Furthermore, the streamwise velocity spectra exhibit a very short inertial sub-range of turbulence at the both locations, as indicated by the solid black line with $\omega_z E_{uu} \propto \omega_z^{-2/3}$ (*i.e.* $E_{uu} \propto \omega_z^{-5/3}$). As opposed to the velocity spectra for Base case, the magnitudes of PSD for Mode(1,1) and Mode(2,1) are higher at the lower wavenumbers, as shown in Figs. 31(a) and (b), which correspond to the flow three-dimensionality induced by the surface deformations.

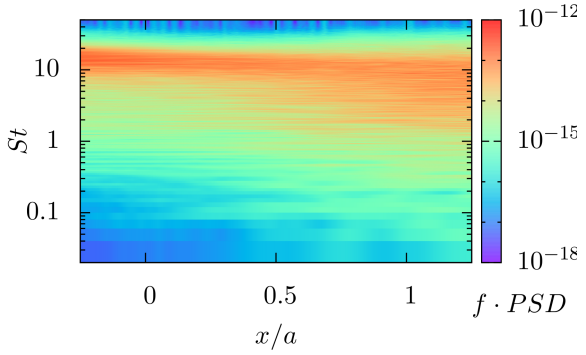

(a) Base case

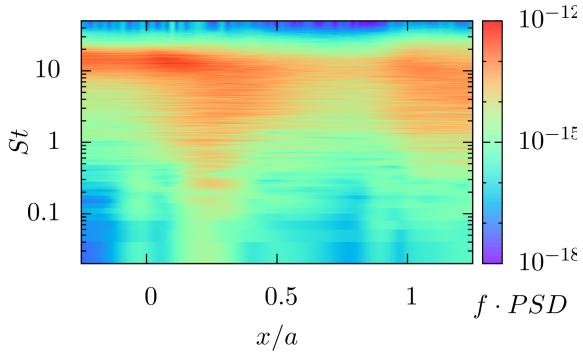

(b) Mode(1,1)

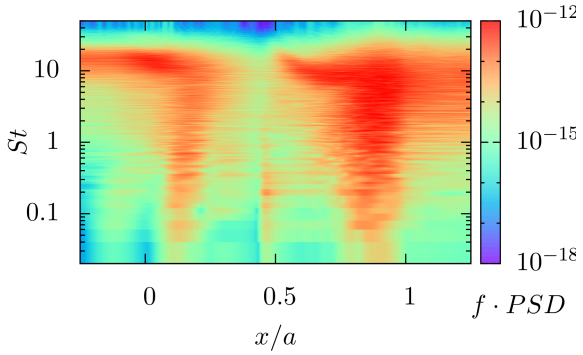

(c) Mode(2,1)

Figure 32: Pre-multiplied power spectral density of the wall pressure at $z = 0$

A flat region of a pre-multiplied spectrum of the wall pressure represents the ω_z^{-1} dependence of the wall pressure PSD on the wavenumber/frequency. In this range of wavenumbers, the pressure contribution is mainly due to the large eddies from the log-layer [85], which corresponds to the mid-range wavenumbers/frequencies of the pressure spectra (Figs. 31c and d). The magnitudes of wall pressure PSD at downstream location $L4$ are, to some degree, higher compared to upstream location $L2$ for all wavenumbers, as shown in Figs. 31(c) and (d). Additionally, the flat range of the pre-multiplied spectrum ($\omega_z E_{p_w p_w} \propto \omega_z^0$, Fig. 31c) at $L2$ is increased at the downstream location $L4$ (Fig. 31d). At the lower wavenumbers however, the wall pressure spectra do not exhibit ω_z^2 power law, or equivalently ω_z^3 for the pre-multiplied spectra, as shown in Figs. 31(c) and (d); rather that manifest no dependence on the wavenumber, *i.e.* $E_{p_w p_w} \propto \omega_z^0$ (or $\omega_z E_{p_w p_w} \propto \omega_z^1$), agreeing with the experimental observation of [86]. Similar to the streamwise velocity spectra, the wall pressure spectra for Mode(1,1) and Mode(2,1) exhibit higher spectral energy for the lower wavenumbers at both locations $L2$ and $L4$ (Fig. 31c and d) when compared to the flat surface Base case spectra.

In addition to the increased level of turbulence, the flow separation associated with the shock wave boundary layer interaction (SWBLI) introduces a characteristic low-frequency unsteadiness [10, 87, 88]. The low

frequencies are 1 to 2 orders of magnitude lower compared to the turbulence frequencies, whose potential origin mechanisms have been discussed in [89]. The pre-multiplied wall pressure PSD of the temporal data along the center-line ($z = 0$) for the three cases are displayed in Fig. 32. As opposed to the Base case wall pressure PSD (Fig. 32a), the wall pressure spectra for Mode(1,1) (Fig. 32 b) and Mode(2,1) (Fig. 32 c) clearly manifest the presence of low-frequency unsteadiness, prominently in the regions where the flow undergoes separation, that is, in the proximity of location $L2$ ($x/a \approx 0.0$) for Mode(1,1) and locations $L2$ and $L4$ ($x/a \approx 1.0$) for Mode(2,1). The frequencies are normalized by using the panel length (a) and free-stream velocity (u_∞), leading to Strouhal numbers ($St = fu_\infty/a$) of the order of those observed in SBLI (as low as 0.02), particularly for Mode(1,1) and Mode(2,1). Furthermore, the magnitudes of wall pressure spectra increase due to the surface deformations (Fig. 32) for almost all Strouhal numbers ($0.02 \leq St \lessapprox 40$), indicating an increased level of flow turbulence in addition to the low frequency dynamics.

6.1.5 Summary

We have examined the effects of surface modal deformations on a spatially evolving supersonic turbulent boundary layer. Although the surface deformations manifest minimal thermal and compressibility effects on the flow in terms of the Morkovin's hypothesis and strong Reynolds analogy, they result in local modification of the turbulence structure as well as, in general, amplification of the flow turbulence. The adverse pressure gradients induced by the surface deformations cause flow separation, giving rise to the low frequency dynamics associated with the shock wave boundary layer interaction. For the parameters considered, the surface deflection associated with Mode(2,1) impacts the TBL far more than that associated with Mode(1,1); this is mainly due to the higher degree of flow separation induced by the Mode(2,1) surface deflection. Thus from the fluid-thermal-structural-interaction (FTSI) point of view, an initial static surface deformation caused by, for instance, thermal loading at high-speeds can lead to the low-frequency flow dynamics (pressure loading); which can eventually result in a coupled fluid-structure interaction (FSI) and in turn a full FTSI.

6.2 Impact of Structurally Induced Flow Separation on Loads Prediction

Structural state-of-the-art design requires simple and quick calculations to determine turbulent pressure loads for structural responses. The semi-empirical model used here to predict the RMS surface pressure follows the implementation described in [22]. The semi-empirical relationships for this approach were developed in [1, 17, 37] for incompressible attached TBL flow and were extended to compressible flow using a transformation function. The model is used to compute RMS pressure levels and PSDs for use in structural responses. A theoretical turbulent boundary layer height was matched at the start of the panel, and boundary layer edge quantities were used to compute RMS pressure. Attached flow was assumed for the semi-empirical model.

RMS values for the LES pressure predictions discussed in Section 6.1 are compared to the semi-empirical model[1, 17, 37], denoted here as "Laganelli & Wolfe". These are shown in Fig. 33. Note three different curves are displayed for the LES results: RMS for the pressure at the spatial discretization of the surface mesh and RMS for the pressure spatially averaged for length scales that correspond to a Kulite pressure sensor. The latter is important, since spatial averaging inherently reduces RMS pressure. While the size of Kulite used for development of the semi-empirical Laganelli & Wolfe model, the 0.1" spatially averaged LES prediction provides good agreement with the semi-empirical model. Good agreement with the Laganelli / Wolfe model is expected, since the semi-empirical model was taken from data measured for a TBL over a flat plate. However, the agreement diminishes considerably for a TBL over Mode (1,1) and Mode (2,1) deformations. In particular, the Mode (1,1) deformation has the same shape of RMS pressure, but is

substantially scaled compared to the semi-empirical model. Furthermore, for Mode (2,1), where there are regions of local flow separation, both the shape and magnitude of the RMS pressure deviate substantially. This is significant since the structural response can be sensitive to both the magnitude and spatial variation of the RMS pressure [22, 24, 25]. This clearly becomes significantly challenging when local flow separation occurs.

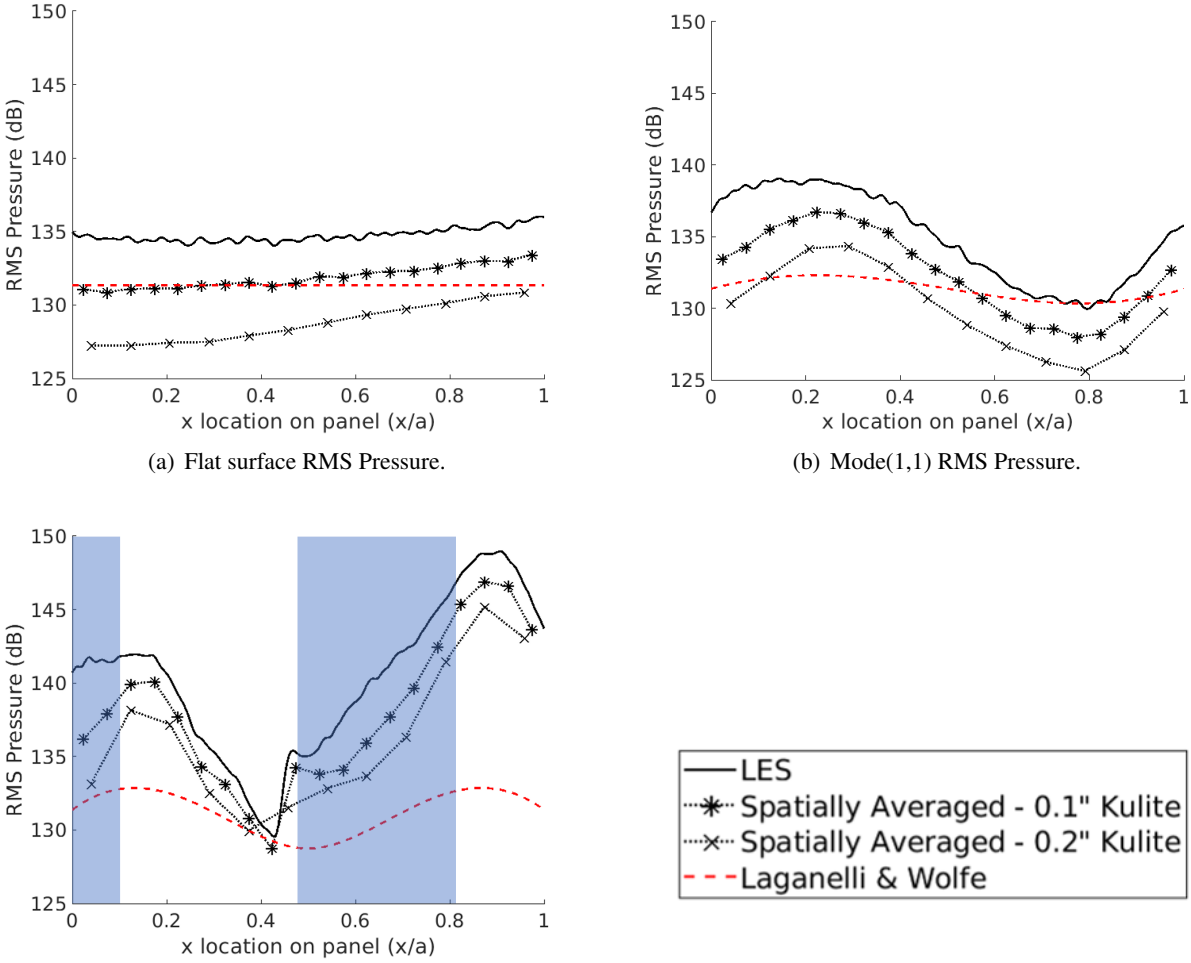

(a) Flat surface RMS Pressure.

(b) Mode(1,1) RMS Pressure.

(c) Mode(2,1) RMS Pressure.

Figure 33: RMS pressure prediction comparisons between LES (Section 6.1) and the Laganeilli & Wolfe semi-empirical model. Shaded Regions Denote Separated Flow.

6.3 Momentum Integral Equation Analysis Considering Static Deformations

The results discussed to this point indicate that structurally induced flow separation leads to substantially increased importance and complexity of understanding interactions between the boundary layer dynamics and surface response. This section summarizes indepth analysis of the Momentum Integral Equation when considering structural deformation, which provides fundamental insights into the specific structural parameters that drive onset of separation to occur. Full details of the mathematical analysis are available in:

Becks, A. Linking Static Structural Surface Topology Changes to Supersonic Turbulent Boundary Layer

Flow Separation. MS Thesis. The Ohio State University. Spring 2022 (expected).

Consider the conservation of mass and momentum equations for a boundary layer system in 2D Cartesian coordinates:

$$\frac{\partial \rho}{\partial t} + \frac{\partial \rho u}{\partial x} + \frac{\partial \rho v}{\partial y} = 0 \tag{27}$$

$$\rho \frac{\partial u}{\partial t} + \rho u \frac{\partial u}{\partial x} + \rho v \frac{\partial u}{\partial y} = \rho g_x - \frac{\partial p}{\partial x} + \frac{\partial}{\partial x}\left[2\mu \frac{\partial u}{\partial x} + \lambda\left(\frac{\partial u}{\partial x} + \frac{\partial v}{\partial y}\right)\right] + \frac{\partial}{\partial y}\left[\mu\left(\frac{\partial u}{\partial y} + \frac{\partial v}{\partial x}\right)\right] \tag{28}$$

This work follows closely to that by [90] and [91]. The Momentum Integral Equation (MIE), Eq. 29, is derived from Eq. 28 through invoking a series of assumptions. First, we invoke Stokes' hypothesis, $\lambda = -\frac{2}{3}\mu$ [92], as well as neglect any body forces, such as gravity or magnetic forces, $g_x = 0$. We also will assume that viscosity is not a function of time or space, $\mu \neq f(x, y, t)$. We now integrate the momentum equation along a line, from the wall, δv to an arbitrary height h:

$$\int_{\delta v}^{h} \rho \frac{\partial u}{\partial t} dy + \int_{\delta v}^{h} \rho u \frac{\partial u}{\partial x} dy + \int_{\delta v}^{h} \rho v \frac{\partial u}{\partial y} dy = \int_{\delta v}^{h} -\frac{\partial p}{\partial x} dy + \int_{\delta v}^{h} \frac{4}{3}\mu \frac{\partial^2 u}{\partial x^2} dy + \int_{\delta v}^{h} \frac{1}{3}\mu \frac{\partial^2 v}{\partial x \partial y} dy + \int_{\delta v}^{h} \mu \frac{\partial^2 u}{\partial y^2} dy \tag{29}$$

Next several simplifications are assumed:

- The arbitrary height h is allowed to approach ∞ allowing the use of freestream quantities.
- Viscous forces are negligible in the freestream.
- Gradients in the freestream are assumed negligible.
- The flow is in a converged, steady state, and time-averaged quantities are analyzed.
- The integral of the second derivative of streamwise velocity is negligible.

These with further mathematical manipulations lead to the following form of the MIE, Eq. 30:

$$-\frac{1}{3}\mu \left.\frac{\partial v}{\partial x}\right|_{\delta v} - \mu \left.\frac{\partial u}{\partial y}\right|_{\delta v} = -\delta_p \frac{\partial p_\infty}{\partial x} + \delta_1 \frac{\partial p_\infty}{\partial x} - p_\infty \frac{\partial \delta_p}{\partial x} - (p_\infty - p_{\delta v}) \frac{\partial \delta v}{\partial x} - \rho_\infty u_\infty^2 \frac{\partial \delta_2}{\partial x} \tag{30}$$

The LHS of Eq. 30 is proportional to the skin friction coefficient, C_f, and thus represents the condition for flow separation to occur. The RHS are all terms dependent on surface deformation. To further establish this link, we assume using Linear Piston Theory [93], in Eqs. 31 and 32 that $p_{\delta_v} \sim \frac{\partial \delta_v}{\partial x}$, and $\frac{\partial p_{\delta_v}}{\partial x} \sim \frac{\partial^2 \delta_v}{\partial x^2}$.

$$p_{\delta v} = p_\infty + \gamma p_\infty M_\infty \left(\frac{\partial \delta v}{\partial x} + \frac{1}{u_\infty}\frac{\partial \delta v}{\partial t}\right) \tag{31}$$

$$\frac{\partial p_{\delta v}}{\partial x} = \gamma p_\infty M_\infty \left(\frac{\partial^2 \delta v}{\partial x^2} + \frac{1}{u_\infty}\frac{\partial^2 \delta v}{\partial x \partial t}\right) \tag{32}$$

Propagating this into Eq. 30 yields:

$$-\frac{1}{3}\mu \left.\frac{\partial v}{\partial x}\right|_{\delta v} - \mu \left.\frac{\partial u}{\partial y}\right|_{\delta v} \sim f\left(\delta_v, \frac{\partial \delta_v}{\partial x}, \left(\frac{\partial \delta_v}{\partial x}\right)^2, \frac{\partial^2 \delta_v}{\partial x^2}\right) \tag{33}$$

And since the LHS of Eq. 33 is proportional to C_f, we can also say that:

$$C_f \sim f\left(\delta_v, \frac{\partial \delta_v}{\partial x}, \left(\frac{\partial \delta_v}{\partial x}\right)^2, \frac{\partial^2 \delta_v}{\partial x^2}\right) \tag{34}$$

This result in Eq. 34 indicates that skin friction on a surface with deformation is a function of the deformation, the first streamwise spatial derivative of deformation, and the second streamwise spatial derivative of deformation.

Further analytical understanding is not possible without substantial simplifying assumptions that severely limit generality of any gained understanding. Thus, a data-driven approach was undertaken using the model generating software, Eureqa®, along with the LES simulations to provide deeper insights into the link between surface deformation and flow separation. Here, following work by Brouwer et al. [91] , who established insights on changes in shock-induced separation with surface surface deformation, the focus was on surface curvture in particular. This term was important in Brouwer et al. [91] since streamwise pressure changes are induced by the slope of surface deformation; thus, streamwise pressure gradients are induced by the second streamwise spatial derivative of surface deformation. However, a generalized form of curvature [94] was chosen for results discussed here, as shown in Eq. 35:

$$\kappa = \frac{\frac{\partial^2 \delta_v}{\partial x^2}}{\left[1 + \left(\frac{\partial \delta_v}{\partial x}\right)^2\right]^{3/2}} \tag{35}$$

Here, it is noted that surface curvature is dependent on both the first and second streamwise spatial derivative, and in particular the square of the first streamwise spatial derivative. This term indeed appeared in the proportionality shown in Eq. 34, and was consistently one of the dominant terms selected by Eureqa® along with the second streamwise spatial derivative.

The model selected for discussion here, based on balancing simplicity with accuracy and generality, is:

$$C_f = 3 \cdot 10^{-4} - 3.4 \cdot 10^{-4} \kappa \tag{36}$$

The above model can be implemented on the surface deformation in the previous LES dataset and compared to the computed skin friction, shown in 34.

Figure 35 demonstrates the strong negative correlation between the curvature of the surface and the skin friction. This only holds, however, prior to separation where the skin friction is positive. Once separation occurs, the assumptions used in the proportionality in Eq. 34 break down and requires if a link is desired/required. However, our primary focus is establishment of a generalizable threshold on structural deformation inducing flow separation, and these findings are an important initial step towards this goal. Future work is needed to establish remaining terms needed to fully collapse all lines onto a model that is independent of dataset and specific mode of structural deformation.

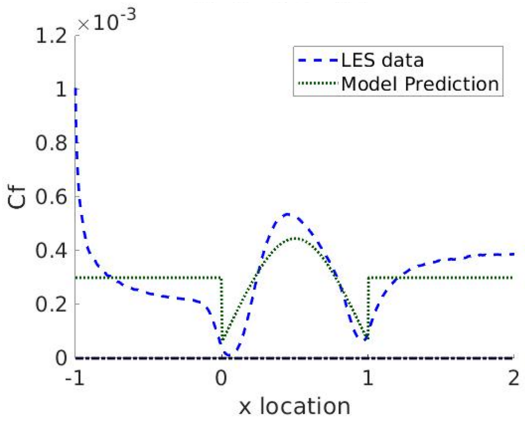

(a) Mode 1 LES data vs model prediction.

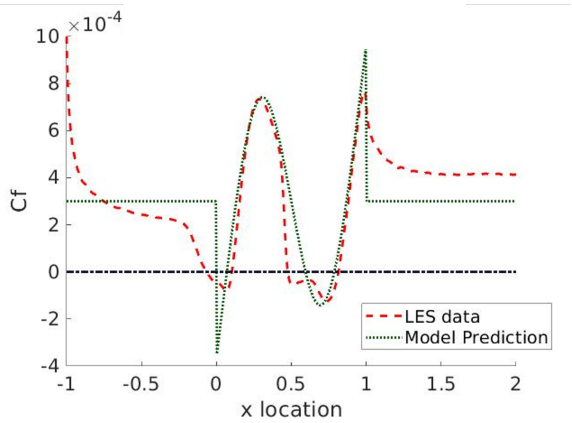

(b) Mode 2 LES data vs model prediction.

Figure 34: Curvature vs Skin friction Eureqa® model

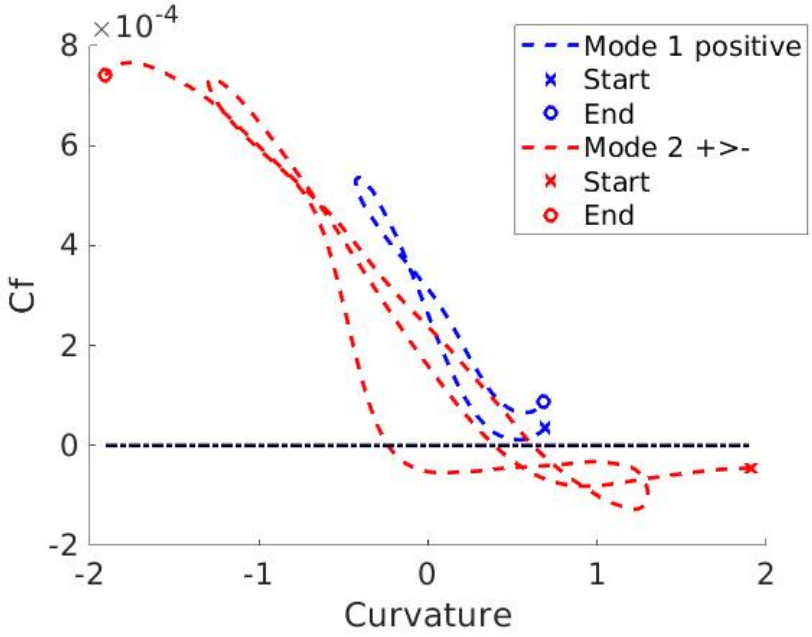

Figure 35: Skin friction vs curvature simulation results

6.4 Simulations of SBLI over Compliant Surfaces

High-speed fluid-structure interactions (FSI) between a supersonic turbulent boundary layer with an oblique shock wave and a skin panel are investigated by means of large eddy simulations (LES). We simulate the shock boundary layer interaction (SBLI) at Mach 4 and unit Reynolds number of 2.375×10^7 $(/m)$, where an oblique shock of strength $p_3/p_1 \approx 8.5$ and angle $\sigma \approx 30\,\mathrm{deg}$ impinges on a flexible panel near the mid-chord length. The fully clamped rectangular panel has the aspect ratio and non-dimensional panel thickness of $b/a = 1.377$ and $h/a = 0.003$, respectively. The strong SBLI induces a large flow separation of length $L_{sep} \approx 23\delta_{in}$ with a wide range of turbulent scales, including the characteristic low-frequency unsteadiness. Fluid and structural responses are compared across different classes of interaction, namely:

M_∞	Re $(/m)$	Re_a	P_0 (N/m^2)	T_0 (K)	p_∞ (N/m^2)	u_∞ (m/s)	ρ_∞ (kg/m^3)	δ_{in} (m)	δ_{in}/a (deg)	σ
4	2.468×10^7	1.63×10^6	5.40×10^5	297	3.983×10^3	674	0.17	2×10^{-3}	0.03	30

Table 4: Flow parameters

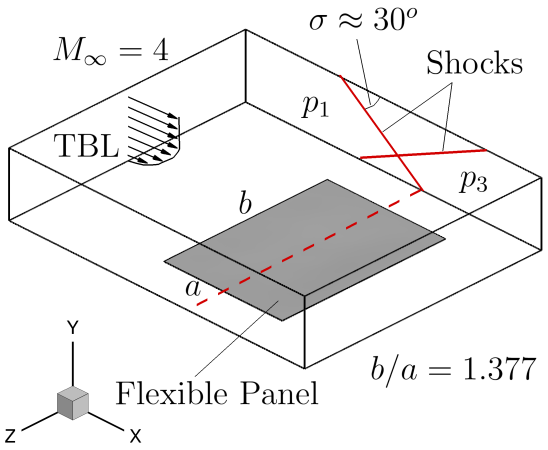

Figure 36: Computational geometry for LES of SBLI over flexible panel

rigid surface; one-way application of SBLI loads to the structure; and two-way interaction between the flow and structure. The interplay between the SBLI and flexible panel is elucidated using detailed analysis that includes proper orthogonal decomposition (POD), dynamic mode decomposition (DMD), and the recently developed Lagrangian Modal Analysis (LMA) for the deforming meshes [95]. The large panel deflections ($\sim 1h$) manifest into the structural non-linearity associated with the coupling between bending and stretching of the panel. Additional details of this component of the research are provided in Ref. [58] and will be further documented in a follow-up journal article that is currently in preparation. We highlight the results and conclusions of the study here.

The flow parameters are displayed in Table 4, where the choices of parameters are guided by the concurrent experiments at Caltech Ludwieg Tube discussed in Section 6.5. The inflow is at Mach 4 with a unit Reynolds number of 2.468×10^6 $(1/m)$, corresponding to a total pressure and temperature of $P_0 = 5.40 \times 10^5$ (N/m^3) and $T_0 = 297$ K, respectively. The inflow is well characterized in our recent paper [60], where the flow is at marginally lower Reynolds number and inflow boundary layer thickness as compared to the values in Table 4. The free-stream conditions, in terms of the velocity and density, and the panel insert dimensions are identical to those presented in Section 6.1 and in [60]. Thus, the present computational domain and grid resolution are based upon the domain extents and grid sensitivity study presented in [60].

The flexible panel on the bottom surface of the computation domain (Fig. 36) has an aspect ratio of $b/a = 1.3722$ and the normalized panel thickness of $h/a = 0.003$, where the rectangular panel extends from $(x = 0.0, z = -0.689)$ to $(x = 1.0, z = +0.689)$. The actual dimensions of the panel design are: length $a = 66 \times 10^{-3}$ m, width $b = 91 \times 10^{-3}$ m, and thickness $h = 0.2 \times 10^{-3}$ m. The panel is assumed to have properties of Stainless Steel, a material commonly used in aerospace applications. Table 5 provides material

Parameter	E_s	m_r	λ	ν	h/a	b/a	Nodes ($n_x \times n_z$)	Elements
Stainless Steel	$210 \times 10^9\ Pa$	0.00741	156	0.30	0.003	1.3771	81×101	16000

Table 5: Material properties of the compliant surface

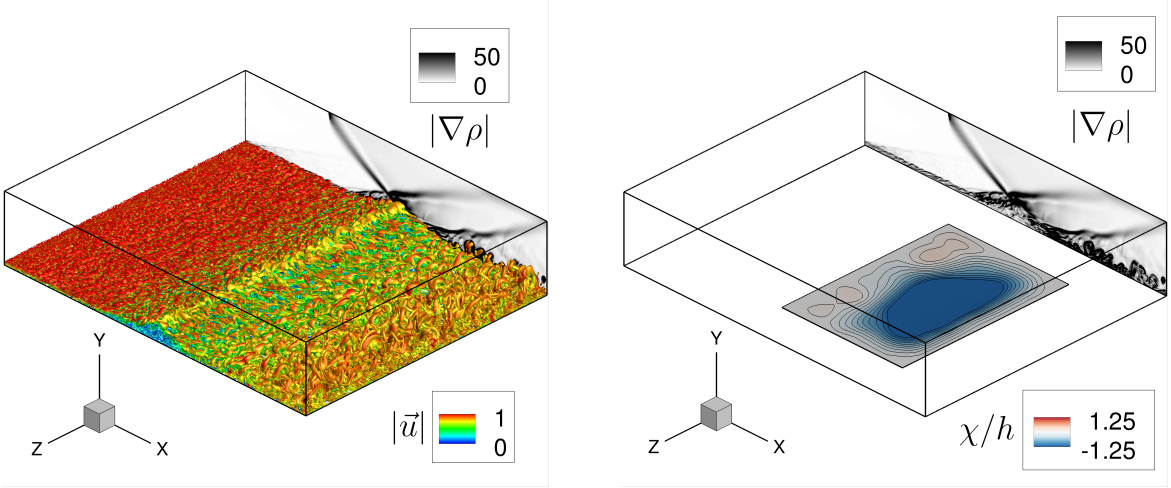

(a) (b)

Figure 37: Three-dimensional flow features of SBLI over flexible panel. (a) Q-criterion isosurface ($Q = 1$) colored with velocity magnitude and density gradient magnitude. (b) instantaneous panel deflection beneath SBLI.

properties of the panel, including the modulus of elasticity E_s and Poisson ratio ν, which are utilized in the definition of material flexural stiffness as $D = E_s h^3/12(1-\nu^2)$. A non-dimensional dynamic pressure (flutter parameter) is then given by $\lambda = \rho_\infty u_\infty^2 a^3/D$. The material density, $\rho_s = 7850\ kg/m^3$, is accounted for in terms of a non-dimensional mass ratio: $m_r = (\rho_\infty a)/(\rho_s h)$.

A full three-dimensional flow field in terms of Q-criterion isosurface is displayed in Fig. 37(a) for $Q = 1$ colored with the velocity magnitude; in addition, the figure shows the density gradient magnitude ($|\nabla\rho|$) on the side boundary, exhibiting the incident and reflected shocks associated with the turbulent boundary layer comprising the flow separation and turbulent flow features downstream the shock impingement. In addition, Fig. 37(b) displays an instantaneous position of the flexible panel interacting with the SBLI above, realizing the panel deflections of the order of the panel thickness ($\chi/h \approx 1.0$). Furthermore, the SBLI appears to intensify the turbulence in the interaction region, promoting large-scale turbulence structures downstream. The simulations are performed for a total time duration of $tu_\infty/a = 200$ with a time step of $\delta t u_\infty/a = 0.0001$. The statistics are gathered at a sampling rate of $100\delta t$ after an initial transient time of $tU_0/a = 100$, which approximately corresponds to a flow-through time of ≈ 40.

6.4.1 Flow separation and unsteadiness of SBLI

From the FSI viewpoint, the skin-friction coefficient and wall pressure are significant parameters manifesting the unsteady flow separation induced by the SBLI. The wall pressure profiles for the inviscid and viscous flows across the shock impingement over the rigid and flexible panels are displayed in Fig. 38(a), where the

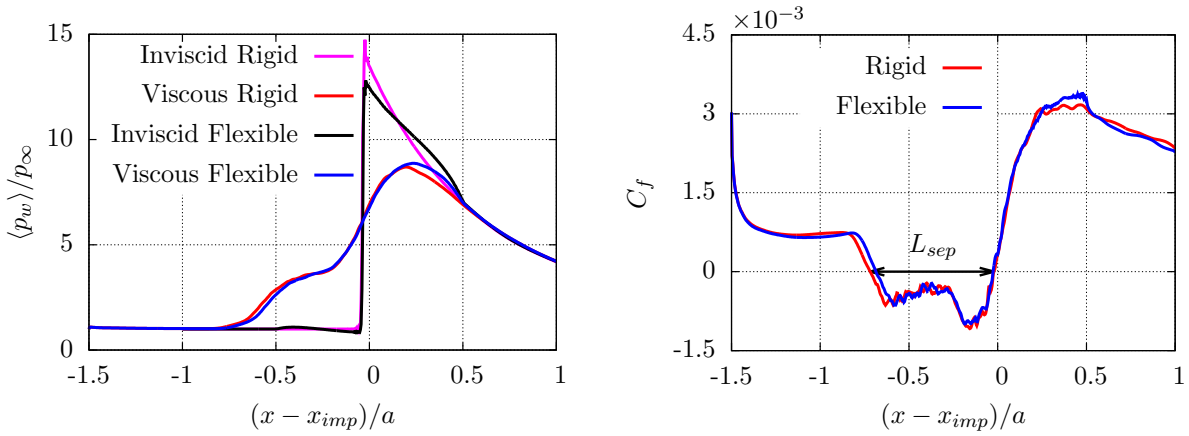

(a) Wall pressure

(b) Skin-friction coefficient

Figure 38: Skin-friction coefficient and wall pressure profiles for the rigid and flexible panels along the domain centerline $z = 0$. (a) Skin-friction coefficient, indicating extent of flow separation. (b) Time-mean wall pressure for different cases, including the inviscid rigid and flexible panels.

pressure rise due to the shock impingement and the downstream decrease of pressure due to the expansion wave are evident. The inviscid pressure profiles of Fig. 38(a) are steady, whereas the viscous wall pressure profiles are time-averaged. Notably, the response of the flexible panel to the inviscid shock impingement remains dynamically stable [58]. The inviscid shock impingement leads to a pressure rise of $p_3/p_1 \approx 15$ on the rigid panel; on the other hand, a slightly lower pressure rise of $p_3/p_1 \approx 12.5$ is exhibited on the flexible panel. In the viscous cases, the SBLI manifests in a pressure rise of approximately $p_3/p_1 \approx 8.5$, exhibiting the characteristic two-step pressure rise as opposed to the step rise of pressure in the inviscid cases. The two-step wall pressure profiles for the rigid and flexible panels are marginally different, particularly in the near upstream regions of the leading and trailing edges of the panel.

The time-mean wall skin-friction coefficient, C_f, along the streamwise distance is displayed in Fig. 38(a) for the rigid and flexible cases:

$$C_f = \frac{\langle \tau_w \rangle}{\frac{1}{2}\rho_\infty u_\infty^2} \quad \text{with} \quad \tau_w = \mu \frac{du}{dy}\bigg|_w, \tag{37}$$

where τ_w is the local shear stress at the wall. The strong adverse pressure due to SBLI results in a large flow recirculation region, $C_f < 0$, separating at $(x - x_{imp})/a \approx -0.7$ till the reattachment near the shock impingement location $(x - x_{imp})/a = 0$, in the mean sense. The separation length for the flexible panel case is $L_{sep} \approx 0.7$ ($\approx 23.33\delta_{in}$), which is slightly higher for the rigid panel case, consistent with the literature [28, 96–98].

The flow unsteadiness including the aforementioned characteristics low-frequency oscillations of SBLI are displayed in Fig. 39, in terms of the pre-multiplied wall pressure power spectral density (PSD) along the domain centerline ($z = 0$) for both the rigid and flexible cases. It is evident that the increased time-mean wall pressure and flow separation due the strong SBLI is also accompanied by a significant increase of the flow unsteadiness. The non-dimensional Strouhal number, defined as $St = fL_{sep}/u_\infty$, is based on the streamwise extent of the flow separation bubble as a characteristic length scale. Typically, the flow

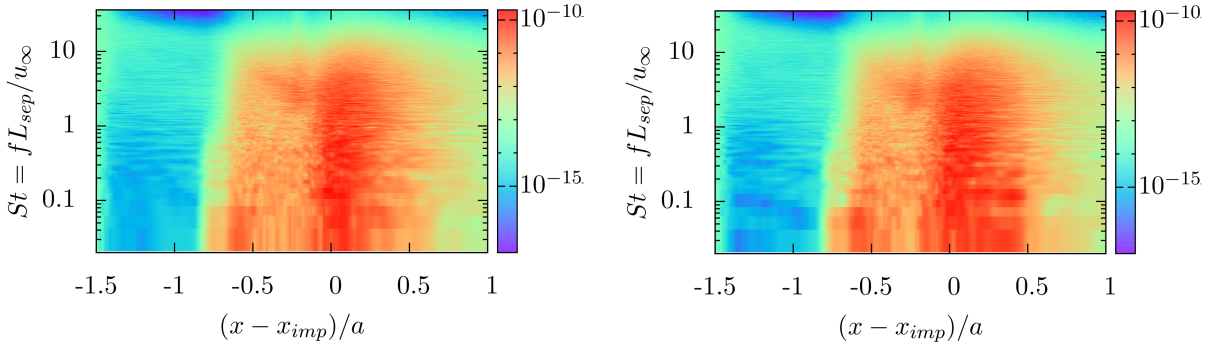

(a) Rigid

(b) Flexible

Figure 39: Wall pressure spectra along the centerline ($z = 0$) for the (a) rigid and (b) flexible panel cases.

separation bubble of SBLI oscillates at the Strouhal of $St \approx 0.03$, which is a few orders of magnitude lower compared to the characteristic frequencies of the incoming turbulent boundary layer. The strong SBLI over the rigid (Fig. 39 a) and flexible (Fig. 39b) panel cases clearly indicate the increased level of wall pressure PSD in the flow separation region and downstream of the shock impingement location. In general, the wall pressure PSD levels are higher for the flexible panel case (Fig. 39 b), particularly near and downstream of the shock impingement location, where the PSD peaks are more spread compared to the rigid panel case.

The dynamic interactions between the SBLI and flexible panel manifest into the modification of the incoming turbulent boundary layer as well as the deflection of the flexible panel in a fully coupled unsteady manner. To understand the individual effects, in Section 6.1 and in [60] we examined the modification of the incoming turbulent boundary layer due to static surface deformation. The Mach 4 turbulent boundary layer is subjected to Mode(1,1) and Mode(2,1) static deformations [60], which led to flow separation, the low-frequency unsteadiness and increased level of flow turbulence downstream - the effects similar due to the SBLI. In the following (Sec. 6.4.2), we examine the response of flexible panel subjected to SBLI forces that are obtained on a rigid wall (one-way interaction from fluid to structure), in addition to the two-way FSI.

6.4.2 Response of flexible panel to SBLI

The response of the flexible panel is displayed in Fig. 40, where the one-way (fluid to structure) and two-way FSI simulations use the same initial conditions. Figure 40(a) shows the panel deflection at the $3/4$th chord location for the two cases, exhibiting an initial transient for $tu_\infty/a \lessapprox 100$. The effect of two-way interaction becomes evident at $tu_\infty/a \approx 50$, leading to a lagged panel deflection with a lower amplitude oscillation as compared to the uncoupled panel response. There are two potential sources for these differences. First is that the coupled response will include both aerodynamic damping and stiffness terms that arise due to pressure forces that change due to surface velocity and displacement, respectively [93]. These general effects are present even in the absence of an SBLI. The second, more complicated and much less understood source, is coupling between the surface motion and dynamics of the SBLI. In particular, Brouwer et al. [91] note that coupling between the structural motion and time mean separation length of the SBLI can induce phase shifts in the aeroelastic loads. Additionally, the increased levels of turbulence, observed in Fig. 39b, suggests that

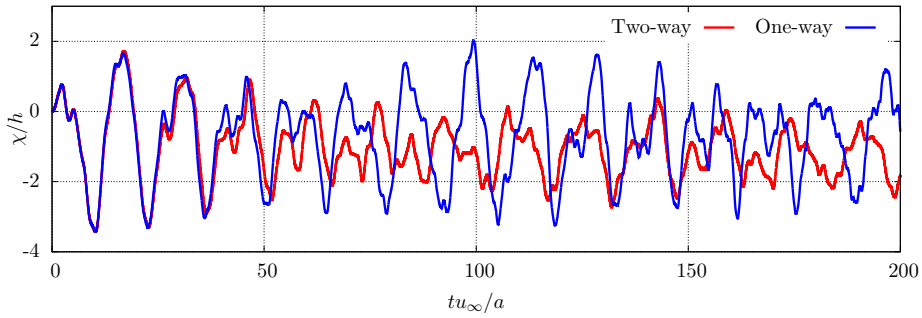

(a) Panel time response at the $3/4$-chord length centerline location

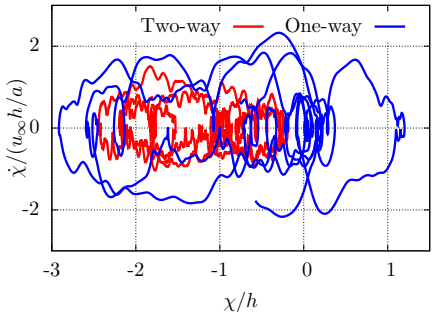

(b) Phase portrait, exhibiting sustained oscillations

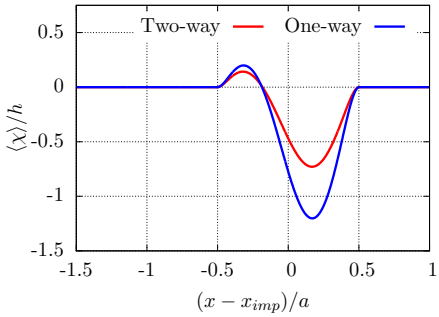

(c) Time-mean panel deflections along the centerline

Figure 40: Flexible panel response in two-way and one-way FSI settings. (a) Instantaneous panel deflection at the $3/4$-chord length location, (b) the last 3 cycles of the panel response at the panel $3/4$-chord length, and (c) time-mean panel deflection along the panel centerline for the two cases.

synchronization of the SBLI with the structural response in the two-way FSI has shifted to higher-energy structural modes. A consistent observation was made recently by Variagoda et al. [99].

The panel response to the SBLI exhibits sustained oscillations for the time window considered, displaying a aperiodic response in either case, as shown in terms of the phase portrait in Fig. 40(b). Figure 40(c) displays the time-averaged panel deflection along the panel centerline, where the mean-deflection is maximum at $(x - x_{imp})/a \approx 0.2$ (or at 0.7 panel chord length) for the two cases. The maximum time-mean deflections of the panel in the two-way and one-way FSI settings are $0.73h$ and $1.20h$, respectively, whereas the instantaneous maximum deflections are up to $\approx 3h$, particularly for the one-way case. The high panel deformations are expected to introduce structural non-linearities, particularly the non-linear coupling between the bending and stretching of the panel [100], leading to the increase of effective panel stiffness and thereby the effective natural frequency of the panel.

To assess the principal modes of panel vibration and associated modal frequencies, we employ the proper orthogonal decomposition method. The time-averaged panel deflection and energy dominant POD modes of the panel response for the two-way and one-way FSI cases are displayed in Fig. 41 and Fig. 42, respectively. The eigenvalues (Λ_n), normalized by the square of the panel thickness, of the first 10 high-energy ranked POD panel modes are shown in Fig. 41(a) for the two-way FSI response, whereas the eigenvalues for the one-way FSI response are displayed in Fig. 42(a). The first few modes in either case comprise most of the total modal energy. Overall, the one-way FSI response exhibits higher panel modal energies compared the

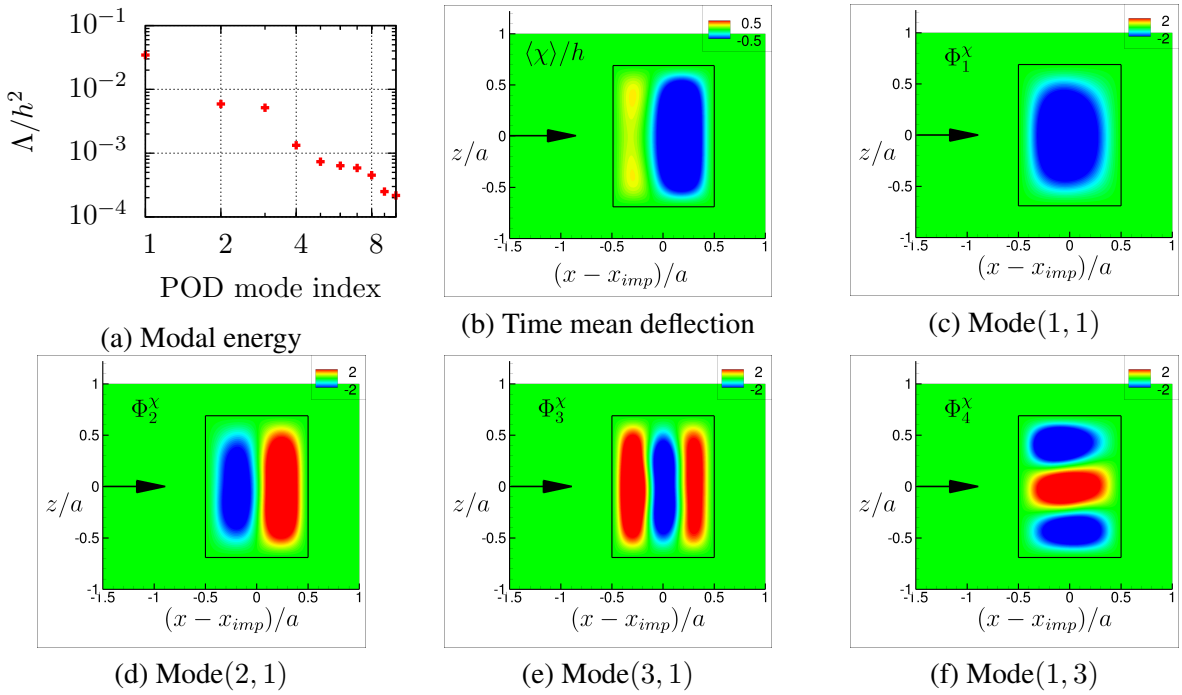

(a) Modal energy (b) Time mean deflection (c) Mode$(1, 1)$

(d) Mode$(2, 1)$ (e) Mode$(3, 1)$ (f) Mode$(1, 3)$

Figure 41: Energy dominant proper orthogonal decomposition modes of the panel response in the two-way FSI case.

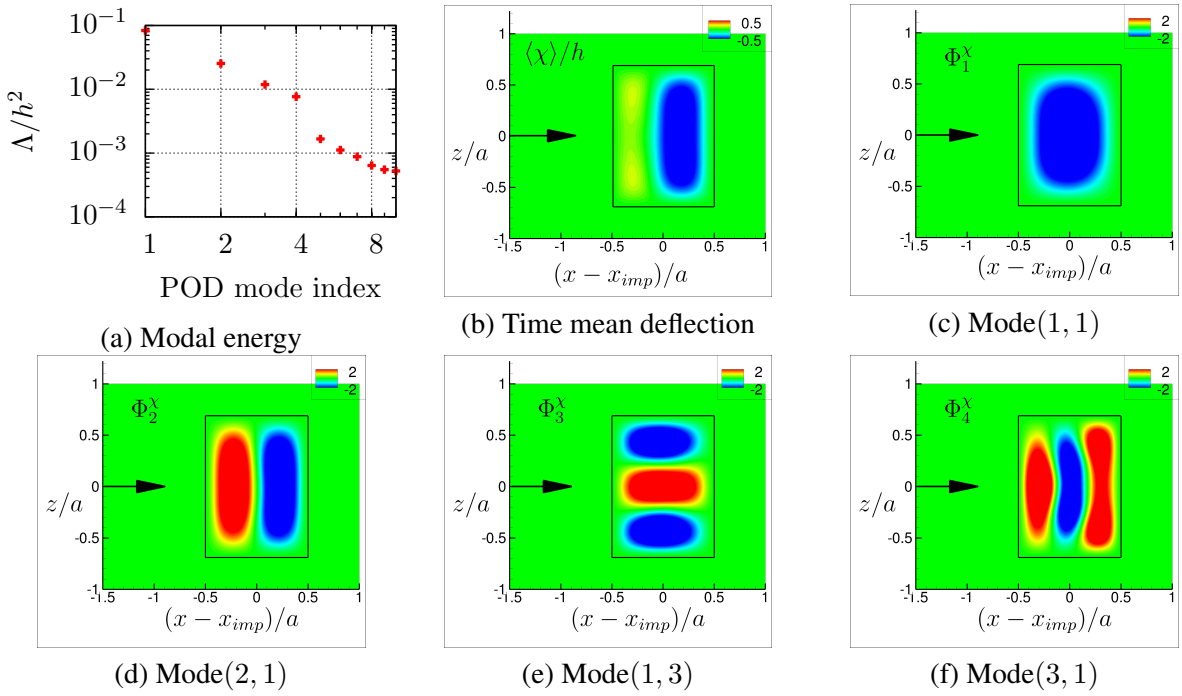

(a) Modal energy (b) Time mean deflection (c) Mode$(1, 1)$

(d) Mode$(2, 1)$ (e) Mode$(1, 3)$ (f) Mode$(3, 1)$

Figure 42: Energy dominant proper orthogonal decomposition modes of the panel response in the one-way FSI case.

	$St_\psi = f_\psi L_{sep}/u_\infty$	$f_\psi^{POD}\,(Hz)$	$f_\psi^{POD}\,(Hz)$	$f^N\,(Hz)$	$f^N\,(Hz)$
	two-way	two-way	one-way	free flat	free mean-deflected
Mode$(1,1)$	0.043	631	733	318	589
Mode$(2,1)$	0.095	1391	1415	754	1390
Mode$(3,1)$	0.133	1940	2127	1418	1887
Mode$(1,3)$	0.089	1293	1451	855	1166

Table 6: Modal frequencies of the vibration modes of panel that correspond to the energy dominant POD modes for coupled and free vibrations.

two-way FSI response. The time-mean panel deflections for the two cases (Fig. 41b and Fig. 42b) exhibit the mode shape of Mode$(2,1)$ due to the shock impingement near the mid-chord length of panel. The energy dominant first four POD modes of the panel deflection for the two cases comprise structural mode shapes of Mode$(1,1)$, Mode$(2,1)$, Mode$(3,1)$, and Mode$(1,3)$, as shown in subfigures (c,d,e, and f) of Fig. 41 and Fig. 42. Mode$(1,1)$ and Mode$(2,1)$ are the energy dominant modes for the both cases, while Mode$(3,1)$ and Mode$(1,3)$ exchange their ranks, with Mode$(3,1)$ being high-energy mode for the two-way FSI.

To examine the structural non-linearities, we analyze the modal frequencies of the panel response for the two-way and one-way FSI. The POD modal frequencies (f_ψ^{POD} in Hz) are obtained by means of the POD temporal coefficients for the two-way and one-way FSI cases, and are listed in Table 6. The Strouhal numbers corresponding to the POD modes in the two-way case coincide with the characteristic low/mid-range frequencies exhibited by the baseline SBLI over rigid flat panel. The modal frequencies for the one-way case are, in general, higher compared to the two-way case, which is also shown to exhibit diminished and phase-shifted panel deflections (Fig. 40a). The higher frequencies of the one-way FSI panel response are consistent with the larger amplitude of the panel deflection.

The natural frequencies of these structural modes are estimated by a standard perturbation analysis (or free vibration analysis) of an unloaded panel with the same material and geometric properties, and boundary conditions. The increase in modal frequencies (Table 6) is likely due to the structural non-linearity associated with the membrane forces in the panel. Furthermore, the free-vibration analysis is performed on a pre-loaded panel with the time-mean pressure of the rigid viscous SBLI case (see Fig. 38b), where the modal frequencies are lower (Table 6) as compared to the modal frequencies of the panel dynamic response. The differences in modal frequencies between the one-way / two-way FSI and unloaded panel free vibration is clearly partially due to structural nonlinearity. However, further investigation is warranted to precisely understand the observed differences in modal frequencies between the static, one-way, and two-way FSI.

6.4.3 Dynamics of the two-way interaction of SBLI over flexible panel

The coupling between the SBLI and flexible panel is evident from the analyses presented in Sec. 6.4.1 and Sec. 6.4.2, where the SBLI exhibits a moderate decrease of the flow separation length and an overall increase of turbulence. On the other hand, the panel under SBLI manifests exhibits a sustained aperiodic oscillation with strong geometric nonlinearity and corresponding shifts in frequency response. As noted before, the panel oscillation ceases to exist for the inviscid shock impingement, emphasizing the role of the SBLI unsteadiness on inducing a dynamic FSI response. To analyze the dynamic coupling between the SBLI and panel vibration modes, we use dynamic mode decomposition [101], which finds basis in the

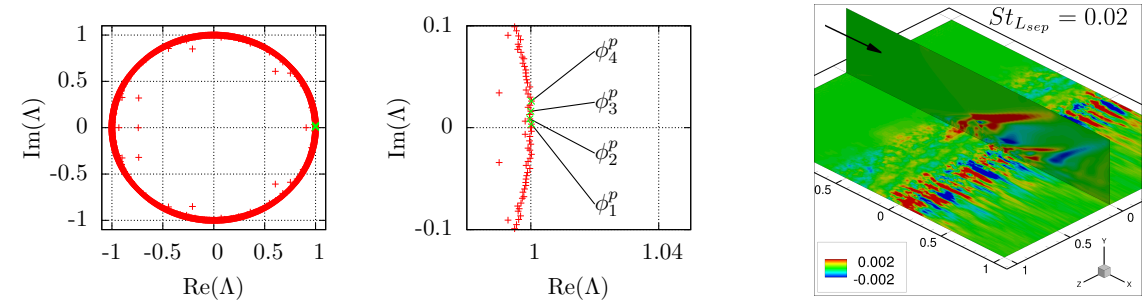

(a) Eigenvalue spectrum of the DMD modes.

(b) Re(ϕ_1^p)

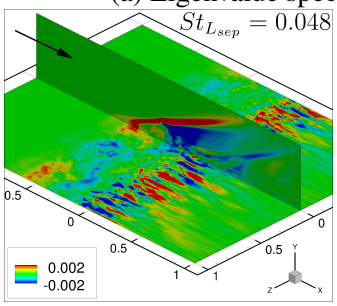

(c) Re(ϕ_2^p)

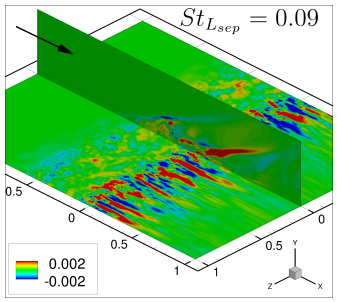

(d) Re(ϕ_3^p)

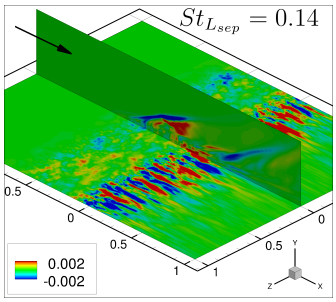

(e) Re(ϕ_4^p)

Figure 43: Dynamic modes (DMD modes) of the pressure for the baseline (rigid surface) SBLI. The DMD modes ϕ_2^p, ϕ_3^p, and ϕ_4^p correspond to the Strouhal numbers of structural modes Mode(1,1), Mode(2,1), and Mode(3,1) of Table 6, respectively.

Koopman theory [102]. As opposed to POD, which focuses on the maximization of the modal energy, DMD extracts spatially coherent flow structures, where each mode evolves in time with unique frequency and growth/decay rate. We employ the standard DMD procedure presented by [101].

DMD of the SBLI over rigid panel, in Fig. 43 in terms of the pressure, reveals the flow features that correspond to the panel vibration modes. Figure 43(a) displays the eigenvalue spectrum or Ritz values in complex plane (left frame), where the DMD modes of the pressure at the Strouhal numbers $St = 0.02$, 0.048, 0.09, and 0.14 are identified (right frame). The first DMD mode ϕ_1^p exhibits $St = 0.02$, which is close to the first sub-harmonic of the first mode of panel deflection. The DMD modes ϕ_2^p, ϕ_3^p, and ϕ_4^p that exhibit frequencies $St_{L_{sep}} = 0.048$, $St_{L_{sep}} = 0.09$, and $St_{L_{sep}} = 0.14$, correspond to the panel vibration modes Mode$(1, 1)$, Mode$(2, 1)$, and Mode$(3, 1)$, respectively. The DMD flow features, in Figs. 43(b,c,d,e), mainly comprise the reflected shock dynamics and the scales of turbulence that are relevant to the interaction.

Similar DMD analysis of the SBLI over rigid surface has been performed previously, for instance by [103], and [104], in order to investigate the stability, three-dimensionality, and unsteady dynamics of the flow. In general these studies considered spanwise-averaged two-dimensional flow fields, whereas in the present work the pressure is not spanwise averaged. The DMD modes ϕ_2^p and ϕ_3^p (Fig. 43) are characteristically similar to the DMD modes of the pressure obtained by [103] at $St = 0.039$ and $St = 0.114$, respectively, exhibiting the dynamics between the reflected compression and expansions waves as well as the separation bubble residing at the shock foot. In addition, the DMD modes of Fig. 43 display the spatial distribution of the mode shape on the bottom wall, indicating the extent of flow structures exhibiting the corresponding unsteadiness.

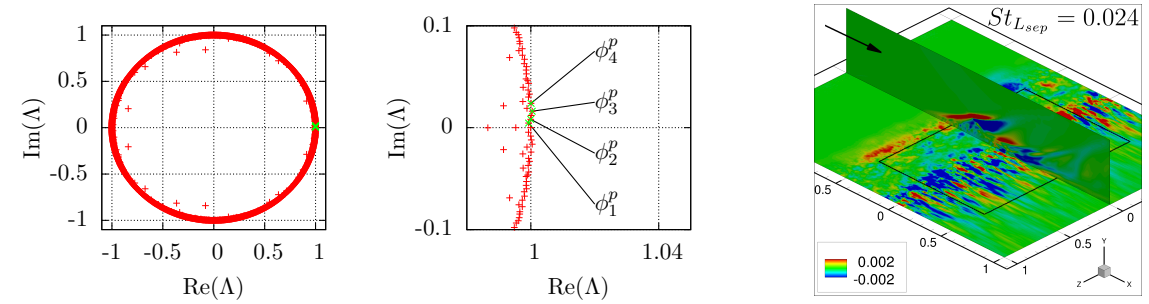

(a) Eigenvalue spectrum of the DMD modes.

(b) Re(ϕ_1^p)

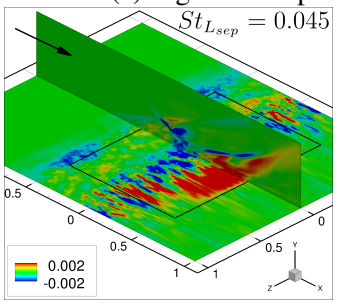

(c) Re(ϕ_2^p)

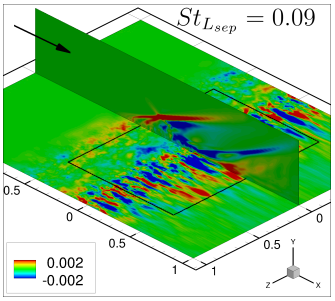

(d) Re(ϕ_3^p)

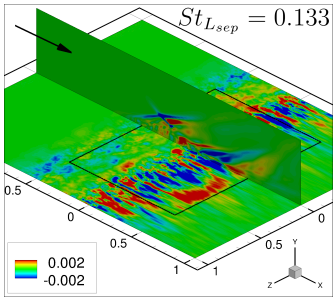

(e) Re(ϕ_4^p)

Figure 44: Lagrangian DMD modes of the pressure for the two-way flexible panel case. The LDMD modes ϕ_2^p, ϕ_3^p, and ϕ_4^p correspond to the Strouhal numbers of structural modes Mode(1,1), Mode(2,1), and Mode(3,1) of Table 6, respectively.

In general, the domain (mesh) deformation in FSI poses difficulty in performing modal decomposition techniques such as the POD and DMD. This problem has been addressed recently in [95], where the conventional modal analyses that utilize the Eulerian frame of reference are reformulated in Lagrangian frame of reference. For flows with deforming meshes, the frame of reference can be the material surfaces (the Lagrangian particles) or the moving mesh itself. In the present case, the computational mesh above the flexible panel deforms to accommodate the panel deflections. Thus, we employ the Lagrangian modal analysis (LMA) by considering the moving mesh as the frame of reference for the modal analysis. The method successfully separates the modes associated with the mesh deformation from the standard modes of the flow fields, as detailed in [95].

Figure 44 displays the Lagrangian DMD (LDMD) modes of the pressure fields in the SBLI over the flexible panel. The LDMD Ritz spectrum is displayed in Fig. 44(a) with the LDMD modes at $St_{L_{sep}} = 0.024$, $St_{L_{sep}} = 0.048$, $St_{L_{sep}} = 0.09$, and $St_{L_{sep}} = 0.133$ that are identified in the right frame. The real parts of the LDMD modes are displayed in Fig. 44(b,c,d,e), respectively. In general, the LDMD modal shapes are considerably altered for the SBLI over flexible panel, displaying a higher degree of spanwise coherence, particularly on the surface of the flexible panel (delineated with the bold rectangle). Interestingly, the reflected shock structures associated with Mode$(1,1)$ for the SBLI over rigid surface (Fig. 43) are, to some degree, muted for the SBLI over flexible panel (Fig. 44c). Conversely, the reflected shock structures associated with Mode$(2,1)$ (Fig. 43d) become prominent for the SBLI over flexible panel (Fig. 44d).

To further elucidate the exchange of energy between the SBLI and flexible panel, we perform POD on the pressure fields, comprising the wall pressure. The POD modal energies for the SBLI over rigid and flexible

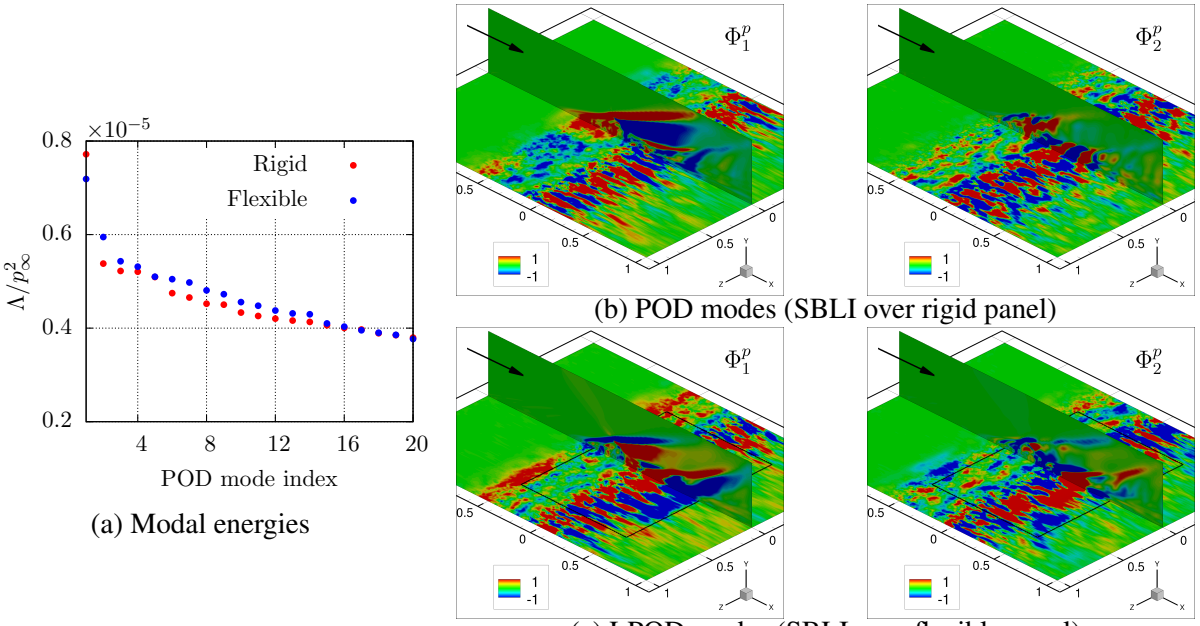

(a) Modal energies

(b) POD modes (SBLI over rigid panel)

(c) LPOD modes (SBLI over flexible panel)

Figure 45: POD modes of the pressure fields in the SBLI over rigid and flexible panels.

panel are compared in Fig. 45(a), displaying the first two energy-dominant POD modes for the rigid and flexible panels in Fig. 45(b) and Fig. 45(c), respectively. The overall increase of the turbulent pressure fluctuations, in Fig. 45(a), for the flexible panel case is evident in terms of the higher level of POD modal energies compared to the rigid panel case; this is congruous with the overall higher levels of wall pressure PSD in Fig. 39(b). Furthermore, the higher amplitude oscillation of the one-way FSI (Fig. 40) is consistent with the higher modal energy of the first POD mode (Fig. 45b) in the SBLI over rigid panel.

6.4.4 Summary

We carried out simulations of a Mach 4 turbulent shock boundary layer interaction over a flexible panel. The dynamics between the SBLI and flexible panel is examined in using one-way (fluid to structure) and two-way fluid-structure interactions by means of a recently developed FSI solver framework (FDFEM). In the one-way FSI, the instantaneous wall pressure fields from the SBLI over rigid surface are transmitted without structural feedback to the structural solver to obtain the panel response. The strong SBLI ($p_3/p_1 \approx 8.5$) induces a large flow separation ($L_{sep} \approx 23\delta_{in}$), which marginally decreases in the presence of flexible panel, in the time-mean sense.

The two-way FSI leads to a higher level flow turbulence, indicated by the increase of wall pressure PSD and the POD modal energies compared to the SBLI over rigid panel. However, the one-way FSI exhibits higher panel deflections as compared to the two-way FSI. The energy exchange between the SBLI and panel oscillation also manifests into the POD modal energies of the SBLI pressure fields, where the first POD mode for the flexible panel case is at a lower energy, whereas the higher rank POD modes contain relatively more energy compared to the rigid panel case. The panel response in both the two-way and one-way FSI comprises structural modes, namely, Mode$(1,1)$, Mode$(2,1)$, Mode$(3,1)$, and Mode$(1,3)$, with a rank change between Mode$(3,1)$ and Mode$(1,3)$ for the one-way FSI. This shift indicates predominantly streamwise panel response in the two-way FSI, while the one-way FSI has strong streamwise and spanwise

P_0 [kPa]	P_∞ [kPa]	U_∞ [m/s]	T_∞ [K]	ρ_∞ $[kg/m^3]$	R_e $[m^{-1}]$
100	0.59	670	69	0.03	4.45×10^6
650	3.86	670	69	0.20	2.89×10^7

Table 7: Ludwieg Tube Freestream Conditions

panel responses. The large time-mean and instantaneous deflections ($\sim 1h$) of the panel due to shock impingement and dynamics of the SBLI induces a nonlinear structural response associated with the panel membrane forces. This at least partially explains increased panel response frequencies, relative to the free vibration frequencies of the unloaded panel, in the one-way and two-way FSI.

Several, likely inter-related, mechanisms for differences between the one-way and two-way FSI are noted, including: 1) classical aerodynamic stiffness and damping forces in the two-way interaction; 2) exchange of structural modal energies due to structural nonlinearity induced by the strong SBLI forces; and 3) transfer of energy in the SBLI that induces increased turbulence levels. In particular, the increased turbulence levels in the two-way FSI suggests synchronization of the SBLI-induced loads has shifted somewhat to higher-energy structural modes. However, more attention is needed to develop a precise understanding on the nuances of two-way interaction between a compliant panel and the dynamics of SBLI.

6.5 Experiments

As mentioned previously, to study the complex phenomena associated with high-speed FSI we decouple the problem by looking at three classes of models which progressively increase the possible fluid-structure coupling. In Section 6.5.1, the results from the experiments on a rigid flat plate without the shock generator are shown. The rigid flat plate is the baseline case to characterize the boundary layer and test the diagnostic techniques. In Section 6.5.2, the statically deformed geometries are discussed. These statically deformed panels show how the flow responds to panel deformations on longer time scales. And in Section 6.5.4, the results of the experiments with the shock generator on the rigid flat plate and compliant panel insert will be shown. These experiments show how significant of an effect material compliance has on the flow structures from a SBLI.

The majority of the tests in the Ludwieg tube are carried out with a 250 kPa driver. A number of the statically deformed geometries tests used the 500 kPa driver pressure condition. The freestream conditions for these two driver pressures are given in Table 7.

6.5.1 Rigid Flat Plate Characterization

The rigid flat plate is studied with and without a boundary layer trip at the 250 kPa driver condition. The rigid flat plate experiments are performed to obtain baseline measurements of the boundary layer height and static pressure downstream of the panel insert. The pressure on the rigid flat plate is measured using the Kulite pressure transducers and PSP detailed in Section 5.1.4. The PSP profile for the untripped rigid flat plate is shown in Figure 46. The image is taken with an exposure time of 5 ms to get an average pressure profile on the rigid panel during test time. The static pressures measured by each of the Kulite transducers and the average pressure over the surface of the model from the PSP for a case without impingement and without a boundary layer trip are given in Table 8. The sensitivities of the Kulite and PSP measurements are limited by the calibration gauge to 0.1 kPa. The PSP shows that the pressure profile on the rigid flat plate is two dimensional ensuring that the panel is fully within the core flow of the facility and the static wedge model is wide enough that no disturbances from the edges of the model are effecting the panel loading.

$P_{upstream}$ [kPa]	$P_{downstream}$ [kPa]	P_{psp} [kPa]
1.8 ± 0.1	1.7 ± 0.1	1.8 ± 0.1

Table 8: Rigid flat plate static pressure measurements

In addition, the pressure measured from the paint intensity shows good agreement with the static pressure measured by both Kulite transducers; within the uncertainty all of the pressure measurements agree. Thus, we can conclude that our panels are free from disturbances from the tunnel walls and the edges of the flat plate model and there is no pressure gradient from the untripped flow on the surface of the plate.

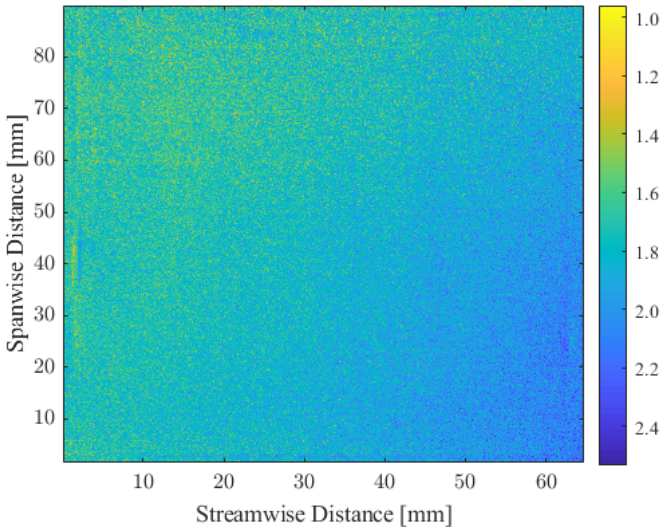

Figure 46: Pressure sensitive paint profile on rigid flat plate for a driver pressure of 250 kPa. Flow is from left to right

As mentioned previously, one of the main goals of the rigid flat plate experiments is to characterize the incoming boundary layer. Visual boundary layer thicknesses from schlieren videos of the rigid flat panel at a driver pressure of 250 kPa are initially found for the case without any boundary layer trip. First, the raw schlieren image is blurred using a 2D Gaussian filter with a standard deviation of 3. Next, the edges of the blurred image are found using the Canny method which finds edges by finding the local maxima of the gradient of the image intensity. The threshold value changes between images but is chosen such that the boundary layer is a continuous edge. Finally, the thickness is found from the processed image using the pixel to mm conversion found by imaging a ruler with the schlieren system.

The Reynolds number on the panel insert grows from 6.5×10^5 at the leading edge to 9.4×10^5 at the trailing edge. The transition Reynolds number depends on the unit Reynolds number and the smooth wall transition Reynolds number decreases with Mach number from 5.9×10^6 at $M_\infty = 1.97$ to 3.4×10^6 at $M_\infty = 3.84$ [105]. In addition, the visual boundary layer thickness growth rate over the panel insert is steeper than expected from the simulations from our collaborators at Ohio State for a fully turbulent boundary layer leading us to conclude that the untripped boundary layer is in the transitional regime. A boundary layer trip is thus needed at this condition to ensure a fully turbulent boundary layer over the panel inserts. However, Williams and Smits caution that boundary layer trips are facility dependent as the optimum

Sandpaper Grit	Roughness Height $[\mu m]$	$\%$ BL Height
120	115	7.9
100	140	9.7
80	190	13.1
60	265	18.3
50	348	24.0
40	425	29.3

Table 9: Roughness heights of various sandpaper boundary layer trips.

trip size depends on the tunnel freestream disturbance environment, the boundary layer development length, and the trip geometry. They suggest that to design an optimum trip the trip size needs to be varied until the mean velocity profile reaches a minimum corresponding to Coles' incompressible wake size correlation [106]. However, we don't currently have a system in place to measure velocity profiles in the Ludwieg tube boundary layer, thus, we chose to evaluate the visual boundary layer thickness over a wide range of trip heights.

The boundary layer is tripped using different roughness sandpaper strips. Each strip stretched spanwise across the model and is about 13 mm long streamwise and is placed 20 mm downstream of the model leading edge. The sandpaper grit, corresponding roughness height, and the ratio of the roughness height to the untripped boundary layer thickness at the trip location are reported in Table 9. The visual boundary layer thicknesses corresponding to the different roughness trips are shown in Figure 47. The untripped visual boundary layer thickness is also plotted in Figure 47. The visual boundary layer thickness is measured using the method detailed earlier for every increment of 5 ms during test time. Each data point in Figure 47 is the average value of the boundary layer thickness over the 60 ms test time and the error bars show the minimum and maximum visual boundary layer thickness measured during the test time. The boundary layer thickness is plotted from $x = 80$ mm downstream of the model leading edge to the trailing edge of the panel insert, $x = 211$ mm downstream of the model leading edge; the panel insert leading edge is the third data point in each series, $x = 145$ mm downstream of the model leading edge. In Figure 47 the untripped boundary layer clearly has the steepest growth rate over the panel insert. The boundary layer trips with roughness heights of $115\mu m$, $140\mu m$, and $190\mu m$ all have similar growth rates which are less steep then the untripped boundary layer. Each of these three boundary layers grow from roughly 3 mm to 3.6 mm over the length of the panel insert. The fact that three roughness heights varying by nearly $100\mu m$ result in nearly identical visual boundary layer thicknesses leads us to believe that these trip heights correspond to an effective boundary layer trip. For larger roughness trips of $265\mu m$, $348\mu m$, and $425\mu m$ the visual boundary layer growth rate begins to steepen and the visual thickness reaches values of nearly 6 mm in some cases. In addition to the steepening of the growth rate, the measured thickness varied much more over the test time than the cases with lower roughness. For the largest roughness case the panel trailing edge boundary layer thickness varied by over 0.5 mm over the course of test time. This leads us to conclude that this level of roughness is over-tripping the boundary layer and resulting in large scale motions which would slowly decay downstream if the model were longer. More analysis is required to ensure that the boundary layer trips are effectively causing the boundary layer to become turbulent and in the future we will be iterating with our collaborators at Ohio State to match our boundary layer to their predicted values, however, for the remainder of the work here we use a trip with $190\mu m$ roughness to control the boundary layer over the panel inserts.

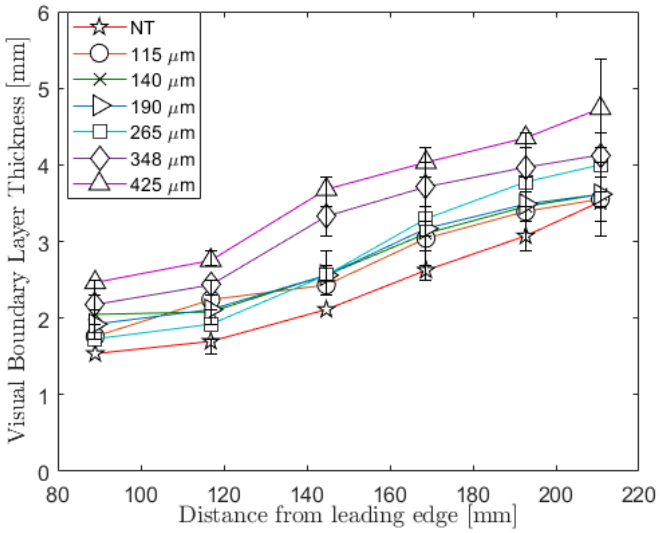

Figure 47: Visual boundary layer thickness for various sandpaper boundary layer trips.

6.5.2 Statically Deformed Geometries

Schlieren videos using the pulsed laser light source with a pulse width of 70 ns and static pressure traces are taken for each panel at driver pressures of 250 kPa and 500 kPa. A description of the deformed geometries used in these experiments is given is Section 5.1.3. A schlieren image of the first panel mode is shown in Figure 48. In each of the images, the white dashed lines show the location of the panel leading and trailing edges and the flow is from left to right. There is a shock at the leading edge of the panel insert, where the insert is not flush with the model. This is fixed for the rigid and compliant panel inserts and will be fixed in subsequent prints of the deformed geometries. From the schlieren image of the first mode, the flow remains attached over the deformed geometry, but, over the negative slope, the boundary layer height grows rapidly. Schlieren from the second panel mode is shown in Figure 49. This panel was studied in two orientations, the orientation shown in Figure 49 has the trough of the full wave upstream and the peak downstream. As can be seen in the schlieren image, there is a series of compression waves that form in the upstream trough and coalesce into a shock above the model. It can also be seen that the boundary layer grows rapidly after traveling over the peak of the wave similarly to what is observed in the first mode. The second orientation, with the peak upstream and the trough downstream, has very similar flow features. Again, compression waves are visible in the trough and coalesce into a shock. With the trough downstream the boundary layer growth behind the panel is more rapid than in the first orientation. The final deformed geometry studied is shown in Figure 50. The panel is oriented such that the trough is in the far-field and the peak is in the near-field. Here the flow looks very similar to the first mode and the compression waves that formed in the second mode are not visible from the trough of the wave.

These statically deformed geometries show how the flow responds to deformations on longer time scales than are achievable in the Ludwieg tube. In addition to schlieren videos, static pressure measurements were made 32 mm downstream of the panel inserts along the centerline for each case. The pressure measurements and visual boundary layer thicknesses at the panel insert leading and trailing edges are given in Table 10. The visual boundary layer thicknesses and error are found as discussed in Section 6.5.1 for the boundary

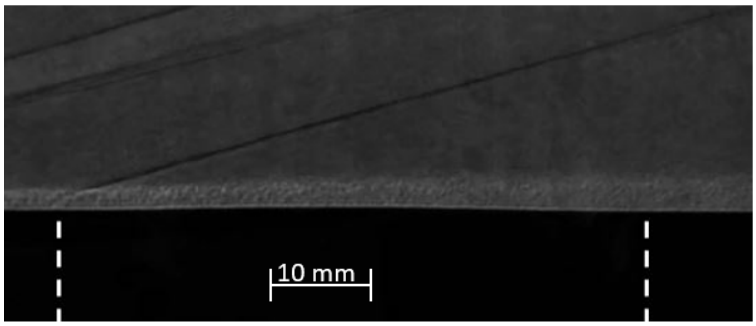

Figure 48: Statically deformed mode 11 boundary layer schlieren image, 500 kPa driver pressure, flow from left to right.

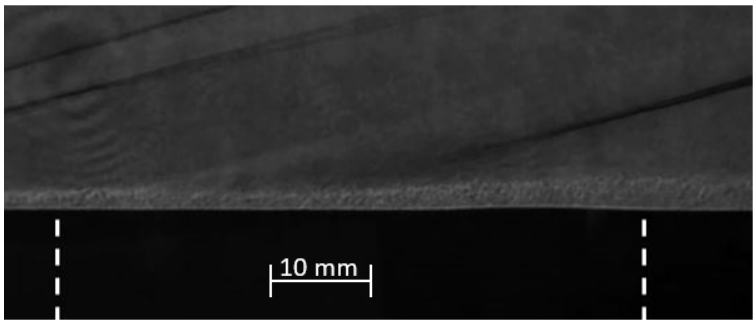

Figure 49: Statically deformed mode 12 boundary layer schlieren image, 500 kPa driver pressure, flow from left to right.

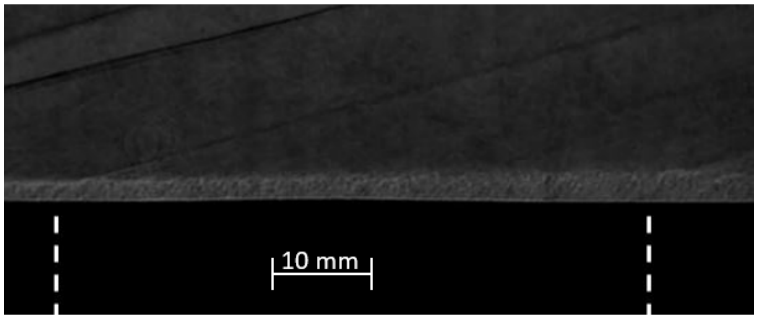

Figure 50: Statically deformed mode 21 boundary layer schlieren image, 500 kPa driver pressure, flow from left to right.

layer over the rigid flat plate. The boundary layer thickness at the leading edge of the panel inserts is similar across all of the geometries, including the flat plate. At the panel insert trailing edge each of the deformed geometries has a larger boundary layer thickness than the flat panel case. Panel 21 has the most variation in the visual thickness at the trailing edge with the boundary layer thickness fluctuating by nearly 1 mm during test time. Although there is clear visual evidence of the effect of the deformations on the flow field through the formation of compression waves and increased boundary layer growth, the Kulite pressure transducer did not measure noticeable pressure differences between the different cases. Moving forward, we plan to look at PSP on the surface of the deformed geometries and also look at additional statically deformed

Panel Shape	P [kPa]	δ_{LE} [mm]	δ_{TE} [mm]
00	1.7 ± 0.1	2.1 ± 0.1	3.1 ± 0.3
11	1.94 ± 0.2	2.4 ± 0.1	3.7 ± 0.2
12 (1)	1.94 ± 0.3	2.2 ± 0.1	3.9 ± 0.1
12 (2)	1.90 ± 0.3	2.1 ± 0.1	4.2 ± 0.4
21	1.92 ± 0.2	2.1 ± 0.3	3.5 ± 0.7

Table 10: Statically deformed panels visual boundary layer thickness, δ, and static pressure for 250 kPa driver. Kulite pressure measurements 32 mm downstream of panel trailing edge. Panel 12 (1) has downstream peak, panel 12 (2) has upstream peak.

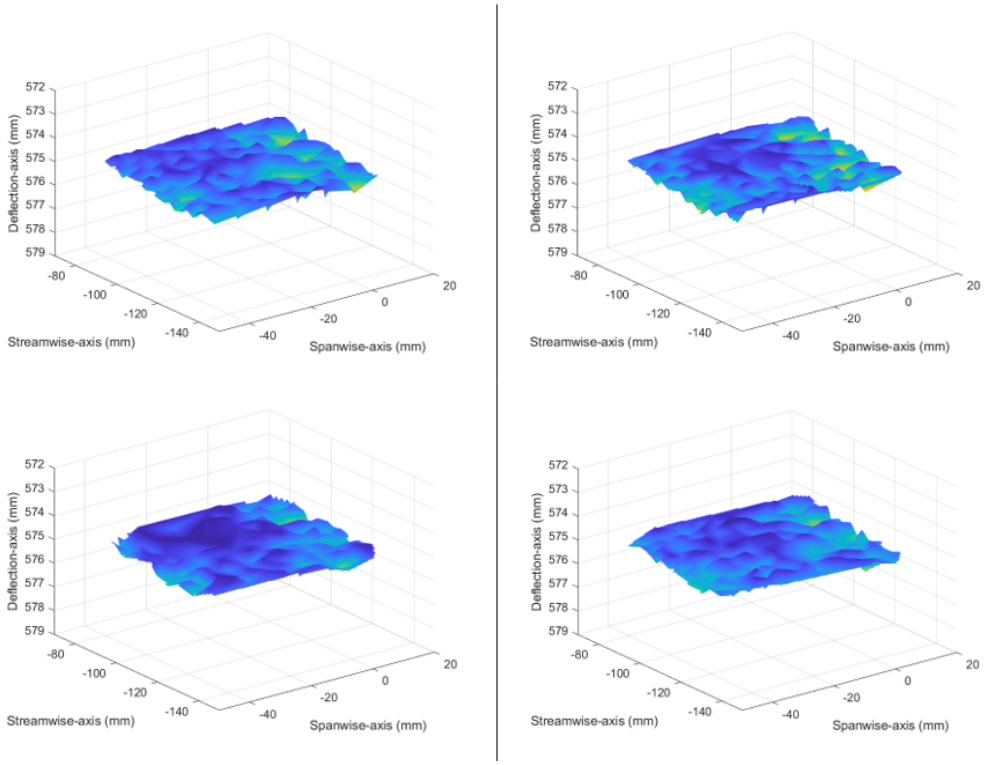

Table 11: Snapshots from high-speed (8000fps) photogrammetry measurements over compliant panel.

geometries, such as panel 11 with a cavity rather than peak, to gain further understanding into how these static deformations are affecting the flow.

6.5.3 Photogrammetric measurements of compliant panel response

As described in Section 6.5, single-camera photogrammetry was developed for absolute measurements of panel displacement. The camera was mounted above the test section such that simultaneous schlieren imaging of the flowfield can be carried out. Snapshots from preliminary experiments are shown in Figure 11. After the initial campaign, it was decided the image quality could be improved by modifications to the panel illumination, including uniformity of the light. This work is in progress under a follow-on effort. SPOD analysis will be carried out using the code of Towne et al. [107].

6.5.4 Shock Impingement

Following the rigid plate baseline and the statically deformed geometries, the oscillating shock generator is installed in the Ludwieg Tube test section. Initial experiments with the shock generator creating static impingements on both the rigid flat plate and the compliant insert are examined and the two cases will be compared in detail here. All of the impingement experiments are carried out at the 250 kPa driver condition given in Table 7. A labeled diagram of the flow structure from an SBLI created by the shock from the leading edge of the shock generator interacting with the rigid flat plate is shown in Figure 51. The black region at the base of the image is the flat plate model that houses the panel inserts. In this configuration the SBLI is occurring at the leading edge of the panel insert. Looking along the left edge of the image, the white region above the model surface is the mean incoming boundary layer. The boundary layer is tripped using the $190\mu m$ roughness trip discussed in Section 6.5.1. Also along the left edge, above the boundary layer are two shocks originating from the leading and trailing edges of the boundary layer trip and above that is the shock from the leading edge of the flat plate model. The shock originating from the shock generator is the clearly visible bright white line impinging on the flat plate model. The shock generator has a 35 degree angle and the shock wave angle in this configuration is 55 degrees before the interaction with the expansion wave originating on the shock generator. After the impinging shock interacts with the expansion, the shock wave angle interacting with the boundary layer is 38 degrees. Downstream of the impinging shock, on the shock generator are two expansions that turn the flow around the 35 degree wedge. Along the flat plate model, the impinging shock creates a separation region. This separation region results in an additional shock, labeled the separation shock. And finally downstream of the separation region we see the reattachment shock from the SBLI. The flow structure will contain these elements for every position of the shock generator on both the rigid and compliant surfaces.

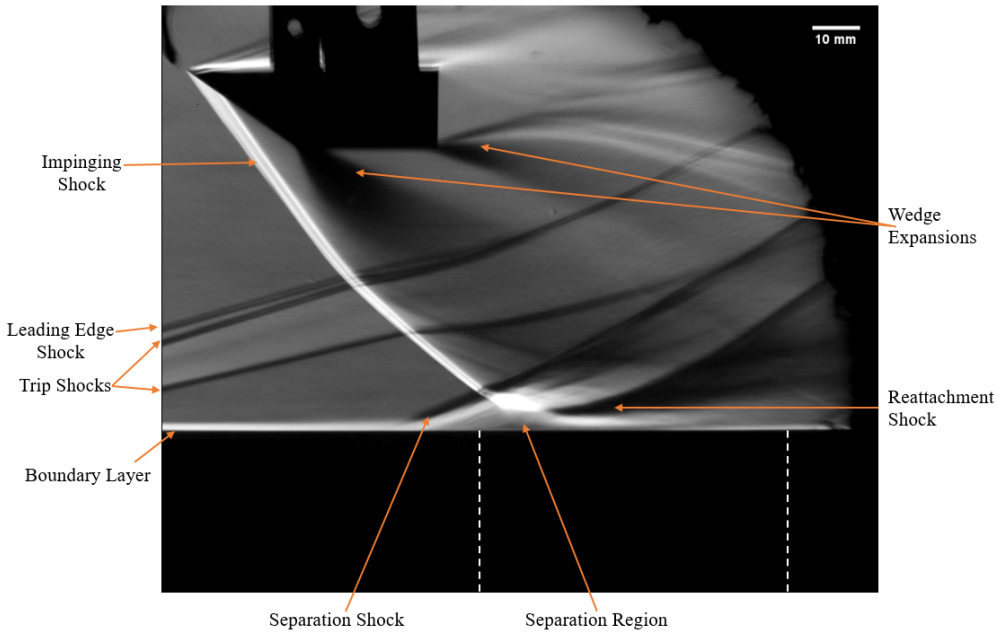

Figure 51: Static SBLI flow structure on rigid panel insert. Location of panel insert leading and trailing edges indicated by white dashed lines. Flow from left to right.

For the shock impingement case shown in Figures 55 and 56 the compliant panel displacement is measured using the Keyence LK-G407 laser displacement sensor detailed in Section 5.1.4. The panel response measurements are made at eleven locations on the compliant panel surface and an additional measurement is made on the rigid panel insert to ensure that the flow is not deflecting the laser light adding additional displacement to the measured values. The surface response interpolated around the eleven measurement locations on the compliant panel is shown in Figure 52. The response takes the shape of the first mode statically deformed geometry with a negative displacement, into the model cavity, of 0.76 mm, 3.8 panel thicknesses, at the center point. Along the edges of the surface where the panel is adhered to the rigid base the measured deformations are less than 0.1 mm. Higher resolution measurements using point and full field techniques are planned to obtain a better understanding of the panel motion.

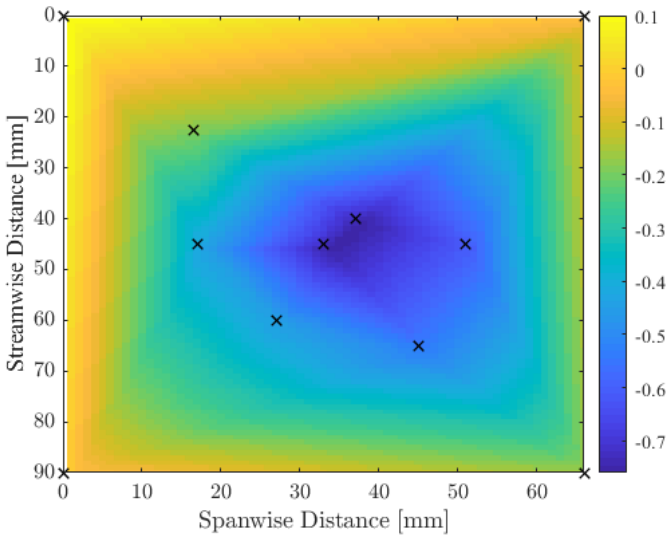

Figure 52: Panel surface response to forcing from static mid-panel impingement. Flow is from the left to right and displacements are given in mm.

Schlieren images for the SBLI on the leading edge of the panel insert are shown for the rigid panel in Figure 53(left) and for the compliant panel insert in 53(right). The most noticeable effect of the compliant panel on the SBLI occurs at the separation region. The height and length of the separation region measured from the schlieren images for both panel inserts are given in Table 12. For the SBLI over the rigid panel insert the height of the interaction zone reaches a peak height of 6 mm, or 2.3δ, where δ is the boundary layer thickness at the panel insert leading edge for the $190\mu m$ boundary layer trip given in Figure 47. Whereas for the SBLI over the compliant insert the height of the interaction zone reaches a peak height of 3.6 mm, 1.4δ. The displacement of the panel center point has a maximum value of 0.76 mm. Thus, the difference of the height in the separation region between the SBLI on the rigid and compliant panels is greater than the magnitude of the panel displacement. In addition to flattening the separation region, the compliant panel also appears to elongate the noticeably separated area in the schlieren images. Looking at the widest point of the separation region, near the model surface, in both schlieren images of Figure 53 the compliant surface elongates this region from just over 24 mm, 9.4δ, in the rigid case to 30 mm, 11.7δ. If we project the impinging shock through the interaction zone onto the panel surface, inviscid impingement, the shock would impinge on the rigid panel 12.7 mm downstream of the panel leading edge. If we assume that the compliant panel deforms

	Rigid Panel	Compliant Panel
Separation Height	6.0 ± 0.3	3.6 ± 0.2
Separation Length	24.2 ± 1.4	30.0 ± 0.5

Table 12: Separation region measurements for panel leading edge SBLI. All values given in mm

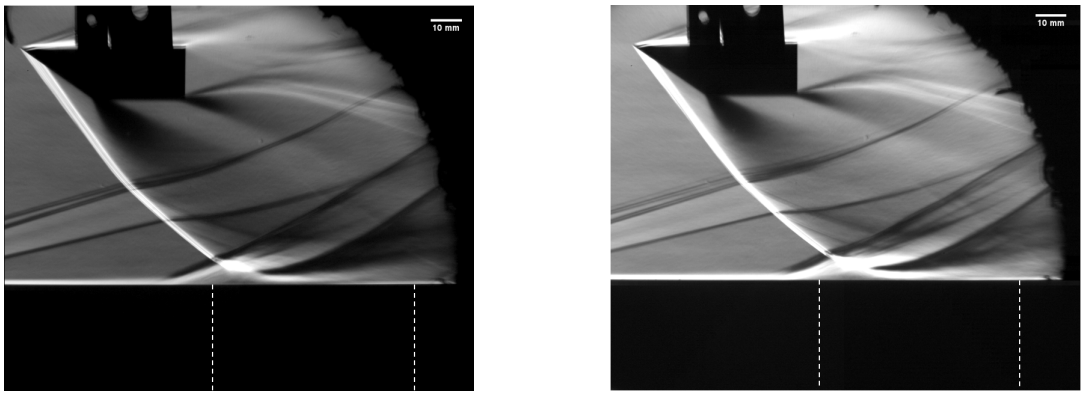

Figure 53: SBLI on leading edge of the panel insert for the rigid panel (left) and compliant panel (right). Location of the panel insert leading and trailing edges indicated by white dashed lines. Flow direction is left to right.

ideally into the first panel mode with a cavity amplitude of 0.76 mm, the impinging shock would intersect the panel 13.5 mm downstream of the panel leading edge.

PSP profiles of the panel surface are shown for the rigid panel in Figure 54 (left) and for the compliant panel in Figure 54 (right). The PSP images are taken with a long, 5 ms exposure, 35 ms into the test time so the pressure represents the average pressure on the surface of the model during test time. The pressure profile on the rigid panel shows clearly that the impingement loading is imparting a 2D pressure wave on the surface of the panel inserts and there are no detectable disturbances from the edges of the shock generator propagating down onto the panel surface. The pressure profiles from the PSP measurements are similar to the profile predicted by the AMRITA simulation in Figure 18. Both panels show elevated pressure over most of the panel insert before decreasing back towards the static pressure measured for the case without impingement. However, we also see very clearly in the rigid panel case but also in the compliant case that there is a peak pressure on the leading edge of the panel insert that is greater than the pressure anywhere else. The maximum pressure rise on the rigid panel due to the SBLI occurs along the leading edge, stretching about 5 mm downstream onto the panel, and is just under 7.5 times the predicted freestream static pressure which is slightly lower than the 8.5 peak pressure rise on the surface predicted by the AMRITA simulations. The peak pressure occurs upstream of the inviscid extension of the interaction which is projected 12.7 mm downstream of the panel leading edge for the rigid case and 13.5 mm downstream for the compliant case. Comparing the compliant panel surface pressure to the rigid case we see lower pressures at every corresponding point. This is most noticeable on the trailing edge of the panel inserts where the pressure on the compliant surface is about 38% lower than the rigid panel pressure. The point of highest pressure on the compliant surface is again on the leading edge of the panel insert, but, in the compliant case the maximum pressure rise is reduced to closer to 6 times the predicted freestream static pressure.

We next look at schlieren images and PSP profiles of the impingement located near the center of the panel

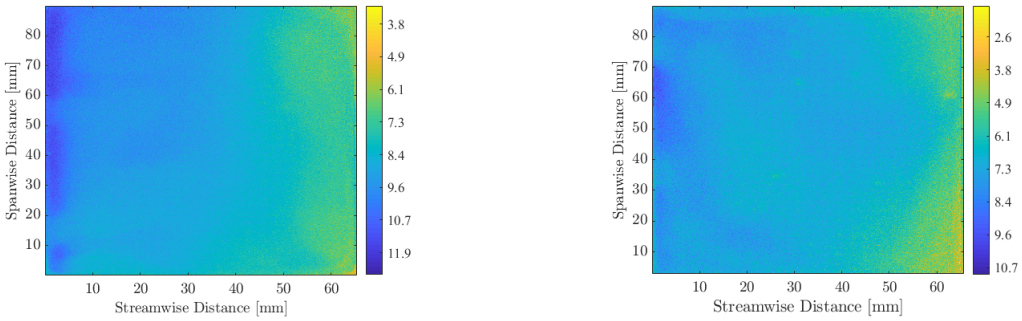

Figure 54: PSP of SBLI on leading edge of the panel insert for the rigid panel (left) and compliant panel (right). Panel leading edge 145 mm downstream of model leading edge. Pressure given in kPa. Inviscid shock impingement is projected to be at a) 12.7 mm and b) 13.5 mm. Note the difference in scale between the two images. Flow direction is left to right.

inserts. Schlieren images for the SBLI occurring near the midpoint of the panel insert, caused by rotating the shock generator 10 degrees, are shown for the rigid panel insert in Figure 55 (left) and for the compliant panel insert in Figure 55 (right). As can be seen in both schlieren images in Figure 55, the shock reflection has transitioned to a regular reflection and the shock wave angle has decreased to 38 degrees before the interaction with the wedge expansion. The shock wave angle of the impinging shock after interacting with the expansion wave is 30 degrees. The measurements of the separation region over the rigid and compliant panels are given in Table 13. In this shock generator configuration, the peak height of the interaction zone is lower than the peak height of the separation when the leading edge of the shock generator is in line with the flow for both the rigid and compliant panels. There is a similar effect of the compliance creating a flatter, longer separation region at the interaction location although the effect is not as large in this impingement configuration. The peak height of the interaction zone decreases from 1.5δ over the rigid panel to 0.8δ over the compliant panel and the length increases from 6.3δ over the rigid panel to 7.2δ over the compliant panel. Again, the change in height of the interaction zone, 1.7 mm, is greater than the panel center point displacement, 0.76 mm (3.8 panel thicknesses). If we again project the impinging shock onto the surface of the panel inserts, for the rigid panel the shock intersects the panel 38.8 mm downstream of the panel leading edge. And assuming the same idealized deformation of the compliant surface, the impinging shock wave intersects the compliant surface 40.1 mm downstream of the panel leading edge.

The PSP profiles for the mid-panel shock impingement are shown for the rigid panel insert in Figure 56 (left) and for the compliant panel in Figure 56 (right). These PSP images are again taken with a 5 ms exposure, 35 ms into the test time. The white dashed lines show the average separation length measured from the schlieren videos. For the compliant panel insert the separation region is very well defined on the surface of the model and the pressure in this region is lower than the freestream static pressure. Outside of the separation region the pressure is elevated to 4 times the predicted freestream static pressure. For the rigid panel, the separation region is not a defined low pressure region corresponding to the separation. This could be due to unsteadiness in the separation region that is averaged out during the long exposure. Additional images are needed to understand this interaction region over the rigid panel. The pressure on the surface of the rigid panel insert is again much higher than the pressure measured on the surface of the compliant panel as it is with the leading edge impingement. This shows that for the same tunnel conditions and impingement locations the compliance of the panel has a large effect on the surface pressure.

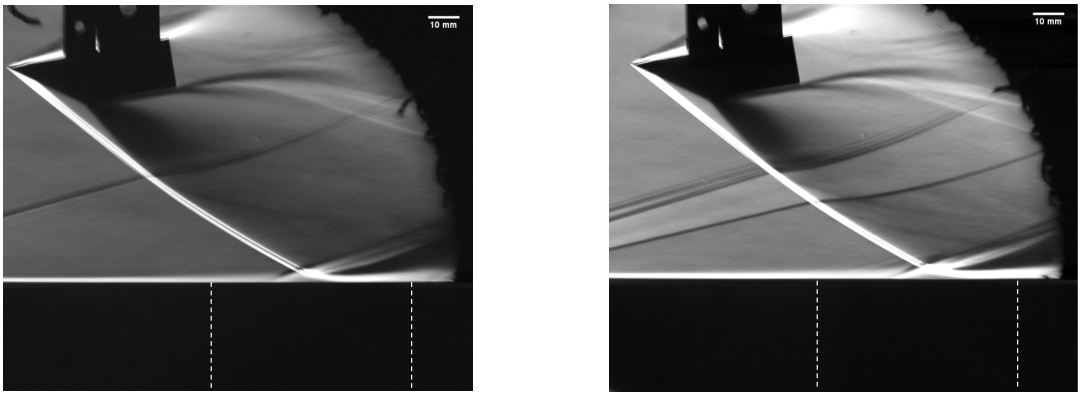

Figure 55: SBLI from shock generator rotated 10 degrees for the rigid panel (left) and compliant panel (right). Location of panel insert leading and trailing edges indicated by white dashed lines. Flow direction is from left to right.

	Rigid Panel	Compliant Panel
Separation Height	3.8 ± 0.2	2.1 ± 0.2
Separation Length	16.2 ± 1.1	18.5 ± 0.6

Table 13: Separation region measurements for mid-panel SBLI. All values given in mm

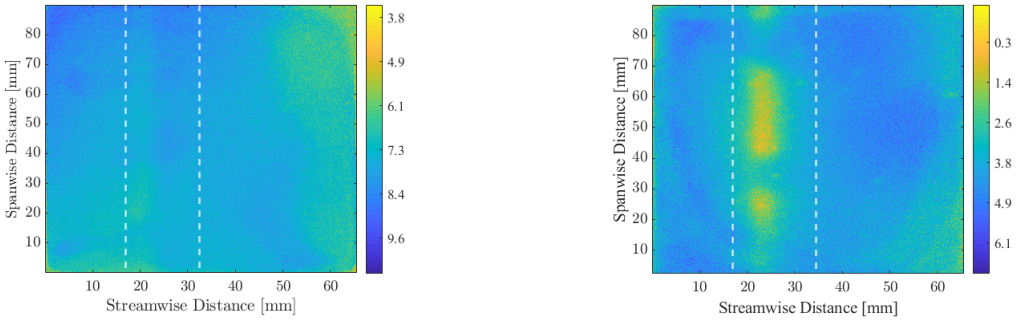

Figure 56: PSP of SBLI on mid-point of panel insert for rigid panel insert (left) and compliant panel insert (right). White dashed lines show separation region measured from schlieren video. Panel leading edge 145 mm downstream of model leading edge. Pressure given in kPa. Inviscid shock impingement is projected to be at a) 38.8 mm and b) 40.1 mm. Note the difference in scale of the two images.Flow direction is left to right.

7 Publications and Presentations

7.1 Student Theses

1. Becks, A. Linking Static Structural Surface Topology Changes to Supersonic Turbulent Boundary Layer Flow Separation. MS Thesis. The Ohio State University. Spring 2022 (expected).

7.2 Conference Proceedings

1. Shinde, V.J., McNamara, J.J. and Gaitonde, D.V., 2021. Shock Wave Turbulent Boundary Layer

Interaction Over a Flexible Panel. In AIAA Scitech 2021 Forum (p. 0488).

2. Patel, V., Parthasarathy, S., Shinde, V.J. and Gaitonde, D.V., 2021. Machine Learning Based Model Reduction for Fluid-Structure Interaction. In AIAA Scitech 2021 Forum (p. 1747).
3. Shinde, V.J., Gaitonde, D.V. and McNamara, J.J., 2020. Control of Shock Wave Turbulent Boundary Layer Interaction using Structurally Constrained Active Surface Morphing. In AIAA Scitech 2020 Forum (p. 0038).
4. Neet, M.C. and Austin, J.M. Effect of Surface Compliance on Shock Boundary Layer Interaction in the Caltech Mach 4 Ludwieg Tube, In AIAA Scitech 2020 Forum (p. 0816).
5. Shinde, V.J., McNamara, J.J. and Gaitonde, D.V., 2019. Effect of structural parameters on shock wave boundary layer induced panel flutter. In AIAA Aviation 2019 Forum (p. 3716).
6. Becks, A., Shinde, V., Deshmukh, R., McNamara, J.J. and Gaitonde, D.V., 2019. Characterizing the Modification of Turbulence Induced Loads Due to Structural Deformation. In AIAA Scitech 2019 Forum (p. 0758).
7. Shinde, V., Gaitonde, D.V. and McNamara, J.J., 2019. Control of transitional shock boundary layer interaction using surface morphing. In AIAA Scitech 2019 Forum (p. 1895).
8. Shinde, V., McNamara, J.J., Gaitonde, D.V., Barnes, C.J. and Visbal, M.R., 2018. Panel flutter induced by transitional shock wave boundary layer interaction. In 2018 Fluid Dynamics Conference (p. 3548).
9. Shinde, V., McNamara, J.J., Gaitonde, D.V., Barnes, C.J. and Visbal, M.R., 2018. Panel flutter induced by transitional shock wave boundary layer interaction. In AIAA Aviation 2018 Forum (p. 3548).

7.3 Archival Journal Publications

1. Shinde, V., McNamara, J., Gaitonde, D., 2022. Dynamic interaction between shock wave turbulent boundary layer and flexible panel. Journal of Fluids and Structures (In preparation).
2. Shinde, V., Becks, A., Deshmukh, R., McNamara, J., Gaitonde, D., Neet, M. and Austin, J., 2021. Spatially developing supersonic turbulent boundary layer subjected to static surface deformations. European Journal of Mechanics-B/Fluids, 89, 485-500.
3. Shinde, V.J., Gaitonde, D.V. and McNamara, J.J., 2021. Supersonic Turbulent Boundary-Layer Separation Control Using a Morphing Surface. AIAA Journal, 59(3), pp.912-926.
4. Shinde, V., McNamara, J. and Gaitonde, D., 2020. Control of transitional shock wave boundary layer interaction using structurally constrained surface morphing. Aerospace Science and Technology, 96, p.105545.
5. Shinde, V., McNamara, J., Gaitonde, D., Barnes, C. and Visbal, M., 2019. Transitional shock wave boundary layer interaction over a flexible panel. Journal of Fluids and Structures, 90, pp.263-285.

7.4 Seminars and Invited Talks

1. Shinde, V. High-Speed Fluid-Structure Interaction: Shock Boundary Layer Interaction on Compliant Thin Panels and Surface Morphing Control. At Aero-Propulsion, Mechatronics, and Energy, Florida State University, October 12, 2021.
2. McNamara, J. Challenges, Progress, and Emerging Directions of Fluid-Structure Interaction During Hypersonic Flight. Florida State University, October, 2020.
3. McNamara, J. Harnessing Hypersonics: A Multi-Physics Wonderland. University of Michigan, February, 2019.
4. McNamara, J. The Role of Fine Scale Boundary Layer Dynamics in High-Speed FSI: How Important Is It and How Can We Capture It?. Duke University, January, 2019.

5. McNamara, J. Numerical Analysis of High-Speed Boundary Layers Interacting with a Compliant Surface, Joint Experimental-Computational Efforts in High-Speed FSI (invited session), AIAA SciTech Conference, January, 2019.
6. Neet, M.C. and Austin, J.M. Dynamics of Interactions between Turbulent Boundary Layers and Compliant Surfaces, AIAA SciTech Conference, January, 2019.
7. Neet, M.C. and Austin, J.M. Periodic Loading of Mach 4 Boundary Layer over a Complaint Surface by an Oscillating Shock Generator, APS DFD Annual Meeting, November, 2019.
8. McNamara, J. Co-Simulation in High-Speed FSI: Where Are We and Where Should We Go? FSI Workshop, UNSW Canberra, AUS, May 2018.

References

[1] R. D. Blevins, D. Bofilios, I. Holehouse, V. W. Hwa, M. D. Tratt, A. L. Laganelli, P. Pozefsky, and M. Pierucci. *Thermo-vibro-acoustic loads and fatigue of hypersonic flight vehicle structure*. Tech. rep. Goodrich Aerostructures Group, June 2009.

[2] G. Tzong, R. Jacobs, and S. Liguore. *Predictive Capability for Hypersonic Structural Response and Life Prediction: Phase 1 – Identification of Knowledge Gaps, Volume 1-Nonproprietary Version*. Tech. rep. AFRL-RB-WP-TR-2010-3068. 2010.

[3] B. Zuchowski. *Predictive Capability for Hypersonic Structural Response and Life Prediction, Phase I – Identification of Knowledge Gaps*. Tech. rep. AFRL-RB-WP-TR-2010-2069. 2010.

[4] R. Quiroz, J. Embler, R. Jacobs, G. Tzong, and S. Liguore. *Predictive Capability for Hypersonic Structural Response and Life Prediction: Phase II – Detailed Design of Hypersonic Cruise Vehicle Hot-Structure*. Tech. rep. AFRL-RQ-WP-TR-2012-0265. 2012.

[5] B. Zuchowski. *Predictive Capability for Hypersonic Structural Response and Life Prediction, Phase II – Detailed Design of Hypersonic Cruise Vehicle Hot-Structure*. Tech. rep. AFRL-RQ-WP-TR-2012-0280. 2012.

[6] S. Spottswood, T. Eason, and T. Beberniss. "Influence of shock-boundary layer interactions on the dynamic response of a flexible panel". In: *Proceedings of the ISMA-2012* (2012), pp. 17–19.

[7] D. Bies. "A review of flight and wind tunnel measurements of boundary layer pressure fluctuations and induced structural response". en. In: *undefined* (1966).

[8] A. J. Smits and J.-P. Dussauge. *Turbulent Shear Layers in Supersonic Flow*. 2nd ed. Springer Science & Business Media, 2006.

[9] D. S. Dolling. "Fifty Years of Shock-Wave/Boundary-Layer Interaction Research: What Next?" In: *AIAA Journal* 39.8 (Aug. 2001), pp. 1517–1531.

[10] D. V. Gaitonde. "Progress in shock wave/boundary layer interactions". In: *Progress in Aerospace Sciences* 72 (2015). Publisher: Elsevier, pp. 80–99.

[11] L. Maestrello. "Use of turbulent model to calculate the vibration and radiation responses of a panel, with practical suggestions for reducing sound level". In: *Journal of Sound Vibration* 5 (May 1967). ADS Bibcode: 1967JSV.....5..407M, 407, IN1, 421–420, IN1, 448.

[12] M. J. Crocker. "The response of a supersonic transport fuselage to boundary layer and to reverberant noise". In: *Journal of Sound Vibration* 9 (Jan. 1969). ADS Bibcode: 1969JSV.....9....6C, pp. 6–20.

[13] L. Maestrello. “Radiation from and panel response to a supersonic turbulent boundary layer”. In: (1969).

[14] L. Maestrello and T. L. J. Linden. “Measurements of the response of a panel excited by shock boundary-layer interaction”. In: *Journal of Sound Vibration* 16 (June 1971). ADS Bibcode: 1971JSV....16..385M, 385, IN2, 389–388, IN2, 391.

[15] L. Maestrello and T. Linden. “Response of an acoustically loaded panel excited by supersonically convected turbulence”. en. In: *Journal of Sound and Vibration* 16.3 (June 1971), pp. 365–384.

[16] C. F. Coe and W. Chyu. “Pressure-fluctuation inputs and response of panels underlying attached and separated supersonic turbulent boundary layers”. en. In: *undefined* (1972).

[17] A. L. Laganelli and H. F. Wolfe. “Prediction of fluctuating pressure in attached and separated turbulent boundary-layer flow”. In: *Journal of Aircraft* 30.6 (Nov. 1993). Publisher: American Institute of Aeronautics and Astronautics, pp. 962–970.

[18] R. Vaicaitis, C. M. Jan, and M. Shinozuka. “Nonlinear Panel Response from a Turbulent Boundary Layer”. In: *AIAA Journal* 10.7 (July 1972). Publisher: American Institute of Aeronautics and Astronautics, pp. 895–899.

[19] Y. F. Hwang, W. K. Bonness, and S. A. Hambric. “Comparison of semi-empirical models for turbulent boundary layer wall pressure spectra”. In: *Journal of Sound and Vibration* 319.1-2 (Jan. 2009), pp. 199–217.

[20] J. Rocha and D. Palumbo. “On the sensitivity of sound power radiated by aircraft panels to turbulent boundary layer parameters”. In: *Journal of Sound and Vibration* 331 (Oct. 2012), pp. 4785–4806.

[21] B. Liu, L. Feng, A. Nilsson, and M. Aversano. “Predicted and measured plate velocities induced by turbulent boundary layers”. In: *Journal of Sound Vibration* 331 (Nov. 2012). ADS Bibcode: 2012JSV...331.5309L, pp. 5309–5325.

[22] R. Deshmukh, A. Culler, B. Miller, and J. McNamara. “Response of Skin Panels to Combined Self and Boundary Layer Induced Fluctuating Pressure”. In: *Journal of Fluids and Structures* 58 (Oct. 2015), p. 216.

[23] A. Frendi. “Coupling Between a Supersonic Turbulent Boundary Layer and a Flexible Structure”. In: *AIAA Journal* 35.1 (Jan. 1997). Publisher: American Institute of Aeronautics and Astronautics, pp. 58–66.

[24] A. Gogulapati, R. Deshmukh, A. Crowell, J. McNamara, V. Vyas, X. Wang, M. Mignolet, T. Beberniss, S. Spottswood, and T. Eason. “Response of a panel to shock impingement: Modeling and comparison with experiments”. In: *55th AIAA/ASMe/ASCE/AHS/SC Structures, Structural Dynamics, and Materials Conference-SciTech Forum and Exposition 2014*. 2014, p. 0148.

[25] A. Gogulapati, R. Deshmukh, J. J. McNamara, V. Vyas, X. Wang, M. P. Mignolet, T. Beberniss, S. M. Spottswood, and T. Eason. “Response of a panel to shock impingement: Modeling and comparison with experiments-part 2”. In: *56th AIAA/ASCE/AHS/ASC Structures, Structural Dynamics, and Materials Conference*. 2015, p. 0685.

[26] P. V. Hahn and A. Frendi. “Interaction of Three-Dimensional Protuberances with a Supersonic Turbulent Boundary Layer”. In: *AIAA Journal* 51.7 (2013). Publisher: American Institute of Aeronautics and Astronautics _eprint: https://doi.org/10.2514/1.J052101, pp. 1657–1666.

[27] J. Gan, H. Im, X.-Y. Chen, G. Zha, and C. L. Pasiliao. “Prediction of Wing Flutter Boundary Using High Fidelity Delayed Detached Eddy Simulation”. In: *56th AIAA/ASCE/AHS/ASC Structures, Structural Dynamics, and Materials Conference*. AIAA SciTech Forum. American Institute of Aeronautics and Astronautics, Jan. 2015.

[28] M. Visbal. “Viscous and inviscid interactions of an oblique shock with a flexible panel”. In: *Journal of Fluids and Structures* 48 (2014), pp. 27–45.

[29] C. M. Ostoich, D. J. Bodony, and P. H. Geubelle. “Interaction of a Mach 2.25 turbulent boundary layer with a fluttering panel using direct numerical simulation”. In: *Physics of Fluids* 25.11 (Nov. 2013). Publisher: American Institute of Physics, p. 110806.

[30] S. M. Spottswood, T. Eason, and T. Beberniss. “Full-field, dynamic pressure and displacement measurements of a panel excited by shock boundary-layer interaction”. In: *19th AIAA/CEAS aeroacoustics conference*. 2013, p. 2016.

[31] S. Willems, A. Gülhan, and B. Esser. “Shock induced fluid-structure interaction on a flexible wall in supersonic turbulent flow”. In: *Progress in Flight Physics* 5 (2013), pp. 285–308.

[32] D. Daub, S. Willems, and A. Gülhan. “Experiments on the interaction of a fast-moving shock with an elastic panel”. In: *AIAA Journal* 54.2 (2015), pp. 670–678.

[33] E. R. Jinks, P. J. Bruce, and M. J. Santer. “The Use of Actuated Flexible Plates for Adaptive Shock Control Bumps”. en. In: *53rd AIAA Aerospace Sciences Meeting*. Kissimmee, Florida: American Institute of Aeronautics and Astronautics, Jan. 2015.

[34] G. M. D. Currao, A. J. Neely, C. M. Kennell, S. L. Gai, and D. R. Buttsworth. “Hypersonic Fluid–Structure Interaction on a Cantilevered Plate with Shock Impingement”. en. In: *AIAA Journal* 57.11 (Nov. 2019), pp. 4819–4834.

[35] S. V. Varigonda and V. Narayanaswamy. “Investigation of Shock Wave Oscillations over a Flexible Panel in Supersonic Flows”. en. In: *AIAA Aviation 2019 Forum*. Dallas, Texas: American Institute of Aeronautics and Astronautics, June 2019.

[36] T. J. Whalen, A. G. Schöneich, S. J. Laurence, B. T. Sullivan, D. J. Bodony, M. Freydin, E. H. Dowell, and G. M. Buck. “Hypersonic Fluid–Structure Interactions in Compression Corner Shock-Wave/Boundary-Layer Interaction”. en. In: *AIAA Journal* 58.9 (Sept. 2020), pp. 4090–4105.

[37] A. L. Laganelli and J. R. Howe. *Prediction of Pressure Fluctuations Associated with Maneuvering Re-entry Weapons. Volume I*. en. Tech. rep. Section: Technical Reports. GENERAL ELECTRIC CO PHILADELPHIA PA RE-ENTRY SYSTEMS DEPT, July 1977.

[38] M. Visbal. “On the interaction of an oblique shock with a flexible panel”. In: *Journal of Fluids and structures* 30 (2012), pp. 219–225.

[39] E. Jinks, P. Bruce, and M. Santer. “Optimisation of adaptive shock control bumps with structural constraints”. In: *Aerospace Science and Technology* 77 (2018), pp. 332–343.

[40] B. E. Schmidt. “On the Stability of Supersonic Boundary Layers with Injection”. PhD thesis. California Institute of Technology, 2015.

[41] C. A. Mouton. “Transition between Regular Reflection and Mach Reflection in the Dual-Soluton Domain”. PhD thesis. California Institute of Technology, 2007.

[42] R. Blevins. *Formulas for Natural Frequency and Mode Shape*. Krieger Publishing Company, 2001.

[43] W. P. Flaherty. “Effects of Local and Global Mechanical Distortions to Hypervelocity Boundary Layers”. PhD thesis. University of Illinois at Urbana Champaign, 2013.

[44] N. J. Parziale, B. E. Schmidt, J. S. Damazo, P. S. Wang, H. G. Hornung, and J. E. Shepherd. “Pulsed Laser Diode for use as a Light Source for Short-Exposure, High-Frame-Rate Flow Visualization”. In: *53rd AIAA Aerospace Sciences Meeting* (2015).

[45] A. L. R. T. Simon M. Walker and G. K. Taylor. “Photogrammetric reconstruction of high-resolution surface topographies and deformable wing kinematics of tethered locusts and free-flying hoverflies”. In: *J. R. Soc. Interface* 6 (2009), pp. 351–366.

[46] K. B. Atkinson. *Close range photogrammetry and machine vision*. Reinhold, 1996.

[47] R. I. Hartley and A. Zisserman. *Multiple view geometry in computer vision, 2nd edn.* Cambridge University Press, 2004.

[48] L. Yu and B. Pan. “Single-camera stereo-digital image correlation with a four-mirror adapter: Optimized design and validation”. In: *Opt. Laser. Eng.* 87 (2016), pp. 120–128.

[49] J. J. Quirk. “Amrita–a computational facility (for CFD modeling)”. In: *VKI 29th CFD Lecture Series* (1998).

[50] D. J. Garmann. “Characterization of the vortex formation and evolution about a revolving wing using high-fidelity simulation”. PhD thesis. University of Cincinnati, 2013.

[51] R. M. Beam and R. Warming. “An implicit factored scheme for the compressible Navier-Stokes equations”. In: *AIAA journal* 16.4 (1978), pp. 393–402.

[52] M. Visbal and R. Gordnier. “Numerical simulation of the interaction of a transitional boundary layer with a 2-D flexible panel in the subsonic regime”. In: *Journal of fluids and structures* 19.7 (2004), pp. 881–903.

[53] M. R. Visbal and D. V. Gaitonde. “High-order-accurate methods for complex unsteady subsonic flows”. In: *AIAA journal* 37.10 (1999), pp. 1231–1239.

[54] D. V. Gaitonde and M. R. Visbal. “Padé-type higher-order boundary filters for the Navier-Stokes equations”. In: *AIAA journal* 38.11 (2000), pp. 2103–2112.

[55] M. R. Visbal and D. V. Gaitonde. “On the use of higher-order finite-difference schemes on curvilinear and deforming meshes”. In: *Journal of Computational Physics* 181.1 (2002), pp. 155–185.

[56] M. Visbal and D. Gaitonde. “Shock capturing using compact-differencing-based methods”. In: *43rd AIAA Aerospace Sciences Meeting and Exhibit*. 2005, p. 1265.

[57] N. M. Newmark. “A method of computation for structural dynamics”. In: *Journal of the engineering mechanics division* 85.3 (1959), pp. 67–94.

[58] V. Shinde, J. J. McNamara, and D. V. Gaitonde. “Shock Wave Turbulent Boundary Layer Interaction Over a Flexible Panel”. In: *AIAA Scitech 2021 Forum*. 2021, p. 3434679.

[59] R. E. Gordnier and M. R. Visbal. “Development of a three-dimensional viscous aeroelastic solver for nonlinear panel flutter”. In: *Journal of fluids and structures* 16.4 (2002), pp. 497–527.

[60] V. Shinde, A. Becks, R. Deshmukh, J. McNamara, D. Gaitonde, M. Neet, and J. Austin. “Spatially developing supersonic turbulent boundary layer subjected to static surface deformations”. en. In: *European Journal of Mechanics - B/Fluids* 89 (Sept. 2021), pp. 485–500.

[61] M. C. Neet and J. M. Austin. “Effects of Surface Compliance on Shock Boundary Layer Interaction in the Caltech Mach 4 Ludwieg Tube”. In: *AIAA Scitech 2020 Forum*. 2020, p. 0816.

[62] A. J. Smits and J.-P. Dussauge. *Turbulent shear layers in supersonic flow*. Springer Science & Business Media, 2006.

[63] M. D. Van Dyke. “A study of second-order supersonic-flow theory”. In: *National Advisory Committee for Aeronautics* Technical Notes.2200 (1951), pp. 1–73.

[64] K. A. Chauhan, P. A. Monkewitz, and H. M. Nagib. “Criteria for assessing experiments in zero pressure gradient boundary layers”. In: *Fluid Dynamics Research* 41.2 (2009), p. 021404.

[65] R. Vinuesa, R. Örlü, C. S. Vila, A. Ianiro, S. Discetti, and P. Schlatter. “Revisiting history effects in adverse-pressure-gradient turbulent boundary layers”. In: *Flow, turbulence and combustion* 99.3-4 (2017), pp. 565–587.

[66] M.-b. Sun, Z. Hu, and N. D. Sandham. “Recovery of a supersonic turbulent boundary layer after an expansion corner”. In: *Physics of Fluids* 29.7 (2017), p. 076103.

[67] M. Sun, N. D. Sandham, and Z. Hu. “Turbulence structures and statistics of a supersonic turbulent boundary layer subjected to concave surface curvature”. In: *Journal of Fluid Mechanics* 865 (2019), pp. 60–99.

[68] P. Schlatter and R. Örlü. “Turbulent boundary layers at moderate Reynolds numbers: inflow length and tripping effects”. In: *Journal of Fluid Mechanics* 710 (2012), p. 5.

[69] D. R. Smith and A. J. Smits. “The effects of successive distortions on a turbulent boundary layer in a supersonic flow”. In: *Journal of Fluid Mechanics* 351 (1997), pp. 253–288.

[70] D. Smith and A. Smits. “A study of the effects of curvature and compression on the behavior of a supersonic turbulent boundary layer”. In: *Experiments in fluids* 18.5 (1995), pp. 363–369.

[71] P. Bradshaw. “The effect of mean compression or dilatation on the turbulence structure of supersonic boundary layers”. In: *Journal of Fluid Mechanics* 63.3 (1974), pp. 449–464.

[72] A. Townsend. “The Structure of Turbulent Shear Flow”. In: *The Structure of Turbulent Shear Flow, by AAR Townsend, pp. 440. ISBN 0521298199. Cambridge, UK: Cambridge University Press, March 1980.* (1980), p. 440.

[73] M. Jayaram, J. Donovan, J.-P. Dussauge, and A. Smits. “Analysis of a rapidly distorted, supersonic, turbulent boundary layer”. In: *Physics of Fluids A: Fluid Dynamics* 1.11 (1989), pp. 1855–1864.

[74] H. S. Ribner and M. Tucker. *Spectrum of turbulence in a contracting stream*. Vol. 1113. National Advisory Committee for Aeronautics, 1952.

[75] G. Batchelor and I. Proudman. “The effect of rapid distortion of a fluid in turbulent motion”. In: *The Quarterly Journal of Mechanics and Applied Mathematics* 7.1 (1954), pp. 83–103.

[76] M. V. Morkovin. “Effects of compressibility on turbulent flows”. In: *Mécanique de la Turbulence* 367 (1962), p. 380.

[77] S. Pirozzoli and M. Bernardini. “Turbulence in supersonic boundary layers at moderate Reynolds number”. In: *Journal of Fluid Mechanics* 688 (2011), pp. 120–168.

[78] B. Ganapathisubramani, N. T. Clemens, and D. Dolling. “Large-scale motions in a supersonic turbulent boundary layer”. In: *Journal of fluid Mechanics* 556 (2006), pp. 271–282.

[79] M. P. Martın. “Direct numerical simulation of hypersonic turbulent boundary layers. Part 1. Initialization and comparison with experiments”. In: *Journal of Fluid Mechanics* 570 (2007), pp. 347–364.

[80] Y. Na and P. Moin. “Direct numerical simulation of a separated turbulent boundary layer”. In: *Journal of Fluid Mechanics* 374 (1998), pp. 379–405.

[81] J. A. Sillero, J. Jiménez, and R. D. Moser. “Two-point statistics for turbulent boundary layers and channels at Reynolds numbers up to $\delta^+ \approx 2000$”. In: *Physics of Fluids* 26.10 (2014), p. 105109.

[82] V. J. Shinde, J.-P. Laval, and M. Stanislas. “Effect of mean pressure gradient on the turbulent wall pressure–velocity correlations”. In: *Journal of Turbulence* 15.12 (2014), pp. 833–856.

[83] J. L. Lumley. “Computational modeling of turbulent flows”. In: *Advances in applied mechanics*. Vol. 18. Elsevier, 1979, pp. 123–176.

[84] S. Pope and S. B. Pope. *Turbulent Flows*. Cambridge University Press, 2000.

[85] P. Bradshaw. “‘Inactive’motion and pressure fluctuations in turbulent boundary layers”. In: *Journal of Fluid Mechanics* 30.2 (1967), pp. 241–258.

[86] S. J. Beresh, J. F. Henfling, R. W. Spillers, and B. O. Pruett. “Fluctuating wall pressures measured beneath a supersonic turbulent boundary layer”. In: *Physics of Fluids* 23.7 (2011), p. 075110.

[87] J. M. Delery. “Shock wave/turbulent boundary layer interaction and its control”. In: *Progress in Aerospace Sciences* 22.4 (1985), pp. 209–280.

[88] V. Shinde, J. McNamara, and D. Gaitonde. “Control of transitional shock wave boundary layer interaction using structurally constrained surface morphing”. In: *Aerospace Science and Technology* (2019), p. 105545.

[89] N. T. Clemens and V. Narayanaswamy. “Low-frequency unsteadiness of shock wave/turbulent boundary layer interactions”. In: *Annual Review of Fluid Mechanics* 46 (2014), pp. 469–492.

[90] E. Touber and N. D. Sandham. *Low-order stochastic modelling of low-frequency motions in reflected shock-wave/boundary-layer interactions*. Vol. 671. 2011, pp. 417–465.

[91] K. R. Brouwer, A. Gogulapati, and J. J. McNamara. “Interplay of Surface Deformation and Shock-Induced Separation in Shock/Boundary-Layer Interactions”. In: *AIAA Journal* (2017). Publisher: American Institute of Aeronautics and Astronautics, pp. 1–16.

[92] R. J. Gordon. “Boundary Layer Theory.” In: *AIChEMI Modul. Instr. Ser. C Transp.* 3 (1983), pp. 23–27.

[93] H. Ashley and G. Zartarian. “Piston Theory-A New Aerodynamic Tool for the Aeroelastician”. In: *Journal of the Aeronautical Sciences* 23.12 (Dec. 1956). Publisher: American Institute of Aeronautics and Astronautics, pp. 1109–1118.

[94] D. H. Hodges. “Proper definition of curvature in nonlinear beam kinematics”. In: *AIAA journal* 22.12 (1984), pp. 1825–1827.

[95] V. J. Shinde and D. V. Gaitonde. “Lagrangian approach for modal analysis of fluid flows”. In: *Journal of Fluid Mechanics* 928 (2021), A35.

[96] H. T. Pham, Z. Gianikos, and V. Narayanaswamy. “Compression Ramp Induced Shock Wave/Turbulent Boundary Layer Interactions on a Compliant Material”. In: *2018 AIAA/ASCE/AHS/ASC Structures, Structural Dynamics, and Materials Conference*. 2018, p. 0095.

[97] V. Shinde, J. McNamara, D. Gaitonde, C. Barnes, and M. Visbal. “Transitional shock wave boundary layer interaction over a flexible panel”. In: *Journal of Fluids and Structures* 90 (2019), pp. 263–285.

[98] N. R. Boyer, J. McNamara, D. Gaitonde, C. J. Barnes, and M. R. Visbal. “Features of panel flutter response to shock boundary layer interactions”. In: *Journal of Fluids and Structures* 101 (2021), p. 103207.

[99] S. V. Varigonda, C. Jenquin, and V. Narayanaswamy. “Impact of Panel Vibrations on the Dynamic Field Properties in Supersonic flow”. In: *AIAA AVIATION 2021 FORUM*. 2021, p. 2926.

[100] E. H. Dowell. “Panel flutter-A review of the aeroelastic stability of plates and shells”. In: *AIAA Journal* 8.3 (1970), pp. 385–399.

[101] P. J. Schmid. “Dynamic mode decomposition of numerical and experimental data”. In: *Journal of fluid mechanics* 656 (2010), pp. 5–28.

[102] C. W. Rowley, I. MEZI?, S. Bagheri, P. Schlatter, D. HENNINGSON, et al. “Spectral analysis of nonlinear flows”. In: *Journal of fluid mechanics* 641.1 (2009), pp. 115–127.

[103] V. Pasquariello, S. Hickel, and N. A. Adams. “Unsteady effects of strong shock-wave/boundary-layer interaction at high Reynolds number”. In: *Journal of Fluid Mechanics* 823 (2017), pp. 617–657.

[104] J. W. Nichols, J. Larsson, M. Bernardini, and S. Pirozzoli. “Stability and modal analysis of shock/boundary layer interactions”. In: *Theoretical and Computational Fluid Dynamics* 31.1 (2017), pp. 33–50.

[105] S. P. Schneider. “Effects of Roughness on Hypersonic Boundary-Layer Transition”. In: *Journal of Spacecraft and Rockets* (2008).

[106] O. J. H. Williams and A. J. Smits. “Effect of Tripping on Hypersonic Turbulent Boundary-Layer Statistics”. In: *AIAA Journal* (2017).

[107] A. Towne, O. Schmidt, and T. Colonius. “Spectral proper orthogonal decomposition and its relationship to dynamic mode decomposition and resolvant analysis”. In: *Journal of Fluid Mechanics* 847 (2018), pp. 821–867.